

University of Alberta

**Microstructure – Property Correlation in Magnesium-based Hydrogen
Storage Systems**

The Case for Ball-milled Magnesium Hydride Powder and Mg-based Multilayered Composites

by

Mohsen Danaie

A thesis submitted to the Faculty of Graduate Studies and Research
in partial fulfillment of the requirements for the degree of

Doctor of Philosophy

in

Materials Engineering

Chemical and Materials Engineering Department

©Mohsen Danaie

Spring 2011

Edmonton, Alberta

Permission is hereby granted to the University of Alberta Libraries to reproduce single copies of this thesis and to lend or sell such copies for private, scholarly or scientific research purposes only. Where the thesis is converted to, or otherwise made available in digital form, the University of Alberta will advise potential users of the thesis of these terms.

The author reserves all other publication and other rights in association with the copyright in the thesis and, except as herein before provided, neither the thesis nor any substantial portion thereof may be printed or otherwise reproduced in any material form whatsoever without the author's prior written permission.

Dedication

This thesis is dedicated to my family,
Mom, Dad, Gita, Mehran,
and the memory of my late brother, Keivan.

Abstract

The main focus of this thesis is the characterization of defects and microstructure in high-energy ball milled magnesium hydride powder and magnesium-based multilayered composites. Enhancement in kinetics of hydrogen cycling in magnesium can be achieved by applying severe plastic deformation. A literature survey reveals that, due to extreme instability of α -MgH₂ in transmission electron microscope (TEM), the physical parameters that researchers have studied are limited to particle size and grain size. By utilizing a cryogenic TEM sample holder, we extended the stability time of the hydride phase during TEM characterization. Milling for only 30 minutes resulted in a significant enhancement in desorption kinetics. A subsequent annealing cycle under pressurized hydrogen reverted the kinetics to its initial sluggish state. Cryo-TEM analysis of the milled hydride revealed that mechanical milling induces deformation twinning in the hydride microstructure. Milling did not alter the thermodynamics of desorption. Twins can enhance the kinetics by acting as preferential locations for the heterogeneous nucleation of metallic magnesium. We also looked at the phase transformation characteristics of desorption in MgH₂. By using energy-filtered TEM, we investigated the morphology of the phases in a partially desorbed state. Our observations prove that desorption phase transformation in MgH₂ is of “nucleation and growth” type, with a substantial energy barrier for nucleation. This is contrary to the generally assumed “core-shell” structure in most of the simulation models for this system. We also tested the hydrogen storage cycling behavior of bulk centimeter-scale Mg-Ti and Mg-SS multilayer composites synthesized by accumulative roll-bonding. Addition of either phase (Ti or SS)

allows the reversible hydrogen sorption at 350°C, whereas identically roll-bonded pure magnesium cannot be absorbed. In the composites the first cycle of absorption (also called “activation”) kinetics improve with increased number of fold and roll (FR) operations. With increasing FR operations the distribution of the Ti phase is progressively refined, and the shape of the absorption curve no longer remains sigmoidal. Up to a point, increasing the loading amount of the second phase also accelerates the kinetics. Microscopy analysis performed on 1-2 wt.% hydrogen absorbed composites demonstrates that MgH₂ formed exclusively on various heterogeneous nucleation sites. During activation, MgH₂ nucleation occurred at the Mg-hard phase interfaces. On the subsequent absorption cycles, heterogeneous nucleation primarily occurred in the vicinity of “internal” free surfaces such as cracks.

Acknowledgements

First and foremost, I would like to thank my PhD supervisor, Dr. David Mitlin, for his strong support and encouragement during the course of my research. Through many - oftentimes heated- discussions, he taught me to maintain an open outlook towards research and to be the pickiest critic towards myself. I am also deeply indebted to all my colleagues in Dr. Mitlin's group, especially Dr. Colin Ophus, Babak Shalchi Amirkhiz, Dr. Peter Kalisvaart, Brian Olsen, Christopher Harrower, Chris Holt and Erik Lubber.

Without the constant support from the great technicians, both at the university departments and within the National Institute for Nanotechnology (NINT-NRC), this work would not have reached its current stage. Greg Popowich (Physics Department), Julie Qian (NINT), and Daniel Salamon (NINT) taught me how to operate the microscopes. Jim Skwarok (CME) helped us in particle size analysis (Chapter 2). Steve Launspach (NINT) taught me the operation of the X-ray diffractometer. My sincere thanks go to all of them.

During these years at University of Alberta I have had the opportunity to collaborate with great colleagues. Dr. Marek Malac (Physics Department- NINT) taught me the basics of electron energy loss spectroscopy. Insightful discussions with Professor Ray Egerton (Physics Department) contributed to our energy-filtered TEM approach (Chapter 3) for characterizing the hydride powder samples. I performed most of the experiments for Chapter 4 of this thesis in Professor Jacques Huot's lab at *Institut de Recherche sur l'Hydrogène* (IRH), Trois-Rivières, Québec. I am grateful to him for facilitating this visit and his support.

Last but not least, my heartfelt thanks go to my family for their unconditional love and support through all my graduate studies. This thesis is dedicated to them.

Contents

CHAPTER 1- Introduction	1
1-1- HYDROGEN AS AN ENERGY VECTOR	1
1-2- HYDROGEN STORAGE	3
1-3- HYDROGEN IN METALS	5
1-3-1- THERMODYNAMICS OF HYDRIDE FORMATION	6
1-3-2- KINETICS OF HYDRIDE FORMATION	9
1-4- MAGNESIUM AS A HYDROGEN STORAGE MEDIUM	10
1-5- THE MOTIVATION AND SCOPE OF THIS THESIS	12
1-6- REFERENCES	15
CHAPTER 2- TEM Analysis of Milled MgH₂	17
2-1- INTRODUCTION	17
2-2 EXPERIMENTAL PROCEDURES	19
2-3- RESULTS	22
2-4- DISCUSSION	33
2-5- SUMMARY AND CONCLUSIONS	36
2-6- REFERENCE	38
CHAPTER 3- Analysis of Twins & Partially Dehydrogenated MgH₂	41
3-1- INTRODUCTION	41
3-2- EXPERIMENTAL PROCEDURES	44
3-3- RESULTS	46
3-3-1- DEFORMATION TWINS: EXPERIMENTAL	46
3-3-2- THERMODYNAMIC STABILITY OF DEFORMATION TWINS: DFT	51
3-3-3- PARTIALLY DESORBED MICROSTRUCTURE: EXPERIMENTAL	53
3-4-DISCUSSION	57
3-4-1- EFFECT OF TWINS ON THE THERMODYNAMICS AND KINETICS OF DESORPTION	57
3-4-2- PARTIALLY DESORBED MICROSTRUCTURE	58
3-5- SUMMARY AND CONCLUSIONS	60
3-6- REFERENCE	62
CHAPTER 4- Mg-Ti & Mg-SS Composites	66
4-1- INTRODUCTION	66
4-2- EXPERIMENTAL PROCEDURES	68
4-3- RESULTS	70
4-3-1- Mg-Ti 15FR, EFFECT OF TI CONTENT	70
4-3-2- Mg-22 AT.%Ti, EFFECT OF NUMBER OF FR	76
4-3-3- Mg-STAINLESS STEEL COMPOSITES	83
4-4- DISCUSSION	84
4-5- SUMMARY AND CONCLUSION	91
4-6- REFERENCES	93
CHAPTER 5- Conclusions	97
APPENDIX 1	100

List of Tables

	Page
Table 1-1- Values of n in the JMAK equation as correlated to the modes of nucleation and growth	10
Table 1-2- Crystallographic data for Mg and MgH ₂ polymorphs	11
Table 2-1- Crystallographic data used for generating electron diffraction simulations.	22
Table 2-2- Mean grain size and lattice strain obtained from the IBA analysis of the α -MgH ₂ XRD peaks.	24
Table 3-1- The crystal data for Rutile MgH ₂ and deformation twin MgH ₂ . The calculated lattice constants and interatomic distances. Unit is Å.	53
Table 4-1- Labeling and respective volume fractions of the 15 FR titanium and stainless steel samples.	69
Table 4-2- Theoretical versus experimental (recorded on the second sorption cycle) hydrogen capacities of different Mg-Ti composites. The maximum (theoretical) capacity here only takes into account magnesium.	75
Table A-1- Equilibrium hydrogen pressures as function of temperature for α -MgH ₂ .	103

List of Figures

	Page
Figure 1-1- World primary energy production (1970-2007) categorized by source.	2
Figure 1-2- Hydrogen as an energy vector, connecting various production techniques to the final utilization. Shaded boxes for production also entail significant carbon dioxide emission.	3
Figure 1-3- (A) Schematic pressure-composition isotherm diagram, with a marking the solid solution of hydrogen in metal and b the hydride. (B) van't Hoff plot for calculating the enthalpy of hydride formation ΔH .	7
Figure 1-4- Magnesium-hydrogen phase diagram at 1 bar hydrogen pressure	11
Figure 1-5- (A) a typical planetary ball mill machine, (B) schematic of the movement pattern within the vial of an operating planetary milling machine	13
Figure 1-6-(A) Schematic of the accumulative roll bonding processing, (B) Schematic of the procedure we used for preparing Mg-Ti multilayered composites	14
Figure 2-1- (A) DSC and (B) TGA results for the desorption of the as-received hydride, 30 minute milled hydride (m30min), and milled and annealed hydride (m30min-a2hrs and m30min-a16hrs).	23
Figure 2-2- SEM micrographs of magnesium hydride powder (A) As-received, (B) Milled for 30 minutes, (C) Milled for 30 minutes and annealed for 2 hours, and (D) Milled for 30 minutes and annealed for 16 hours.	25
Figure 2-3- Particle size distributions of the as-received, milled and milled and 16hrs annealed MgH_2 powders.	26
Figure 2-4- TEM micrographs of the milled MgH_2 powder: (A) Bright field image of a cluster of powder particles, (B) corresponding diffraction ring pattern with α - MgH_2 simulation.	27

- Figure 2-5- TEM micrographs of the milled MgH_2 powder: (A) Bright field image, (B) dark field micrograph, obtained using $g = 020_a$, of the same area highlighting a typical $\alpha\text{-MgH}_2$ grain within an individual particle (C) corresponding indexed $\alpha\text{-MgH}_2$ SAD. 27
- Figure 2-6- TEM micrographs of two overlapping milled $\alpha\text{-MgH}_2$ powder particles: (A) Bright field micrograph; (B) Dark field micrograph highlighting the presence of multiple twins, obtained using the streaked twin reflection (arrowed in (C)). 27
- Figure 2-7- TEM micrographs of the milled $\alpha\text{-MgH}_2$ powder demonstrating the presence of nano-scale twins within individual grains: (A) Bright field image; (B) Dark field micrograph of the same area; (C) corresponding SAD of $\alpha\text{-MgH}_2$. Arrows point to the same location in both images and to the portion of the 110_a ring pattern used for dark field imaging. 29
- Figure 2-8- TEM micrographs of the milled and 2 hour annealed MgH_2 powder: (A) Bright field micrograph; (B) Dark field micrograph demonstrating the presence of powder particles that are essentially a single crystal. The dark-field image was obtained using the arrowed portion of the $011 \alpha\text{-MgH}_2$ reflections (C). 29
- Figure 2-9- TEM micrographs of the milled and 2 hour annealed MgH_2 powder: (A) Bright field micrograph; (B) Dark field micrograph, obtained using a portion of the $011 \alpha\text{-MgH}_2$ ring pattern, highlighting the presence of twins (arrowed); (C) corresponding SAD. 29
- Figure 2-10- TEM micrographs of the the same area observed in figure 2-9 after a long exposure to electron beam: (A) Bright field micrograph; (B) Dark field micrograph, obtained using a portion of the $01\text{-}11 \text{ Mg}$ ring pattern, showing the fine grain structure of Mg; (C) corresponding SAD. The simulation corresponds to Mg ring pattern. Some rings of MgO can also be observed. 30
- Figure 2-11- TEM micrographs of the milled and 16 hour annealed MgH_2 powder: (A) Bright field micrograph; (B) dark field micrograph, obtained using $g = 110_a$ reflection; (C) dark field micrograph obtained using a portion of the 002 MgO ring pattern (first continuous ring), and; (D) corresponding SAD. 31

Figure 2-12- TEM micrographs of the milled and 16 hour annealed MgH₂ powder: (A) Bright field micrograph; (B) dark field micrograph, imaged using a portion of the 110 α -MgH₂ ring pattern, showing several nano-scale α -MgH₂ grains; (C) Corresponding SAD. 32

Figure 2-13- TEM micrographs of the milled and 16 hour annealed MgH₂ powder: (A) Bright field micrograph; (B) Dark field micrograph, imaged using $g = -110$, reflection, showing a large individual α grain with a coarse twin segment which appears dark (arrowed); (C) Corresponding SAD. 32

Figure 2-14- Histograms of the individual grain areas for the milled and the milled and 2 hour annealed powders, obtained from dark field micrographs. 32

Figure 3-1- Kinetic analysis for the desorption of the three powder samples. Calculated values for activation energy (E) appear on the right. Activation energy for *as-received* powder is also presented for comparison. 47

Figure 3-2- Van't Hoff plots generated using high pressure DSC, yielding the following enthalpy of reaction values: *As-received* desorption, $\Delta H = 78$ kJ/mole; *As-received* absorption, $\Delta H = -70$ kJ/mole; *Milled* desorption $\Delta H = 75$ kJ/mole; *Milled* absorption $\Delta H = -70$ kJ/mole (negative means exothermic). 47

Figure 3-3- TEM analysis of a *Milled* powder particle: (A) Bright field micrograph; (B) Selected area diffraction SAD; (C) Simulation of the diffraction pattern which shows that the matrix ZA is close to $[-21-2]$, and the observed twinning plane is (101). (D) schematic of the twin geometry looking down $[010]$ (ion sizes not to scale); The numbers show the depth of the ions with reference to (010) plane; TEM analysis of a *Milled* powder particle: (E) dark field micrograph obtained using the matrix spot $g = -202$ α -MgH₂; (F) dark field micrograph obtained using $g = 020$ α -MgH₂ twin reflection. 49

Figure 3-4- TEM micrographs of *Milled-Annealed* powder sample: (A) bright field micrograph, (B) dark field micrograph obtained using $g = 110$ α -MgH₂ reflection; (C) corresponding SAD pattern. 51

- Figure 3-5- TEM micrographs of several *Milled-Annealed-Milled* powder particles: (A) bright field micrograph, (B) dark field micrograph obtained using a portion of the 110 α -MgH₂ ring pattern (C) diffraction pattern and simulation of α -MgH₂. Arrow points to the same area in the bright field and the dark field micrographs where two twinned grains show strong diffraction contrast. 51
- Figure 3-6- Multiple deformation twins. In order to highlight the twin structures (the black lines), supercells are shown. (A) Four metal atoms cell with 100% deformation twins (2x2x2 supercell); (B) Eight metal atoms cell with 50% deformation twins (2x2x1 supercell); (C) Twelve metal atoms with 33% deformation twins (2x2x1 supercell). 52
- Figure 3-7- (A) The optimized structure of twinned α -MgH₂. (B) A side view of the twin interface. 53
- Figure 3-8- (A) Time-resolved series of low-energy loss spectra from in-situ desorption of Milled sample; (B) An example of room-temperature in-situ desorption as observed by EFTEM. Initial state bright field micrograph is shown in top-center. Left column shows Mg at $t \approx 0$ seconds beam exposure and after 421 seconds. Right column shows MgH₂ after 15 and 413 second exposures. 55
- Figure 3-9- Partially desorbed relatively large hydride particle in the *Milled* condition. (A) bright field micrograph; (B) Mg - 10eV and (C) MgH₂ - 14eV energy-filtered micrographs. 55
- Figure 3-10- Another example of a partially desorbed relatively large hydride particle in the *Milled* condition. (A) bright field micrograph; (B) Mg - 10eV and (C) MgH₂ - 14eV energy-filtered micrographs. 56
- Figure 3-11- Several smaller metal and hydride particles taken from a partially desorbed *Milled* condition sample. (A) bright field micrograph; (B) Mg - 10eV and (C) MgH₂ - 14eV energy-filtered micrographs. 56
- Figure 3-12- Another example of smaller metal and hydride particles taken from a partially desorbed *Milled* condition sample. (A) bright field micrograph; (B) Mg - 10eV and (C) MgH₂ - 14eV energy-filtered micrographs. 56

Figure 4-1- SEM micrographs showing the as-rolled microstructure of the Mg-Ti samples with different compositions, all folded and rolled for 15 times. The arrow shows the approximate trace of the rolling plane. The images are at the same magnification. 72

Figure 4-2- Mg-Ti composites with 15FR repetitions but with different Ti content. (A) XRD obtained (via multiple whole profile fitting) average grain size of Mg as a function of Ti content. (B) Bright field TEM micrograph of a representative region in the Mg portion of a Mg-10at.%Ti composite. (C) XRD obtained dislocation density in Mg, and (D) dislocation density in Ti. 73

Figure 4-3- Hydrogen sorption kinetics of 15FR Mg-Ti composites with varying Ti content, tested at 350°C: (A) First absorption (activation), (B) First desorption, (C) and (D) Second absorption and desorption, respectively. 74

Figure 4-4- (A): Pressure – composition curve of the 15FR Mg-22at.%Ti composite at 350°C. (B) XRD patterns of the composite in the as-rolled state and after the PCT experiment (desorbed). (C) XRD patterns of as-rolled compared to the absorbed state of Mg-22 at.%Ti sample (50FR). 75

Figure 4-5- SEM micrographs showing the as-rolled microstructure of the Mg-22 at.%Ti composites. The arrows show the approximate trace of the rolling plane. White arrows in (C) mark necking events. The images are at the same magnification, except for D). 77

Figure 4-6- Results of the multiple whole profile (MWP) fitting analysis on the XRD data for Mg-22 at.%Ti composites with different number of FR operations. (A) Mg volume weighted average grain size. (B) Dislocation density in Mg. (C) dislocation density in Ti. 78

Figure 4-7- (A) Comparison of the first absorption cycle for the 22at.%Ti composites, but with varying FR number, tested at 350°C. (B) Hydrogen sorption cycling kinetics of the Mg-22at.%Ti 50FR composite. 79

Figure 4-8- First absorption cycle for Mg-22 at.% Ti 15FR composite (A) Interrupted and full absorption curves, (B) XRD patterns. (C) SEM micrograph of the cross-sectioned composite absorbed with 1.6wt.%H. Arrows point to MgH₂ (darker regions) nucleated in the proximity of TiH₂. 80

- Figure 4-9- First absorption cycle for Mg-22 at.% Ti 90FR composite (A) Interrupted and full absorption curves (B) XRD patterns. (C) SEM micrograph of the cross-sectioned composite absorbed with 1.6wt.% H. Arrows point to MgH₂ (darker regions) nucleated in the proximity of TiH₂. 82
- Figure 4-10- SEM micrographs from the Mg- 22 at.% Ti 15 FR composite, quenched at 2.5 wt.% H on the third absorption cycle. 83
- Figure 4-11- Hydrogen sorption kinetics of 15 FR Mg-SS composites, tested at 350°C: (A) Activation, (B) 1st desorption, (C) 2nd absorption, and (D) 2nd desorption. The test for Mg-1vol.% SS was discontinued after the first cycle due to sluggish kinetics. 84
- Figure 4-12- Microstructure of Mg-SS composites interrupted on their first absorption cycle at ~1 wt.% H, showing the nucleation sites of MgH₂ (arrowed). (A) Hydride nucleation in Mg-5 vol% SS samples near the stainless steel particles and at cracks. (B) Hydride nucleation in Mg-5 vol% SS samples near smaller cracks and other heterogeneous nucleation sites. (C) Hydride nucleation in Mg-18vol%SS composite. 85
- Figure 4-13- (A) and (B) First derivatives with respect to time of activation steps of Mg-Ti composites with different compositions (raw data presented in Fig. 3A), and Mg-22 at.% Ti with various FR number (raw data plot presented in Fig. 7A), respectively. (C) a schematic demonstration of two concurrent reactions with different rate constants. (D) time derivative of the model data presented in (C). 86
- Figure 4-14- Schematic of the potential nucleation sites in Mg-composite system: (1) the incoherent interface between the hard phase and the magnesium (2) cracks, (3) kissing bonds and (4) external surfaces. Hydrogenation on location (4) was only occasionally observed. 87
- Figure A-1- Annealed MgH₂ (a) and corresponding diffraction patterns for (b) newly exposed and (c) after 3.6 C/cm². Simulation is for Mg and dashed line is 002_{MgO}. Ring in (a) designates selected area. 101
- Figure A-2- Milled MgH₂ powder (a) and corresponding diffraction patterns for (b) newly exposed –simulation for MgH₂- and (c) after 2.6 C/cm² –simulation for Mg. 102

Figure A-3- Change in intensity of 110-MgH₂ reflections with increasing electron dose for annealed and milled samples.

List of Symbols

Symbol	Meaning [Unit]
μ	Chemical potential [J/mol]
P	Pressure [bar <i>or</i> atm <i>or</i> MPa]
T	Temperature [K <i>or</i> °C]
c	Concentration [Volume or weight percent]
H	Enthalpy [J <i>or</i> J/mol]
S	Entropy [J/K <i>or</i> J/mol.K]
R	Universal gas constant [8.314 J/mol.K]
ζ	Fraction reacted
t	Time [sec]
ρ	Dislocation density [$/m^2$]
b	Burgers vector [\AA]
D	Grain size (Average diameter) [μm <i>or</i> nm]
e	Microstrain
G	Shear modulus [GPa]
E	Elastic modulus [GPa]
Φ	Heating rate [°C/min]

List of Abbreviations

Abbreviation	Meaning
ARB	Accumulative roll bonding
BSE	Back-scattered electron
DFT	Density functional theory
DSC	Differential scanning calorimetry
EELS	Electron energy loss spectroscopy
EFTEM	Energy-filtered transmission electron microscopy
FR	Fold and roll
IBA	Integral breadth analysis
JMA	Johnson-Mehl-Avrami
JMAK	Johnson-Mehl-Avrami-Kolmogorov
MWP	Multiple whole profile
NG	Nucleation and growth
SAD	Selected area diffraction
SEM	Scanning electron microscopy
SS	Stainless steel
TEM	Transmission electron microscopy
TGA	Thermo-gravimetric analysis
UHV	Ultra-high vacuum
XRD	X-ray diffraction
ZA	Zone axis

Chapter 1

Introduction

1-1- Hydrogen as an energy vector

Fossil fuels have been powering our growth and development since the Industrial Revolution in the 18th century. By looking at today's distribution of primary energy production (Figure 1-1) we realize that more than 85% of global energy originates from the underground fossil-based reservoirs. That includes crude oil and natural gas plant liquids, coal, and natural gas. This acute monopolization in our primary energy source has caused numerous difficulties, e.g. excessive carbon dioxide emission and global warming, environmental hazards involved in off-shore drilling and spills, dependence on fragile political administrations governing the oil rich regions of the world, and unsustainable nature of these resources. It might be safe to claim that making the transition towards a sustainable, environment-friendly primary source(s) of energy is the major challenge facing our modern civilization.

One potential way forward is diversification and decentralization of the energy resources [1]. So instead of massive hubs of generating energy (i.e. power plants), we would have localized, widespread center-points each generating relatively small packs of

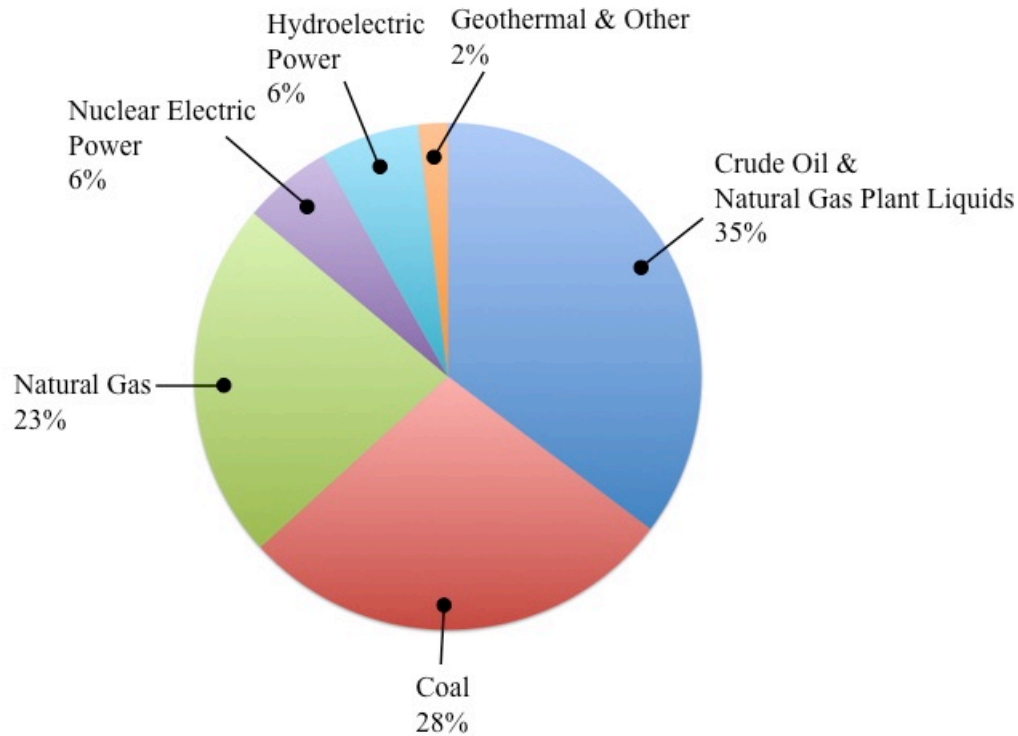


Figure 1-1- World primary energy production (1970-2007) categorized by source. Data gathered from [2].

energy with smaller carbon footprint, preferentially via “green” techniques like hydro, wind, wave, solar, biomass and geothermal. It is in this context that hydrogen as a vector for energy provides a promising pathway.

By definition, an energy vector “allows to transfer in space and time, a quantity of energy” [3]. Examples for existing energy vectors include electricity and heat exchanging fluids. In other words, an energy vector would facilitate storage (“transfer” in time) and transportation (transfer in space) of energy, both in short and long ranges. Figure 1-2 schematically demonstrates how hydrogen fits this outlook. One of the more attractive aspects of hydrogen in this respect is its compatibility with the intermittent nature of the renewable pathways to generate energy. The excess energy produced in peak hours can be stored as hydrogen and used during peak demand time. This concept is now gradually being put to use in remote, off-the-grid communities with access to renewable recourses for energy. One example of a recently initiated such system is the *Hydrogen Assisted Renewable Power* (HARP) project in Bella Coola community, British Columbia. Using this facility Bella Coola, which is not connected to BC Hydro’s provincial electricity

grid, can use its available run-of-the-river hydropower to generate hydrogen via electrolysis, store the hydrogen for the peak demand time and generate the required electricity using fuel cells [4].

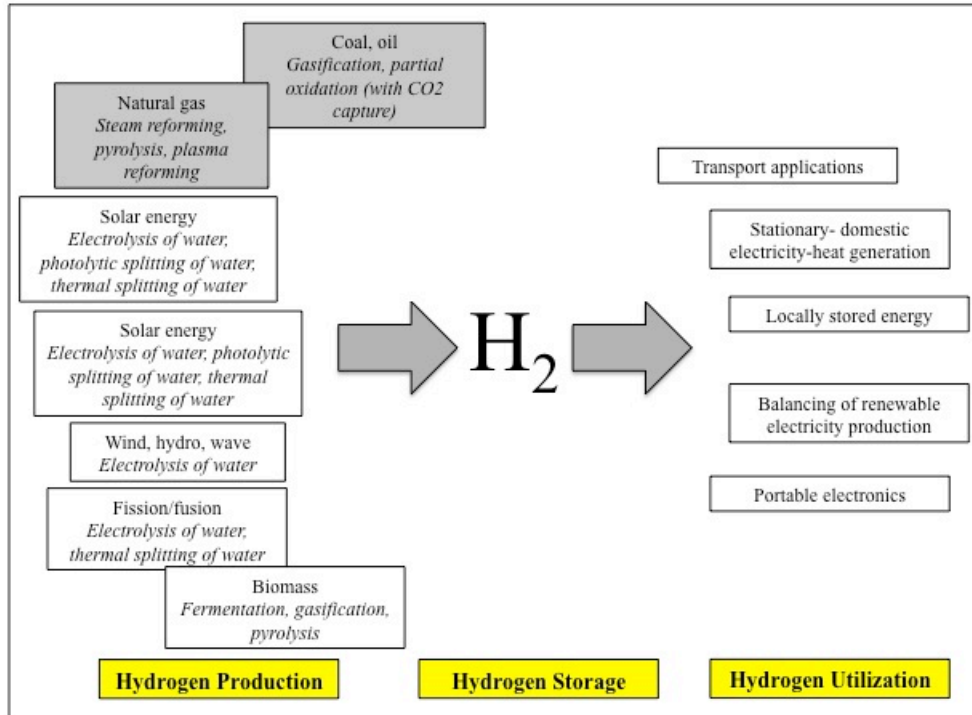


Figure 1-2- Hydrogen as an energy vector, connecting various production techniques to the final utilization. Shaded boxes for production also entail significant carbon dioxide emission (Adapted from [1])

In order for the realization of this hydrogen-centered energy system, hydrogen storage plays a vital role. Reliable mechanism for the storage of hydrogen, with minimum energy expenditure and maximum safety, is the crucial link between “clean” hydrogen production and its end-user utilization.

1-2- Hydrogen Storage

Depending on the final application of the stored hydrogen, the operating requirements of the hydrogen storage system can wildly vary. If the storage system is meant to be integrated into an on-board transportation circuit the constraints are much more stringent compared to a stationary storage unit. Some of these requirements for

hydrogen storage system intended for transportation applications can be mentioned as below [1]:

- Low operating pressure (less than 4 bar)
- Operating temperature within the range of -50 to 150°C
- Reversibility (i.e. being able to absorb/desorb hydrogen for not less than 500 cycles)
- High gravimetric and volumetric hydrogen densities (around 9 wt.% and greater than or equal to 70 g of H₂ per liter of storage system)

The imposed design constraints for stationary applications are less aggressive, compared to above, allowing for higher operating temperatures and pressures. They can also take up large spaces.

Categorically, the following are the storage options for hydrogen, as described by the United States' Department of Energy [5]:

- Gaseous and liquid hydrogen storage
- Material-based hydrogen storage

Currently the pressurized hydrogen gas and cryogenically liquefied hydrogen are the two main commercially available options for hydrogen storage. Steel cylinders can store hydrogen at 200 bar, reaching a gravimetric density of around 1 wt.% of hydrogen. Using the modern carbon fiber composite cylinders we can now reach hydrogen pressures in the range of 700-1000 bar, yielding gravimetric density of up to 10 wt.% of hydrogen [1]. Besides the hazards- both real and publicly assumed- of operating at these high hydrogen pressures, the energy cost to reach these pressures leave the above options in a less competitive state. Another deficiency of the gas and liquefied hydrogen storage systems is low volumetric density, despite their acceptable gravimetric capacity. This can be a major impediment when volume constraints are imposed on the design of the storage system, e.g. in transportation application.

To alleviate the concerns regarding working with high-pressure hydrogen gas and also to increase the volumetric density of the storage systems research is focused on the so-called "material-based" hydrogen storage systems. The idea being that by using the interaction of hydrogen with various materials, one can reach a higher density of hydrogen atoms as compared to the gas phase. Depending on the nature of the interaction

between hydrogen and the host material, one can extract the stored hydrogen by applying a change in a physical parameter of the system, e.g. temperature or partial hydrogen pressure.

Material-based hydrogen storage can be categorized as below [5]:

- Metal hydrides
- Chemical hydrides
- Carbon-based materials, high surface area materials

Metal hydrides provide a possibility to reversibly store and extract hydrogen via the hydride formation and decomposition reaction, respectively. This is the focus of the present thesis and will be studied in detail in the following sections. Chemical hydrides are used in a technology (the technology is referred to as *Chemical Hydrogen Storage*) where hydrogen is produced by the chemical reaction of a hydride, generally with water or an alcohol. This reaction is not easily reversible and the “by-products” of the hydrogen generation reaction should be regenerated in a plant. The last category, carbon-based and high surface area materials, takes advantage of the small surface forces to adsorb hydrogen molecule on large surface area materials, e.g. metal organic frameworks (MOF) or different forms of carbon. As the magnitude of these surface interactions are small, these storage techniques only operate at low temperatures ($\sim 77\text{K}$ for MOFs).

1-3- Hydrogen in Metals

Once exposed to an oxide-free surface of a metal, hydrogen molecule can dissociate into atomic hydrogen and interstitially diffuse into the metallic crystal structure [6]. The following reaction demonstrates this process:



Usually though the surface of the metal is covered with a layer of oxide or hydroxide that prevents the prompt dissociation and penetration of hydrogen into the

metal. Hence, for the above reaction to proceed, we first need to break through the oxide layer by increasing the hydrogen pressure or temperature. This process is sometimes referred to as *activation* [7]. After the introduction of the atomic hydrogen to the metal, it can diffuse within the structure with high diffusivity rates even at room temperature. This fast diffusivity of H atom in metals can be mainly linked to the interstitial nature of the dissolved hydrogen atoms, and as a result its diffusion not being controlled by vacancy concentration [6].

1-3-1- Thermodynamics of hydride formation

Many metals react with hydrogen to form hydrides. Depending on the nature of the metal-hydrogen bonding, these hydrides can be classified into three main groups [P. 88 in Ref. 8]: ionic, covalent, and metallic.

Ionic hydrides (also known as *saline hydrides*) are the hydride of the alkali and alkaline earth metals with large electropositivity. These hydrides are generally crystalline with high heats of formation and high melting points. Covalent hydrides (group BX, and Group AIII to AIV in the periodic table) can be solid, liquid or gaseous. Prominent covalent hydride formers include carbon, silicon, boron and the halogens. The bonding between the element and hydrogen is the non-polar electron-sharing covalent type. Metallic hydrides, formed mainly by the first three columns of the transition metals (BI to BIII) and also Pd and Ni, are formed by the continuous interstitial dissolution of hydrogen within the metallic structure and subsequent phase transformation to the hydride phase once the corresponding stoichiometric ratio has been reached (e.g. ZrH₂, VH, VH₂, PdH). The bonding character in these hydrides is metallic.

The thermodynamics of metal hydride formation can be demonstrated using the pressure-composition isotherms (Figure 1-3-A). At low concentrations of dissolved hydrogen in the metal (region I in Figure 1-3-A), thermodynamic equilibrium of the reaction (1-1) above requires the following:

$$\frac{1}{2} \mu_{H_2}(P,T) = \mu_H(P,T,c) \quad (1-2)$$

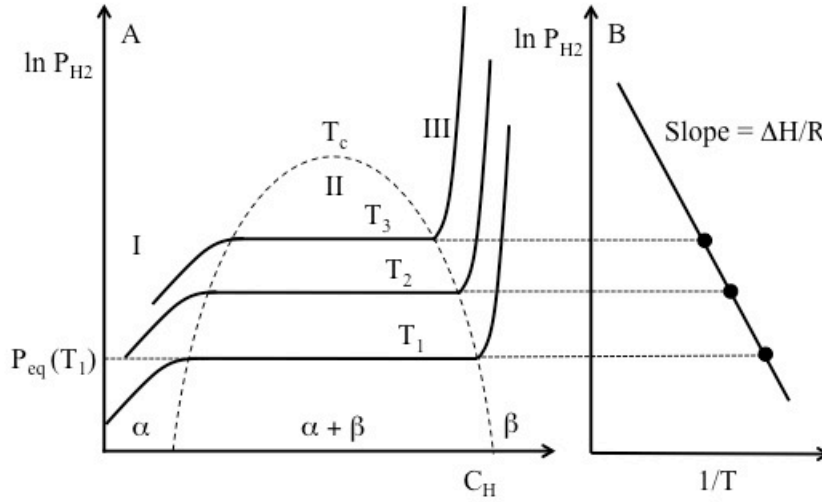


Figure 1-3- (A) Schematic pressure-composition isotherm diagram, with α marking the solid solution of hydrogen in metal and β the hydride. (B) van't Hoff plot for calculating the enthalpy of hydride formation ΔH . (Adapted from [7])

where μ_{H_2} and μ_H are the chemical potentials of molecular hydrogen and of the atomic hydrogen in the solid solution, respectively. At low pressures ($P < 100$ bar) hydrogen can be approximated to be an ideal gas. This would allow us to write:

$$\mu_{H_2} = H_{H_2}^0 - TS_{H_2}^0 + RT \ln P_{H_2} \quad (1-3)$$

where $H_{H_2}^0$ and $S_{H_2}^0$ are the enthalpy and the entropy of the hydrogen gas at the standard state. For the chemical potential of the dissolved hydrogen the following holds:

$$\mu_H = H_H - TS_H^{id} + RT \ln \left(\frac{c}{b-c} \right) \quad (1-4)$$

here H_H is the enthalpy and S_H^{id} is the vibrational (non-configurational) entropy of the hydrogen in solid solution. The last term in equation (1-4) is the configurational entropy. There, b denotes the number of interstitial sites per M atoms ($c=H/M$). Now if we apply the equilibrium condition, i.e. equation (1-2) we reach the condition below:

$$\Delta H_H - T\Delta S_H = RT \ln P^{1/2} + RT \ln \left(\frac{b-c}{c} \right) \quad (1-5)$$

where $\Delta H_H = H_H - \frac{1}{2}H_{H_2}^0$ and $\Delta S_H = S_H^{id} - \frac{1}{2}S_{H_2}^0$. In region I of Figure 1-3-A, since we are dealing with dilute solutions, i.e. $c \ll b$, we can simplify equation (1-5) as below:

$$c = K \cdot P_{H_2}^{1/2} \quad (1-6)$$

This equation is known as the Sievert's Law, and K is the Sievert's constant. At higher hydrogen concentrations the hydride phase (β) starts to nucleate (region II in Figure 1-3-A), generally with a different crystal structure of that of the metal and the solid solution. In this stage the system has three phases present (α , β , and the hydrogen gas), with two components (metal and hydrogen). Referring to the Gibbs phase rule as stated below:

$$f = C - P + 2 \quad (1-7)$$

where f is the degree of freedom in the system, C the number of components, and P the number of phases, respectively, we reach the degree of freedom of one. Hence in the two-phase region, at a given temperature the hydrogen pressure is constant (as depicted in Figure 1-3-A). This equilibrium pressure is related to the enthalpy (ΔH) and entropy (ΔS) of the hydride phase formation ($\alpha \rightarrow \beta$) through the Van't Hoff equation below:

$$\ln \left(\frac{P_{eq}}{P_{eq}^0} \right) = \frac{\Delta H^0}{R} \cdot \frac{1}{T} - \frac{\Delta S^0}{R} \quad (1-8)$$

Since this reaction involves moving from an initial gas phase (hydrogen) to a final crystalline hydride phase (β), the entropy change is approximately equal to the standard entropy of hydrogen ($S^0=130 \text{ J/K.mole}$ [P. 192 in Ref. 8]). So the change in entropy term can safely be deemed constant, independent of the metal that is forming the hydride. The

enthalpy change in the hydride formation reaction can be calculated by plotting $\ln(P_{eq})$ at different temperatures versus $1/T$ and measuring the slope of the resulting trend line. This slope, based on the Van't Hoff equation, is equal to $(\Delta H/R)$. This approach is also schematically demonstrated in Figure 1-3-B.

1-3-2- Kinetics of hydride formation

In order for the hydride phase (β) to form, the applied hydrogen pressure should be above the equilibrium pressure P_{eq} . The “driving force” for the hydrogenation reaction can then be defined as the deviation from the equilibrium pressure, or:

$$\Delta P = P_{H_2} - P_{eq} \quad (1-9)$$

The kinetics of the reaction can be expressed in terms of the ratio of the reacted portion of the material to that of the original initial amount (reacted fraction: ζ). The rate at which the reaction proceeds can be correlated to the driving force. The nature and degree of this dependence is linked to the rate-limiting step in the reaction.

The approach generally taken for studying the kinetics of the hydrogenation reaction (or any other diffusive phase transformation) is known as the Johnson-Mehl, Avrami, Kolmogorov (JMAK) equation [9] as given below:

$$\zeta = 1 - \exp\left(\frac{-t}{\tau}\right)^n \quad (1-10)$$

In the equation above, the time constant τ is determined from the rates of nucleation and growth. The exponent n in the JMAK equation can be determined by curve fitting the experimental data and its value points to the mode of nucleation and growth [10]. Table 1-1 correlates different n values to various states of nucleation and growth. As can be observed in this table, the disadvantage of this “overall kinetics” approach is that same values of the exponent n can imply multiple potential mechanisms in nucleation and growth. Hence direct observation at different stages of the phase

transformation provides a much clearer picture of the kinetic details of the phase transformation.

Table 1-1- Values of n in the JMAK equation as correlated to the modes of nucleation and growth (adapted from [10]).

(A) Polymorphic changes, discontinuous precipitation, eutectoid reactions, interface controlled growth, etc.

Conditions	n
Increasing nucleation rate	>4
Constant nucleation rate	4
Decreasing nucleation rate	3-4
Zero nucleation rate (saturation of point sites)	3
Grain edge nucleation after saturation	2
Grain boundary nucleation after saturation	1

(B) Diffusion controlled growth

Conditions	n
All shapes growing from small dimensions, increasing nucleation rate	>2.5
All shapes growing from small dimensions, constant nucleation rate	2.5
All shapes growing from small dimensions, decreasing nucleation rate	1.5-2.5
All shapes growing from small dimensions, zero nucleation rate	1.5
Growth of particles of appreciable initial volume	1-1.5
Needles and plates of finite length dimensions, small in comparison with their separation	1
Thickening of long cylinders (needles)	1
Thickening of very large plates	0.5
Precipitations on dislocations	-0.67

1-4- Magnesium as a Hydrogen Storage Medium

Magnesium-hydrogen phase diagram at 1 bar hydrogen pressure is shown in Figure 1-4 below. At atmospheric pressure, hydrogen has little solubility in magnesium. The stoichiometric magnesium hydride in standard conditions, α -MgH₂, has a Rutile-type crystal structure. This phase can undergo multiple polymorphic phase transitions under increasing pressure. Table 1-2 lists the crystallographic information of metallic magnesium and all those variations of MgH₂ [11].

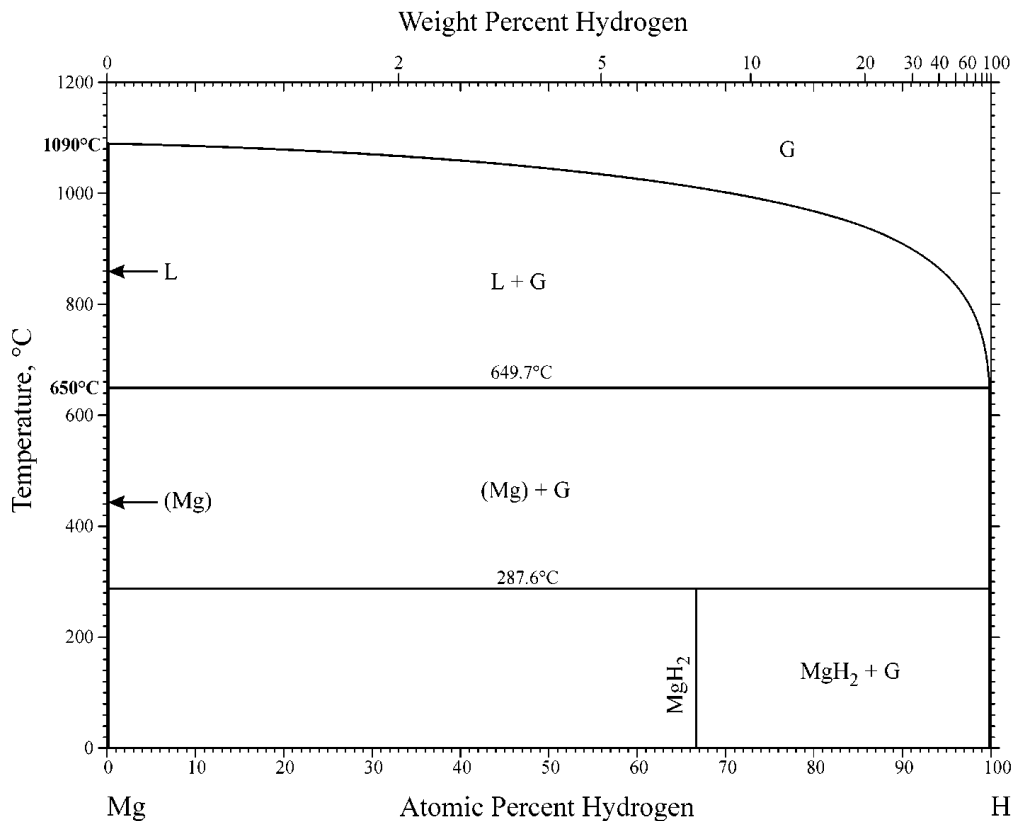


Figure 1-4- Magnesium-hydrogen phase diagram at 1 bar hydrogen pressure [12].

Table 1-2- Crystallographic data for Mg and MgH₂ polymorphs (adapted from [11]).

Phase, structure type	Unit cell (Å)			Wyckoff positions
	a	b	c	
Mg, P6 ₃ /mmc	3.2094	3.2094	5.2103	Mg (2c): 0, 0, 0
α-MgH ₂ , Rutile P4 ₂ /mnm	4.5176	4.5176	3.0206	Mg (2a): 0, 0, 0 H (4f): 0.304, 0.304, 0
β-MgH ₂ , Modified CaF ₂ , Pa-3	4.6655	4.6655	4.6655	Mg (4a): 0, 0, 0 H (8c): 0.3429, 0.3429, 0.3429
γ-MgH ₂ , Pbcn	4.5246	5.4442	4.9285	Mg (4c): 0, 0.3313, 0.25 H (8d): 0.2727, 0.1089, 0.0794
δ'-MgH ₂ , Pbca	8.8069	4.6838	4.3699	Mg (8c): 0.8823, 0.0271, 0.2790 H1 (8c): 0.7970, 0.3765, 0.1651 H2 (8c): 0.9738, 0.7433, 0.5207

The calculated pressure for α-to-γ transition is 0.387 GPa, and for γ-to-β transition this pressure is around 3.84 GPa. The transformation to δ' happens at yet higher pressures. It will be discussed (in Chapter 2) that one of these high pressure phases

(γ -MgH₂) can also form during a high impact energy powder processing technique, called high-energy ball milling. The hydride phase that is stable at standard condition, α -MgH₂, has an enthalpy of formation of $\Delta H = -74.4$ kJ/mole [13]. Using the Van't Hoff equation (equation (1-8) above), this would yield the equilibrium desorption (or: decomposition) temperature of 279°C at 1.013 bar (1 atm) of hydrogen pressure. As mentioned above, this temperature is too high for any potential on-board storage application (Target temperature for transportation applications: -50 to 150°C).

But for stationary applications, magnesium with the ideal gravimetric hydrogen capacity of 7.6 wt.% is considered to be competitive. The main hindrance for the widespread use of magnesium in storage systems is the slow kinetics in its absorption and desorption reactions. Also the first absorption cycle for the as-prepared powder is extremely slow (*Activation period*) [7]. Even after activation, the sorption kinetics of pure magnesium remains poor. The main reason for this sluggish kinetics is the very small dissociation probability of H₂ molecule on the surface of non-transition metals [14]. It has been demonstrated that one route to enhance the (de)hydrogenation kinetics in magnesium is using severe plastic deformation techniques [15]. This can also be achieved by the addition of catalytic species to facilitate the dissociation of the molecular hydrogen. The combination of the two approaches above has yielded enhanced magnesium-based storage systems. Recent developments in this respect have now resulted in a few commercially available magnesium-based stationary hydrogen storage systems (See [16] as an example).

1-5- The Motivation and Scope of this thesis

In the present thesis we are looking at two severe plastic deformation processes that can be utilized to enhance the hydrogen sorption kinetics of magnesium, i.e. high-energy ball milling and accumulative roll bonding. Below, an overview of each of these techniques is provided.

High-energy ball milling is a powder processing technique used for pulverization, mixing, alloying or formation of metastable phases [17]. There are number of designs available as for the geometry of the milling equipment. In the present research our focus

is on planetary configuration of this technique (See Figure 1-5-A). In this technique, the powder sample, along with the grinding balls, is loaded in a milling vial, usually made from the same material as the balls. The mounted vial is then rotated in a planetary fashion, as schematically shown in Figure 1-5-B, with both orbital and rotational motions. This motion pattern results in high-energy impingements of the balls onto the target specimen powder, yielding repeated welding, fracture, and re-welding of the powders.

In Chapters 2 and 3 of this chapter we will study high-energy ball milling of magnesium hydride powder. A short duration of ball milling can significantly enhance the sorption kinetics of the hydride powder. Our motivation in approaching this phenomenon is attempting to correlate this final improvement in the property of the hydride phase to parameters and features in the microstructure. Knowing this correlation and the potential mechanism will enable us to optimize our preparation techniques, such that they would yield better final sorption properties.

In Chapter 4, we will study accumulative roll bonding the preparation of magnesium-based composites for hydrogen storage applications. Accumulative roll bonding was originally developed to fabricate bulk nanostructures of single-phase metals and alloys [18]. This was achieved by repetitive rolling and folding (or cutting and restacking) of that metal or alloy in sheet form (See Figure 1-6-A for the schematic).

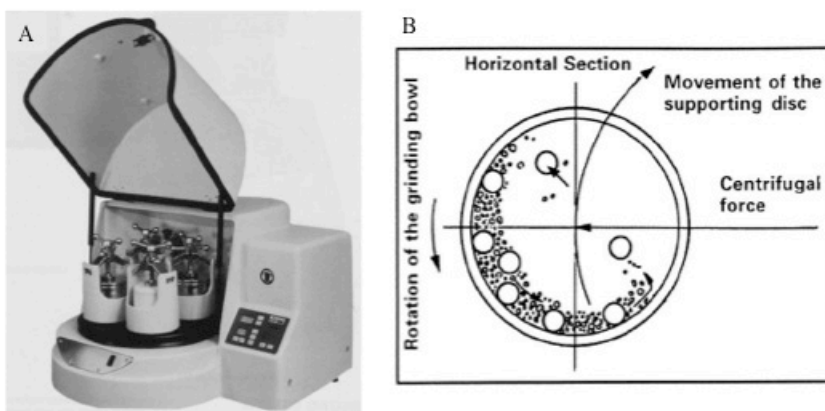


Figure 1-5- (A) a typical planetary ball mill machine, (B) schematic of the movement pattern within the vial of an operating planetary milling machine (Taken from [17]).

In our approach, we use the accumulative roll bonding methodology to prepare magnesium-titanium and magnesium-stainless steel (SS) composites. Figure 1-6-B provides a schematic for the adopted technique for the preparation of the Mg-Ti composites (details to be discussed in Chapter 4). In this section of the thesis we shift our outlook from hydride phase powder processing to that of the preparation of the magnesium in metallic state. Also we aim to design our composite preparation technique such that it would be directly transferable to an industrial set-up. Our motivation in this part of our research is to study the metal to hydride phase transformation and how it can be kinetically tuned by adding varying amounts of the secondary phase (Ti and SS) in the composite.

In both of the cases, ball milling of the magnesium hydride powder and ARB of Mg-Ti and Mg-SS composites, our emphasis is the detailed characterization of the microstructure and its correlation with the resulting hydrogen sorption properties.

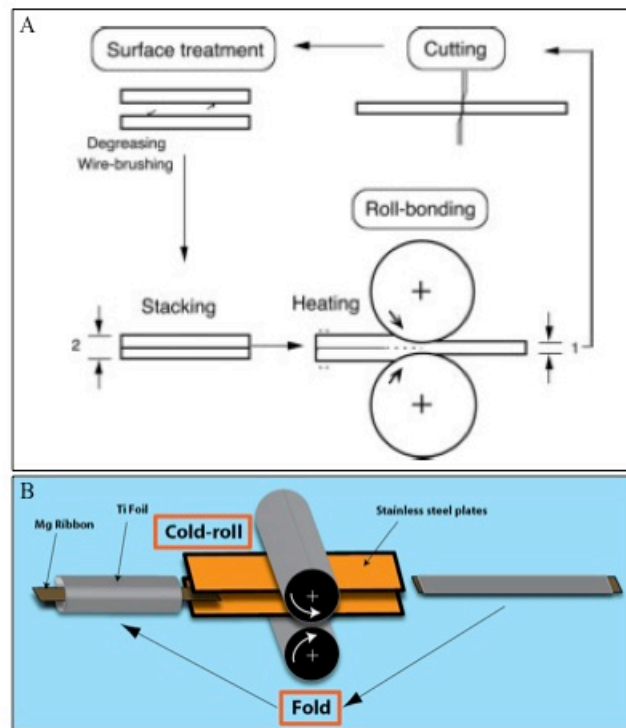


Figure 1-6-(A) Schematic of the accumulative roll bonding processing (Taken from [18]), (B) Schematic of the procedure we used for preparing Mg-Ti multilayered composites (See chapter 4).

1-6- References

-
- 1 Edwards PP, Kuznetsov VL, David WIF. *Philosophical Transactions of the Royal Society A* 2007; 365: 1043-1056.
 - 2 United States Energy Information Administration, Annual Energy Review, Annual Energy Review 2009, Report No. DOE/EIA-0384(2009), Release Date: August 19, 2010. <http://www.eia.doe.gov/emeu/aer/inter.html>
 - 3 Orecchini F. *International Journal of Hydrogen Energy* 2006; 31: 1951-1954.
 - 4 General Electric's Press release regarding *Clean Energy Powers Bella Coola, B.C. (9 September 2010)*
<http://www.genewscenter.com/content/Detail.aspx?ReleaseID=10947&NewsAreaID=2>
 - 5 US-DOE Hydrogen Storage Program Web-page:
<http://www1.eere.energy.gov/hydrogenandfuelcells/storage/index.html>
 - 6 Kirchheim R. *Solid State Physics* 2004; 59: 203-291.
 - 7 Huot J (2010) "Metal hydrides", in *Handbook of Hydrogen Storage: New Materials for Future Energy Storage* (Hirscher M, Hirose K, Eds), P. 81, Wiley-VCH, Weinheim.
 - 8 Zuttel A, Borgschulte A, Schlapbach L, Chorkendorff Ib, Suda S (2008) "Properties of Hydrogen" in *Hydrogen as a Future Energy Carrier* (Zuttel A, Borgschulte A, Schlapbach L, Eds), P. 88, Wiley-VCH, Weinheim.
 - 9 Doherty RD (1996) "Diffusive Phase Transformations in the Solid State", in *Physical Metallurgy* (Cahn RW, Haasen P, Eds), 4th revised and enhanced edition, P. 1435, Elsevier Science.
 - 10 Christian JW. *The Theory of Transformations in Metals and Alloys*, P. 546, 3rd Edition, Oxford: Pergamon; 2002.
 - 11 Vajeeston P, Ravindran P, Hauback BC, Fjellvag H, Kjekshus A, Furuseth S, Hanfland M. *Physical Review B* 2006; B73: 224102.
 - 12 Okamoto H. *Journal of Phase Equilibria* 2001; 22(5): 598-599.
 - 13 Stampfer JF, Holley CE, Suttle JF. *Journal of the American Chemical Society* 1960; 82(14): 3504-3508.
 - 14 Schlapbach L. (1992) "Surface Properties and Activation", in *Hydrogen in Intermetallic Compounds II* (Schlapbacl L, Ed), pp. 15-95, Springer-verlag, Berlin.

15 Leiva DR, Fruchart D, Bacia M, Girard G, Skryabina N, Villela ACS, Miraglia S, Santos DS, Botta WJ. International Journal of Materials Research 2009; 100(12): 1739-1746.

16 The French company, McPhy, is an example. See:
<http://www.mcphy.com/en/index.php>

17 Suryanarayana C. Prog. in Mat. Sci. 2001; **46**: 1-184.

18 Tsuji N, Saito Y, Lee SH, Minamino Y. Advanced Engineering Materials 2003;5(5): 338-244.

Chapter 2

TEM Analysis and Sorption Properties of High-energy Milled MgH₂ Powders

A version of this chapter has been published in: Danaie M, Mitlin D. Journal of Alloys and Compounds 2009; 476(1-2): 590-598.

DOI: <http://dx.doi.org/10.1016/j.jallcom.2008.09.078>

2-1- Introduction

Magnesium hydride (MgH₂) holds promise for solid-state hydrogen storage due to its high capacity for hydrogen (7.6 wt. %), relatively low price and abundance. However, this hydride's poor sorption kinetics impedes its widespread utilization. High-energy mechanical ball milling is known to enhance the sorption kinetics of magnesium hydride powder [1]. The milling process changes the powder microstructure, but in ways which are still subject to debate. Gaining additional insight regarding the microstructural evolution during milling is important both scientifically and from a process optimization perspective. The fact that mechanical milling is also frequently used for alloying and dispersing the catalyst materials in powder systems makes this knowledge even more critical.

Lattice strain, powder particle size and grain size of the powder all change simultaneously during milling. Additional microstructural defects, possibly also important for sorption, may be introduced by the milling process. Accurate measurement of these parameters, each with potential effects on final desorption properties, poses a materials characterization challenge. There is no clear consensus among the researchers in terms of which microstructural parameters play the major role in determining the desorption kinetics. Some groups report that desorption kinetics show a drastic enhancement when particle size falls below a threshold value, while grain size reduction is almost ineffective [2, 3]. Others believe that decrease in both particle and grain size would result in lower desorption temperatures [4]. Some researchers even report a deterioration of desorption kinetics upon decreasing the grain size of the powder particles [5]. The contribution of microstructural defects, such as dislocations, twins or stacking faults, to the enhanced or degraded sorption is generally neglected.

Part of the ambiguity mentioned above stems from the fact that direct microstructural characterization is very difficult to perform on milled hydride powders. The most direct way to quantify microstructural parameters such as grain size and defect type and content is through transmission electron microscopy (TEM) analysis. TEM has been attempted in a number of studies, but with very limited success [6, 7, 8, 9]. This is because at ambient sample temperature, normally used for analysis, magnesium hydride is extremely unstable under an electron beam. Within a minute of beam exposure it transforms into metallic magnesium or to an oxide [8, 9]. This problem is even more acute for the highly mechanically deformed samples [See Appendix I for more discussion on the stability of MgH₂ within the TEM environment].

TEM characterization of large single crystals of undeformed magnesium hydride has been successfully performed using a cryogenic TEM holder [10]. However, nothing similar has been achieved for the more technologically pertinent mechanically milled powders. Instead, the methodology that is most widely utilized to estimate the grain size and the defect content in hydride powders is an indirect approach of de-convoluting the different contributions to x-

ray diffraction (XRD) peak broadening. Scanning electron microscopy (SEM) is often used a complementary tool for particle size analysis. Using the XRD peak broadening approach is accompanied by some assumptions and restrictions. XRD analysis yields a single mean value for the grain diameter, assuming a spherical morphology of the grains. While this type of analysis is useful for predicting general trends during milling, the exact grain size values should be interpreted cautiously. This is because the presence of twins and stacking faults in the microstructure results in a reduced measured grain size diameter, relative to what one would directly observe using TEM [11]. Furthermore, XRD does not provide information about the type, scale or distribution of such defects in the microstructure.

The goal of the present study is to apply the direct observation technique of cryogenically cooled TEM to analyze MgH₂ powder in its milled state and after subsequent annealing. By combining direct observations via TEM with more conventional techniques used for hydride analysis such as Differential Scanning Calorimetry (DSC) / Thermo-gravimetric Analysis (TGA), XRD and particle size statistics, we are able to provide a more comprehensive description of the hydride microstructures and ultimately aid in the development of improved powder formulations.

2-2 Experimental Procedures

Magnesium hydride (MgH₂) powder was purchased from Gelest Inc. with 97 wt.% purity, the balance being magnesium. Two batches of powder were milled for 30 minutes in a Fritsch Pulverisette 6 planetary mono-mill. We used 10:1 ball to powder weight ratio, with agate balls and vial, at 650 rpm rotation speed. All powder milling and handling steps were performed in a dry argon glove box. Half of the milled batches were then annealed at 400°C and hydrogen pressure 2 MPa for two different times, 2 hours and 16 hours. The four types of powders that were analyzed are the as-received magnesium hydride, the milled

magnesium hydride, and the milled and subsequently annealed magnesium hydride for 2 and 16 hours.

We used a simultaneous differential scanning calorimeter (DSC) and thermo-gravimetric analyzer (TGA) (SDT Q600, TA Instruments) to monitor the desorption behavior of the powder samples. During thermal analysis, the powders were held in alumina cups and heated to 600°C with 10°C/min heating rate. The analysis was performed under constant flow of argon to prevent oxidation. All four batches were exposed to air for approximately 24 hours prior to testing, so as to obtain a consistent degree of oxidation on the powder surfaces.

We used a Malvern 2000SM Mastersizer laser scattering particle size analysis system to obtain quantitative MgH₂ particle size distributions. The manufacturer specified resolution range of the system was sub- μm to 2 mm. An anhydrous alcohol reagent (Anhydrous Ethyl Alcohol 90% \pm 1% v/v; Methyl Alcohol approx. 5% v/v; 2-Propanol approx. 5% v/v as dispersant) was used as suspension media. All samples were ultrasonicated for equal durations prior to the measurement. All measurements were performed in same stirring speed and obscuration level.

For a qualitative analysis of the as-received powders we used scanning electron microscopy (SEM). We used Hitachi S-4800 SEM operating at 7 kV accelerating voltage, and imaging using the secondary electron signal. The powder samples were mounted on conductive carbon tape onto aluminum SEM stubs in an argon glove box before microscopy session.

We used a Bruker-AXS, D8 Discover diffractometer system with an area detector and Cu-K α radiation for X-ray diffraction (XRD) experiments. X-ray diffraction was used for general phase identification. XRD spectra were also analyzed for grain and lattice strain measurement. Integral breadth analysis (IBA) was utilized for de-convoluting the broadening effects of grain size and lattice strain for the powders. Using the following relation [12]:

$$\frac{(\delta 2\theta)^2}{\tan^2 \theta_0} = K\lambda/D \cdot \frac{\delta 2\theta}{\tan \theta_0 \sin \theta_0} + 16e^2 \quad (2-1)$$

and plotting $(\delta 2\theta)^2 / \tan^2 \theta_0$ versus $(\delta 2\theta / \tan \theta_0 \sin \theta_0)$, where $\delta 2\theta$ is the integral breadth of the peaks, and θ_0 is the position of the peak maximum. The grain size (D) and microstrain (ϵ) can be calculated from the fitted line slope and ordinate intercept, respectively. The microstrain peak broadening is due to the presence of dislocations in the material [12]. We used the following α -MgH₂ reflections for the analysis: 110, 020, 121, 130. These peaks were well resolved from those of other potentially present phases, e.g. magnesium and magnesium oxide. Peak fitting was performed on EVATM commercial software. Instrumentation broadening was automatically accounted for in the software used for the analysis.

TEM analysis was performed using a JEOL 2010 microscope, operating at 200kV accelerating voltage. The TEM observations were performed using a cryogenic holder held near 90 K. This was done to significantly increase the stability time of the hydride powder under the electron beam. At cryogenic temperature, sample degradation occurred relatively slowly. Even in the milled sample, which was the least stable, no beam-induced microstructural degradation was observed after 5 minutes of beam exposure in one area. TEM samples were prepared by dry dispersion of the powders on amorphous carbon grids and in argon glove box, directly before the TEM session.

We used the commercial software, Desktop MicroscopistTM, for simulating experimental electron diffraction patterns. The crystallographic data reported in [13] and some data from the XRD database on EVA software were used for generating the simulations (data tabulated in Table 2-1). In the simulation, hydrogen superlattice reflections were excluded since their intensity is significantly less than that of the magnesium. Image analysis software, Image JTM, was used for measuring the grain boundary area of the milled, and milled and 2 hour annealed samples. In both cases, approximately 1000 grains were analyzed. Dark field TEM micrographs were used for the measurement.

2-3- Results

Figure 2-1 shows DSC and TGA results for desorption of the four samples. Judging by either the onset of the endothermic reaction or the onset of appreciable weight loss, a milling cycle of 30 minutes decreased the onset of desorption by approximately 45 °C. However, the subsequently annealed powder samples showed degraded improvements in the desorption kinetics.

Table 2-1- Crystallographic data used for generating electron diffraction simulations [See text for the source].

Phase	Crystal Structure	Unit Cell (nm)			Wyckoff Positions
		a	b	c	
α -MgH ₂	P4 ₂ /mnm (136)	0.45176	0.45176	0.30206	Mg (2a): 0, 0, 0 H (4f): 0.304, 0.304, 0
γ -MgH ₂	Pbcn (60)	0.45246	0.54442	0.49285	Mg (4c): 0, 0.3313, 0.25 H (8d): 0.2727, 0.1089, 0.0794
Mg	P6 ₃ /mmc (194)	0.32095	0.32095	0.52107	Mg (c2): 0, 0, 0
MgO	Fm-3m (225)	0.4227	0.4227	0.4227	Mg (4a): 0, 0, 0 O (4b): 0.5, 0.5, 0.5

In fact, the 16 hour annealed sample had a slightly higher onset of desorption temperature than the as-received powder. The total weight loss difference between the as-received powder and the milled batches is not very significant and may be attributed to the effect of milling. Since milling was performed in argon atmosphere a small portion of the hydride likely has transformed into magnesium due to localized heating and could not be recovered upon annealing. In all three cases, the total weight loss is comparable to what is commonly reported in literature [1, 2, 3, 4, 5, 14].

Figure 2-2 shows the SEM micrographs of the four powder samples. The as-received powder has a “flake-like” morphology, with relatively mono-

dispersed size distribution. Milling does not entirely pulverize the powders, creating a visibly multimodal distribution. Figure 2-3 shows the quantitative particle size distributions of the three powder batches, obtained from the laser scattering measurement. The as-received powder (Figure 2-2A) shows a fairly tight mono-modal particle size distribution, peaked at a particle diameter of 52 μm .

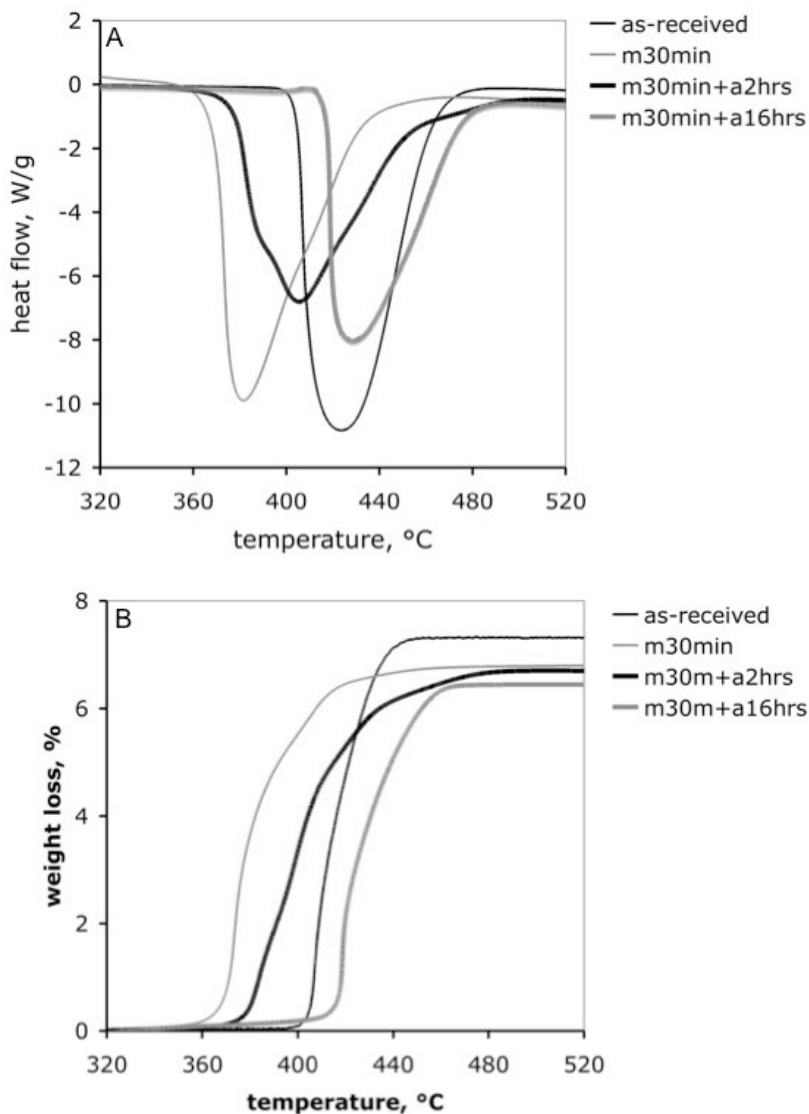


Figure 2-1- (A) DSC and (B) TGA results for the desorption of the as-received hydride, 30 minute milled hydride (m30min), and milled and annealed hydride (m30min-a2hrs and m30min-a16hrs).

After 30 minutes of milling this size distribution is drastically changed. The particle size distribution is multi-modal, with major peaks at 1.7 and 20 μm . Such distribution is attributed to the incompleteness of the milling cycle, where 30 minutes was not enough time to pulverize all the powder. The 30 minute milled distribution also shows a minor presence of particles that are in-fact larger than what was observed in the as-received powder. This is due to agglomeration. The 16-hour annealing cycle causes particle sintering and coarsening. The milling-induced multi-modal size distribution is eliminated, in favor of a broad distribution peaked at 10 μm .

Table 2-2 shows the mean grain size and lattice strain, as obtained from the IBA analysis of the XRD peaks of $\alpha\text{-MgH}_2$. According to IBA analysis, ball milling has reduced the grain size to less than half of its initial value and significantly increased the lattice strain. Performing IBA analysis on both annealed samples yields a negligible value for strain and a grain size comparable to the as-received powder. As will be shown in the subsequent results, the milled microstructure contains twins. This would drive the calculated grain size to a lower mean than for the same grain size distribution in an untwined material [11, 12].

Table 2-2- Mean grain size and lattice strain obtained from the IBA analysis of the $\alpha\text{-MgH}_2$ XRD peaks.

Sample	Average Grain Size (nm)	Lattice Strain
As-received	25	Negligible
Milled	11	5.6×10^{-4}
Milled and annealed for 2 hrs.	21	Negligible
Milled and annealed for 16 hrs.	24	Negligible

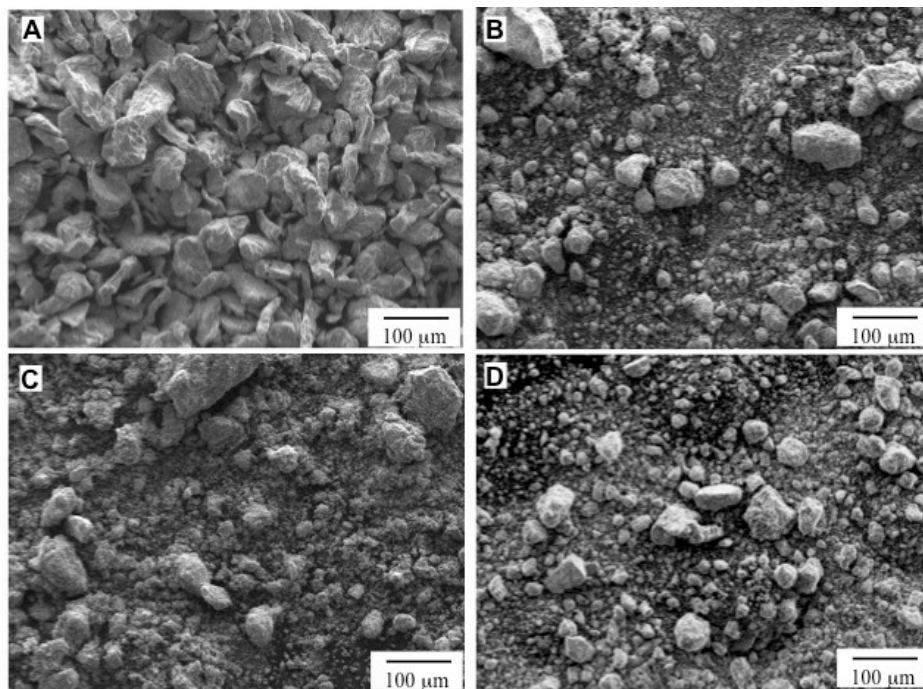


Figure 2-2- SEM micrographs of magnesium hydride powder (A) As-received, (B) Milled for 30 minutes, (C) Milled for 30 minutes and annealed for 2 hours, and (D) Milled for 30 minutes and annealed for 16 hours.

Figures 2-4 through 2-7 display TEM micrographs of the microstructure of the milled MgH₂ powder. The TEM analysis was limited to the sub- μm particles since the larger ones were not electron transparent. The as-received hydride powder particles could not be analyzed because of their large size. The observation made from this analysis will apply to the particles that were pulverized by the milling and hence undergone significant plastic deformation.

Figure 2-4A shows a lower magnification bright field image of a number of particles in the milled hydride powder. Simulation of the selected area diffraction (SAD) ring pattern (Figure 2-4B) indicates that the powder particles are α -MgH₂. Some faint continuous rings from the surface oxide are also present in all the micrographs. On a number of occasions we observed a mixture of α and γ hydride phases in the milled powder, agreeing with the XRD data. However, the γ hydride was by far a minority phase in the microstructure.

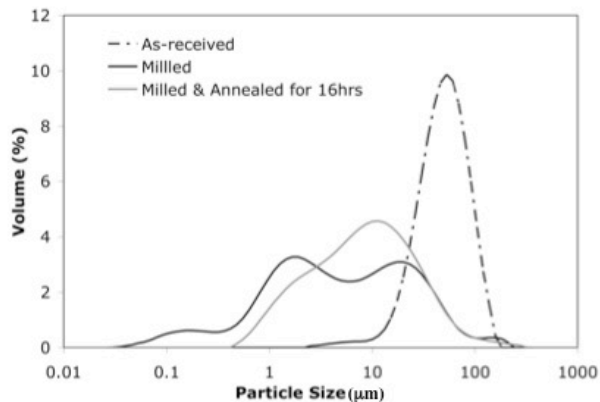


Figure 2-3- Particle size distributions of the as-received, milled and milled and 16hrs annealed MgH₂ powders.

The two common features of the grain structure of the milled powders were irregularly shaped grains of various sizes and larger grains containing nano-scale twins. Figure 2-5 shows an example of a larger α -MgH₂ crystallite (arrowed). The dimension of this particular grain was almost an order of magnitude larger than the mean value reported by XRD, though other grains with comparable dimensions were also observed. Similar grains, of varying dimensions, are the most commonly observed feature of the microstructure. The grain shows mottled (non-uniform, blocky) contrast, previously reported for highly deformed ionic minerals such as phyllosilicates [15, 16].

Figure 2-6 shows an example of an area with a high population of nano-scale twins. Some of these twins are imaged in dark field, using a portion of the streaked twin reflection, arrowed in the SAD. The presence of twins was the prominent feature of the ball-milled microstructure. Researchers have reported twins in ball-milled intermetallic Mg₂NiH₄ [17]. To our knowledge, twins have not been previously observed in ball-milled magnesium hydride powders.

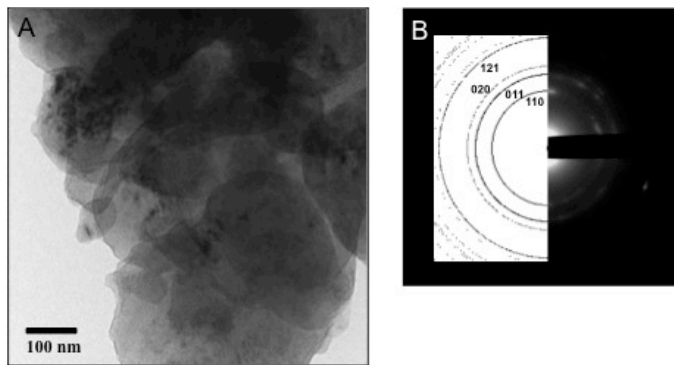


Figure 2-4- TEM micrographs of the milled MgH₂ powder: (A) Bright field image of a cluster of powder particles, (B) corresponding diffraction ring pattern with α -MgH₂ simulation.

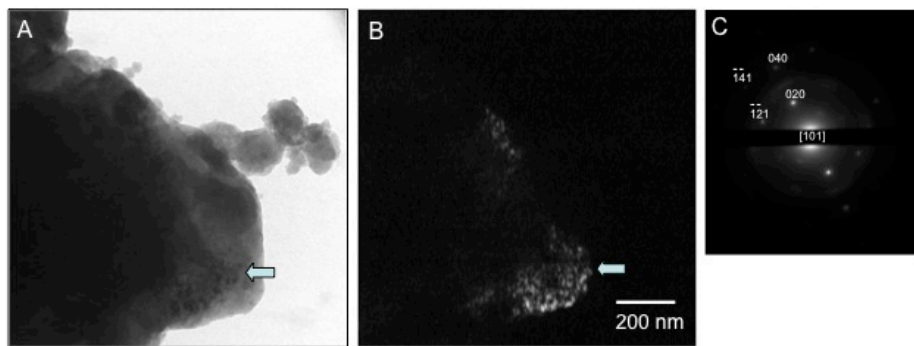


Figure 2-5- TEM micrographs of the milled MgH₂ powder: (A) Bright field image, (B) dark field micrograph, obtained using $g = 020$, of the same area highlighting a typical α -MgH₂ grain within an individual particle (C) corresponding indexed α -MgH₂ SAD.

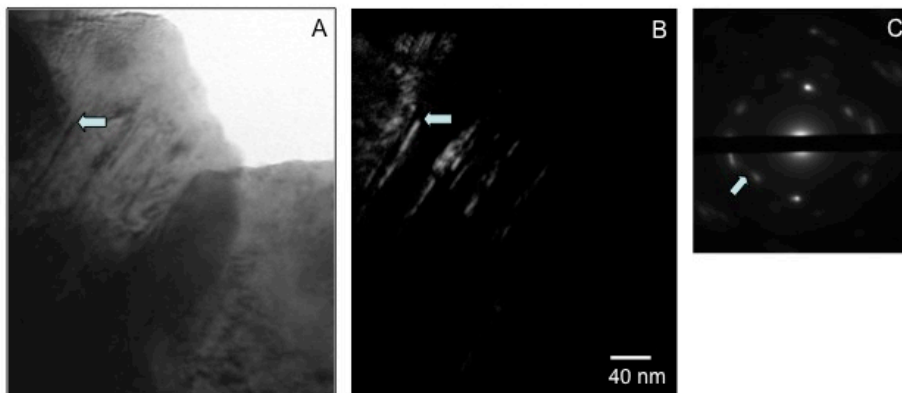


Figure 2-6- TEM micrographs of two overlapping milled α -MgH₂ powder particles: (A) Bright field micrograph; (B) Dark field micrograph highlighting the presence of multiple twins, obtained using the streaked twin reflection (arrowed in (C)).

In addition to areas containing a high density of twins, some grains contained isolated twin segments. This is illustrated in Figure 2-7. The arrow in the bright field – dark field pair point to the same region where an isolated twin was imaged in dark field using a streaked portion (arrowed) of the 110 α -MgH₂ ring pattern. The streaking confirms the high aspect ratio morphology of the imaged crystal.

The microstructure of the milled and annealed powders is shown in Figures 2-8 to 2-13. Figures 2-8 to 2-10 depict the microstructure of the 2 hour annealed specimens, while Figures 2-10 to 2-12 depict the 16 hour annealed specimens. The annealed powders were noticeably more stable under the electron beam than the milled powders.

Figure 2-8 demonstrates that the annealed microstructure mostly consisted of nano-scale α -MgH₂ grains. Similar to the milled powder, the grains ranged in size, and were often significantly larger than the reported XRD mean. As mentioned in the Experimental section, the presence of twins in the microstructure may drive the XRD grain sizes to lower values than what would be directly observed by TEM. TEM analysis detected only a trace amount of γ -MgH₂ phase in the annealed powders. The γ phase was not present in sufficient quantities to be detected by XRD.

Figure 2-9 indicates that twinned sections are still present after 2 hours of annealing. However, they were detected far less frequently after the annealing. A general trend that is observable when comparing the two batches is that the twinned sections detected after annealing were coarser than in the as-milled powders. This can be observed when comparing Figure 2-9 and Figure 2-7, which show twins at the same magnification.

Figure 2-10 shows the same area depicted in figure 2-9, but after a long-term exposure to electron beam. The hydride phase has transformed to a combination of Mg and MgO phases, as observed in the resulting diffraction pattern. Dark filed imaging, using a portion of 01 $\bar{1}$ 1 reflection ring of Mg, reveals that the desorbed grain structure is in a pronounced contrast with the initial grain morphology of the hydride phase. The magnesium grain size is substantially

smaller than the parent hydride phase. This observation is in agreement with the literature [10].

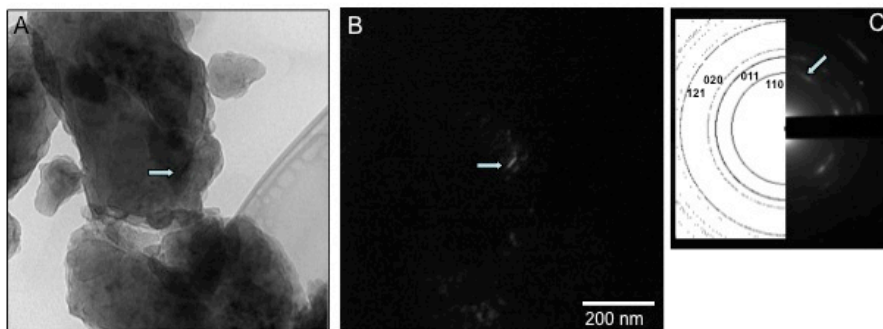


Figure 2-7- TEM micrographs of the milled $\alpha\text{-MgH}_2$ powder demonstrating the presence of nano-scale twins within individual grains: (A) Bright field image; (B) Dark field micrograph of the same area; (C) corresponding SAD of $\alpha\text{-MgH}_2$. Arrows point to the same location in both images and to the portion of the 110_{α} ring pattern used for dark field imaging.

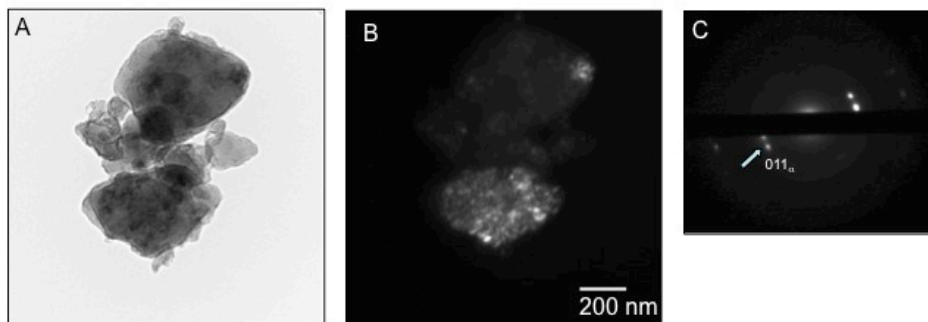


Figure 2-8- TEM micrographs of the milled and 2 hour annealed MgH_2 powder: (A) Bright field micrograph; (B) Dark field micrograph demonstrating the presence of powder particles that are essentially a single crystal. The dark-field image was obtained using the arrowed portion of the $011_{\alpha}\text{-MgH}_2$ reflections (C).

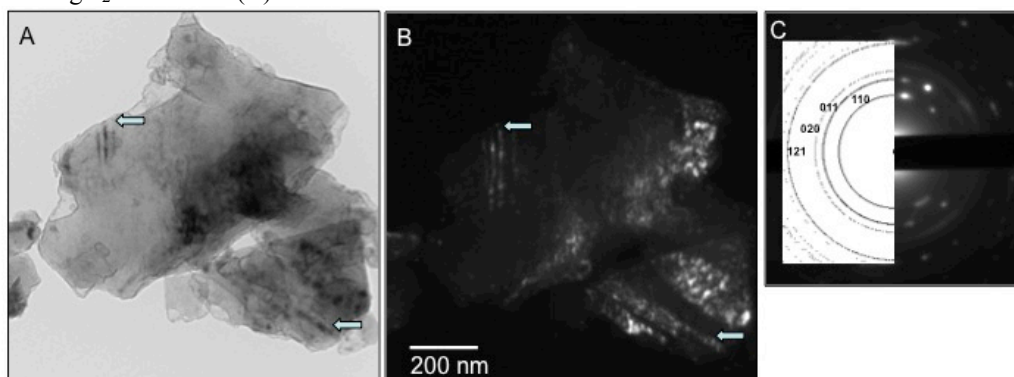


Figure 2-9- TEM micrographs of the milled and 2 hour annealed MgH_2 powder: (A) Bright field micrograph; (B) Dark field micrograph, obtained using a portion of the $011_{\alpha}\text{-MgH}_2$ ring pattern, highlighting the presence of twins (arrowed); (C) corresponding SAD.

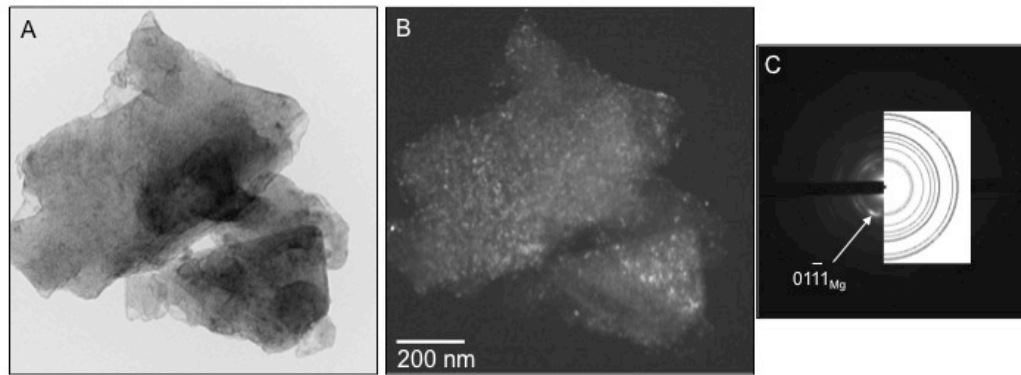


Figure 2-10- TEM micrographs of the the same area observed in figure 2-9 after a long exposure to electron beam: (A) Bright field micrograph; (B) Dark field micrograph, obtained using a portion of the 01-11 Mg ring pattern, showing the fine grain structure of Mg; (C) corresponding SAD. The simulation corresponds to Mg ring pattern. Some rings of MgO can also be observed.

Figure 2-11 shows an example of a relatively large α -MgH₂ single grain in the 16 hour annealed microstructure. The grain did not display twins. Since the grain was far from a symmetric zone axis we were able to image the surface magnesium oxide without the interference of any hydride reflections (See Figure 2-10C). The rings in the SAD are continuous, indicating no preferred texture and a very fine grain size. The individual oxide grains imaged in Figure 2-10C were truly nanoscale, being on the order of single nanometers.

Figure 2-12 shows a series of fine α -MgH₂ grains, which were imaged using a portion of SAD ring pattern. The scale of these grains is similar to the mean value reported by XRD. Another feature of the milled and 16 hour annealed microstructure is the occasional presence of coarse twinned sections. Figure 2-13 shows a bright field – dark field pair of an individual hydride grain, taken near the $[001]_{\alpha}$ zone axis. The dark field image indicates that there is a section of the grain (arrowed) that has a different orientation from the rest of the grain. This section's morphology is consistent with that of being a twin, rather than a separate grain. Its size is much larger than the twins, which were observed in the as-milled material.

From the TEM data we can obtain the grain area distributions in the milled and in the milled and 2 hour annealed powders. Figure 2-14 presents histograms of the grain area distribution of both batches, measured from dark field TEM micrographs using α -MgH₂ reflections. The two distributions look similar, except

for the higher frequency of the large grains in the annealed microstructure. There is a difference in the average grain boundary area per grain between the milled and annealed samples: 65 nm² versus 586 nm².

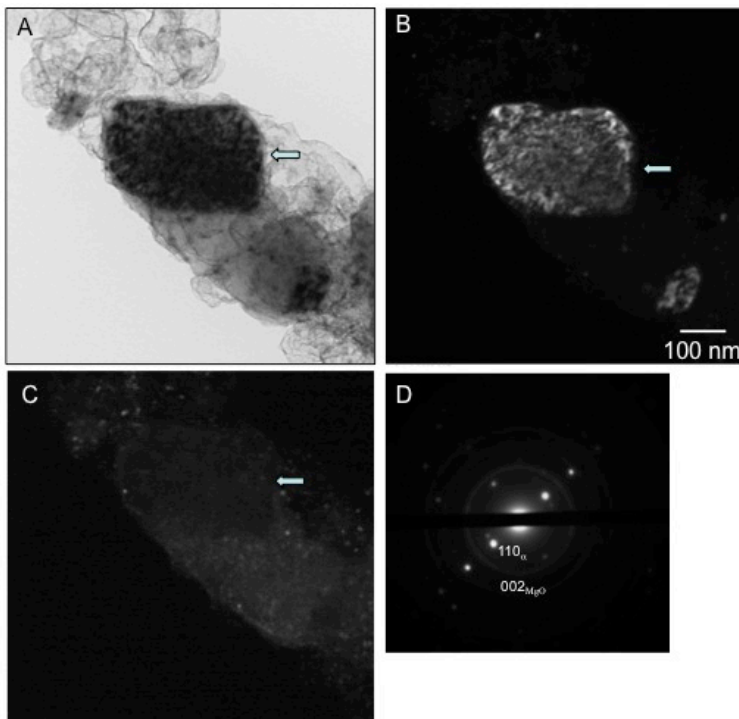


Figure 2-11- TEM micrographs of the milled and 16 hour annealed MgH₂ powder: (A) Bright field micrograph; (B) dark field micrograph, obtained using $g = 110_{\alpha}$ reflection; (C) dark field micrograph obtained using a portion of the 002 MgO ring pattern (first continuous ring), and; (D) corresponding SAD.

Assuming a spherical grain size yields average grain diameters of 4.5 and 13.5 nm. However, observing the area distribution histogram it is evident that the majority of the grains (first two sets of bars) are in the same range. It is the minority presence of larger grains that drives up the average values in the annealed powder.

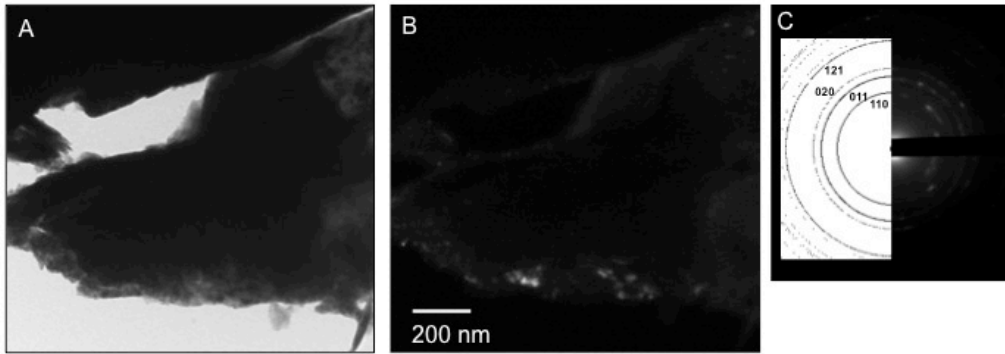


Figure 2-12- TEM micrographs of the milled and 16 hour annealed MgH₂ powder: (A) Bright field micrograph; (B) dark field micrograph, imaged using a portion of the 110 α -MgH₂ ring pattern, showing several nano-scale α -MgH₂ grains; (C) Corresponding SAD.

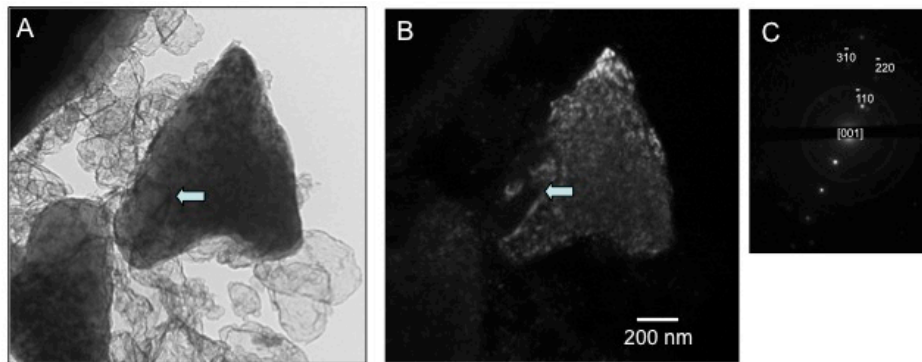


Figure 2-13- TEM micrographs of the milled and 16 hour annealed MgH₂ powder: (A) Bright field micrograph; (B) Dark field micrograph, imaged using $g = -110$. reflection, showing a large individual α grain with a coarse twin segment which appears dark (arrowed); (C) Corresponding SAD.

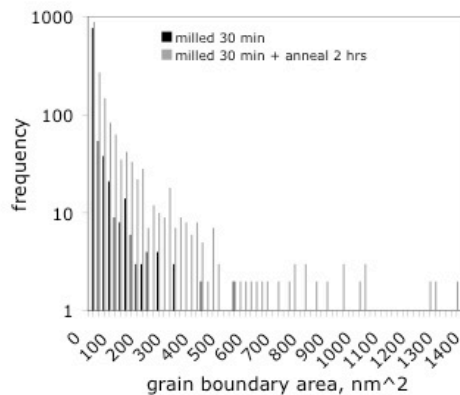


Figure 2-14- Histograms of the individual grain areas for the milled and the milled and 2 hour annealed powders, obtained from dark field micrographs.

2-4- Discussion

It is instructive to consider the ways in which milling may enhance hydrogen desorption. For desorption to occur, the hydrogen ions must diffuse to a surface where they must re-associate into molecules. Meanwhile, metallic magnesium must nucleate and grow in place of the hydride. Any of these three steps may be the rate limiting. Since this study was limited by the difficulty of characterizing the as-received powders in sufficient detail we are cautious not to provide a statement regarding which combination of the microstructural features are essential for enhanced desorption. However, what we do know is that the enhanced hydrogen desorption that is achieved through mechanical milling is almost completely lost through a high temperature hydrogen anneal.

Two factors that will have some influence on the onset of desorption are the presence of the thermodynamically unstable gamma phase and the break-up of surface oxide and hydroxide. The thermodynamically unstable γ -MgH₂ phase, present after milling, should transform to magnesium faster than the remaining α -MgH₂ [3]. However, this phase was only present in trace amounts and should not influence the entire DSC/TGA desorption curve. Researchers who detected this phase also observed a minor secondary low-temperature peak in the DSC data [3], which we did not. Though the powders had nearly identical air exposure prior to the DSC/TGA analysis, it is conceivable that the oxide/hydroxide re-grown on the freshly cleaved surfaces may not be as thick or as tenacious as the one formed on the as-received samples. It is also possible that the surface steps created by the passage of the dislocations during the milling cycle may act as preferential catalytic sites for hydrogen re-association: a step believed by some researchers to be the rate limiting phenomena for hydrogen desorption in MgH₂ (see reference [18] and the citations therein). However, the higher desorption temperature of the annealed powders implies that the native oxide alone cannot account for these differences.

Our experiments show that milling has a tremendous effect of changing the particle size, while the subsequent anneal coarsens the particles only incrementally. The drastic change in the particle size is quite expected since the as-received hydride particles are generally - though not entirely - brittle. A reduced particle size would tremendously increase the surface area available for hydrogen recombination. However, we see that in the annealed samples of similar surface area, the enhanced sorption is lost. This implies that increased surface area alone does not guarantee better kinetics.

Milling also provides a fairly modest change in the average grain size. In fact, the grain size reduction in the milled samples may not be as significant as the x-ray analysis indicates since the milled samples may have a higher density of deformation twins. Any changes in the grain size are likely to be due to repeated transgranular particle fracture during milling. While dynamic recrystallization is another known mechanism for grain size reduction during high-energy milling [19], it is unlikely to be responsible for the grain size reduction in the hydride. In an argon environment with essentially negligible partial pressure of hydrogen (glove box), thermodynamics would favor the nucleation of magnesium accompanied by the release of hydrogen, rather than the re-nucleation of the magnesium hydride.

The reduction of grain size would shorten the diffusion distance of hydrogen to the α -MgH₂ grain boundaries and increase the number of high diffusivity paths to the surface. Twin interfaces may have a similar effect in acting as fast diffusion paths. Similarly, dislocations introduced by milling may provide for additional pipe diffusion. However, since the annealed samples have a similar grain size to the milled ones, we can conclude that a sole increase in the grain boundary density is not enough to enhance desorption.

Another possible contribution to the lower MgH₂ desorption temperature in the milled state is the stored enthalpy given off due to the elimination of dislocations, a secondary effect being the elimination of twins. In heavily cold-worked materials dislocations are known to be a significant source of released energy [20]. It is instructive to consider the total contribution to the enthalpy from

the elimination of dislocations. The slip systems in α -MgH₂ have not been determined experimentally. However, we can reasonably assume that they are analogous to Rutile (TiO₂) [21] (the prototype for α). A possible Burgers vector \mathbf{b} is $\langle 001 \rangle$, which equals 0.302 nm for α -MgH₂. Other slip systems would yield Burgers vectors similar in magnitude. The x-ray microstrain ϵ may be related to dislocation density ρ and the grain size D by the following relation [22]:

$$\rho = \frac{2\sqrt{(3\epsilon)}}{D\mathbf{b}} \quad (2-2)$$

Using the values of 11 nm for D and 5.6×10^{-4} for ϵ yields a dislocation density of $1 \times 10^{15} / \text{m}^2$ and a dislocation spacing of 31 nm. Since a microstructure contains a distribution of grain sizes, a dislocation spacing of 31 nm implies that smaller grains contain either one or no dislocations.

The stored energy is the product of the energy of one dislocation and the dislocation density [20]. The energies of screw and edge dislocations are discussed in detail by Hirth and Lothe [23], and can be approximated by the following expression assuming an average population of edge and screw dislocations [20]:

$$E = \rho \left(\frac{(1-\nu/2)G\mathbf{b}^2}{4\pi(1-\nu)} \ln \left(\frac{R}{R_0} \right) \right) \quad (2-3)$$

R is the upper cutoff radius and may be taken as half the separation between dislocations [23]. The inner cutoff radius R_0 is taken as $4\mathbf{b}$. The shear modulus G and Poisson's ratio ν are calculated from the published elastic constants of α -MgH₂ [24], to be 25 GPa and 0.42 respectively. The final result, calculated for the given dislocation density, is an enthalpy of 236 J/mol, a value in agreement with previous reports on heavily cold-worked nanocrystalline materials, e.g. [25]. If this energy was on the same order of magnitude as the heat of hydride formation, one could argue that the release of cold-work adds a

significant driving force to the hydride => metal transformation. However, 236 J/mol is miniscule compared to the 75 kJ/mol heat of formation for α -MgH₂ [26], indicating a negligible thermodynamic contribution.

An alternative role for the dislocations introduced by the milling process is to act as heterogeneous nucleation sites for the magnesium phase. It is known that the transformation of α -MgH₂ to Mg proceeds through nucleation of many Mg crystallites in place of a single hydride grain [10]. There is a 15.7% volume decrease upon dehydrogenation and a corresponding tensile strain associated with precipitation of the metal. By nucleating on the positive edge component of the dislocation, some cancellation of the opposite sign stresses occurs and the magnesium metal nucleation barrier is reduced. A finer nano-scale grain size may also alter the thermodynamic stability of the hydride through the well-known Gibbs-Thomson effect. A similar argument could be made regarding nano-scale twins acting as heterogeneous nucleation sites and possessing a reduced thermodynamic stability.

2-5- Summary and Conclusions

We analyzed the microstructure of a high-energy mechanically milled magnesium hydride (α -MgH₂) powder. The powder was milled for 30 minutes in an argon environment, with half of the batch being subsequently annealed at 400 °C under pressurized hydrogen. The as-milled sample displays a hydrogen desorption temperature roughly 45 °C lower than the annealed powder. The sorption enhancement is reduced when the milled powders are annealed for 2 hours, and completely lost when the anneal lasted 16 hours.

For microstructural analysis, we focused on powder particle size and distribution, grain size and morphology, and defect density and type. The effect of milling was a tremendous reduction in the powder particle size, a creation of a multi-modal particle size distribution, and an introduction of significant microstrain into the hydride. The hydride grain size was also reduced by a factor

of two by the milling process. Post-milling anneals eliminated the microstrain, doubled the grain size and smoothed the particle size distribution.

Using a cryogenically-cooled liquid nitrogen sample holder we were able to successfully image the milled hydride microstructure using TEM. This has not been previously possible since at ambient temperatures the hydride is extremely unstable under the electron beam. We were able to image the individual hydride grains within the powder particles and compare grain boundary area distributions in the milled and the annealed powders. TEM analysis indicated that the as-milled microstructure contains nano-scale twins, which are reduced in density and coarsened by annealing.

An analysis of the energy associated with the stored strain indicates that the additional energy associated with the accumulated dislocations cannot significantly alter the thermodynamics of hydride dissociation. Rather, we believe that both the dislocations and the nano-scale twins influence the kinetics of the process.

2-6- References

- 1 Dornheim M, Eigen N, Barkhordarian G, Klassen T, Bormann R. Tailoring hydrogen storage materials towards application. *Advanced Engineering Materials* 2006; 8(5): 377-385.
- 2 Varin RA, Czujko T, Chiu C, Wronski Z. Particle size effects on the desorption properties of nanostructured magnesium dihydride (MgH₂) synthesized by controlled reactive mechanical milling (CRMM). *Journal of Alloys and Compounds* 2006; 424(1-2): 356-364.
- 3 Varin RA, Czujko T, Wronski Z. Particle size, grain size and gamma-MgH₂ effects on the desorption properties of nanocrystalline commercial magnesium hydride processed by controlled mechanical milling. *Nanotechnology* 2006; 17(15): 3856-3865.
- 4 Fatay D, Revesz A, Spassov T. Particle size and catalytic effect on the dehydrogenating of MgH₂. *Journal of Alloys and Compounds* 2005; 399(1-2): 237-241.
- 5 Hanada N, Ichikawa T, Orimo SI, Fujii H. Correlation between hydrogen storage properties and structural characteristics in mechanically milled magnesium hydride MgH₂. *Journal of Alloys and Compounds* 2004; 366(1-2): 269-273.
- 6 Friedrichs O, Sanchez-Lopez JC, Lopez-Cartes C, Dornheim M, Klassen T, Bormann R, Fernandez A. Chemical and microstructural study of the oxygen passivation behaviour of nanocrystalline Mg and MgH₂. *Applied Surface Science* 2006; 252(6): 2334-2345.
- 7 Porcu M, Petford-Long AK, Sykes JM. TEM studies of Nb₂O₅ catalyst in ball-milled MgH₂ for hydrogen storage. *Journal of Alloys and Compounds* 2008; 453(1-2): 341-346.
- 8 Bokhonov B, Ivanov E, Boldyrev V. A Study of the Electron-beam-induced Decomposition of Magnesium Hydride Single-crystals. *Materials Letters* 1987; 5(5-6): 218-221.
- 9 Herley PJ, Jones W. Transmission Electron Microscopy of Beam-sensitive Metal-Hydrides. *Zeitschrift für Physikalische Chemie Neue Folge* 1986; 147: 785-797.
- 10 Schober T. The Magnesium-Hydrogen System - Transmission Electron Microscopy. *Metallurgical Transactions A-Physical Metallurgy and Materials Science* 1981; 12(6): 951-957.

-
- 11 Warren BE. X-Ray Studies of Deformed Metals. *Progress in Metal Physics* 1959; 8: 147-202.
- 12 Klug HP, Alexander LE. *X-ray Diffraction Procedures*, John Wiley and Sons, New York, 1974, p. 643.
- 13 Vajeeston P, Ravindran P, Hauback BC, Fjellvag H, Kjekshus A, Furuseth S, Hanfland M. Structural stability and pressure-induced phase transitions in MgH₂. *Physical Review B* 2006; 73(22): 224102.
- 14 T. Klassen, Nanocrystalline light metal hydrides for hydrogen storage, in *Nanostructure Control of Materials* (Hannink RHJ, Hill AJ, Eds) 2006, Woodhead Publishing, pp. 266 – 302.
- 15 Bozhilov KN, Green II HW, Dobrzhinetskaya L. Clinoenstatite in Alpe Arami peridotite: Additional evidence of very high pressure. *Science* 1999; 284: 128-132.
- 16 Noe DC, Veblen DR. Mottled contrast in TEM images of mica crystals. *American Mineralogist* 1999; 84: 1932-1938.
- 17 Zaluska A, Zaluski L, Strom-Olsen JO. Synergy of Hydrogen Sorption in Ball-milled Hydrides of Mg and Mg₂Ni. *Journal of Alloys and Compounds* 1999; 289: 197-206.
- 18 Du AJ, Smith SC, Lu GQ. First-principle Studies of the Formation and Diffusion of Hydrogen Vacancies in Magnesium Hydride. *J. Phys. Chem. C*, 2007; 111: 8360-8365.
- 19 Zhang X, Wang H, Narayan J, Koch CC. Evidence for the Formation Mechanism of Nanoscale Microstructures in Cryomilled Zn Powder. *Acta Materialia* 2001; 49: 1319-1326.
- 20 Humphreys FJ, Hatherly M, *Recrystallization and Related Phenomena*, 2nd Edition, Elsevier, 2004, pp. 11- 60.
- 21 Hirthe WM, Adsit NR, Brittain JO. *Direct Observation of Imperfections in Crystals*. Newkirk JB (Ed), New York. 1962. pp. 135- 62.
- 22 Williamson GK, Smallman RE. Dislocation Densities in Some Annealed and Cold-worked Metals From Measurements on the X-ray Debye-Scherrer Spectrum. *Phil. Mag.* 1956; 1: 34.
- 23 Hirth JP, Lothe J. *Theory of Dislocations*, Second Edition, Krieger, Malabar Florida, 1982, pp. 59 – 95.

24 Zhang L, Wang Y, Cui T, Li Y, Li Y, He Z, Ma Y, Zou G. CaCl₂-type High-pressure Phase of Magnesium Hydride Predicted by Ab-initio Phonon Calculations. *Phys. Rev. B.* 2007; 75: 144109.

25 Zhang X, Wang H, Kassem M, Narayan J, Koch CC. Origins of Stored Enthalpy in Cryomilled Nanocrystalline Zn. *J. Mater. Res.* 2001; 16: 3485-3495.

26 Grochala W, Edwards PP. Thermal Decomposition of the Non-interstitial Hydrides for the Storage and Production of Hydrogen. *Chem. Rev.* 2004; 104: 1283-1315.

Chapter 3

Analysis of Deformation Twins and the Partially Dehydrogenated Microstructure in Nanocrystalline Magnesium Hydride (MgH₂) Powder

A version of this chapter has been published in: Danaie M, Tao SX, Kalisvaart P, Mitlin D. *Acta Materialia* 2010; 58(8): 3162-3172.

DOI: <http://dx.doi.org/10.1016/j.actamat.2010.01.055>

3-1- Introduction

Magnesium hydride (α -MgH₂) with its low cost and high gravimetric hydrogen capacity (7.6 wt.%) is a useful material for hydrogen storage applications in stationary fuel cells, where its high thermodynamic stability is less of an impediment. However, a key drawback is the hydride's sluggish hydrogenation/dehydrogenation kinetics, especially after prolonged sorption cycling. Numerous theoretical and experimental studies have been recently conducted to attempt at addressing this critical issue, e.g. [1, 2, 3, 4, 5, 6, 7]. Bloch and Mintz [8] provide a good summary of the early views on the rate limiting kinetics of the magnesium hydride. Several rate-limiting mechanisms have been

proposed: 1) the slowness of the Mg-MgH₂ phase boundary movement due to slow diffusivity of the hydrogen ions primarily through the hydride but also perhaps through the metal [9, 10, 11]; 2) the diffusion of hydrogen along a metal-hydride interface [12]; 3) surface passivation/poisoning due to adsorbed oxygen or sulfur-containing species [8]; 4) the high activation energy of hydrogen dissociation/re-association on MgH₂ surface [13].

The measured activation energy for desorption can be (and has been) attributed to any one of these mechanisms. For example, it is well known that the activation energy for hydrogen recombination on pure α (Rutile) MgH₂ is relatively high. The literature-quoted values include 144 kJ/mole and 172 kJ/mole (see reference [13] and the citations therein). Activation energy of 160 kJ/mole was also recently reported to correspond to hydrogen diffusion through the α -MgH₂ phase being the rate-limiting step in desorption [11]. Moreover recent modeling work also indicates that because of the interdependence of hydrogen diffusion and dissociation mechanisms a single rate limiting step may not exist at all [14].

High-energy ball milling of MgH₂ is known to significantly improve this hydride's desorption kinetics [15]. This effect has been attributed to various characteristics of the processed powder. Reduction in particle size below a threshold value [16, 17], reduction of particle and grain size [18] (while some researchers report an adverse effect of decrease in grain size [19]), the formation of a sub-stoichiometric hydride phase [20, 21], milling-induced formation of the metastable γ -MgH₂ [16], and introduction of dislocations [22] are among the proposed explanations for this phenomenon.

Even the actual mechanism of MgH₂ to Mg (and vice versa) phase transformation is poorly understood. A number of researchers have utilized the Johnson-Mehl-Avrami (J-M-A) isothermal kinetics framework for nucleation and growth (NG) phase transformation in order to gain insight regarding hydrogenation and dehydrogenation [9, 11, 23]. The results based on J-M-A methodology often provide multiple or even contradictory nucleation and growth scenarios. Some researchers also postulate that a diffusion-limited "shrinking-core" model would better simulate the hydrogen sorption transformations in Mg and in MgH₂ [e.g. 24].

Despite literally hundreds of published works on the subject, both the effect of high-energy milling and the mechanism of the MgH₂ → Mg phase transformation are not fully understood. This is largely due to paucity of direct and site-specific microstructural information regarding the hydride, which is very unstable under an electron beam at ambient conditions. Transmission electron microscopy (TEM) allows for direct analysis of highly deformed nanocrystalline materials, yielding site-specific information about phase distribution, defects and crystallography. At ambient temperature high-energy milled magnesium hydride is extremely unstable under the electron beam, almost instantly decomposing into a mixture of metallic Mg and MgO upon beam exposure [22]. This has discouraged researchers from using TEM for studying the hydride, instead concentrating the microscopy efforts on the metallic magnesium or on various secondary catalyst phases. Rather than TEM, the vast majority of microstructural characterization on magnesium hydride is achieved via indirect methods such as x-ray or neutron scattering techniques. These methods are invaluable in achieving an averaged global insight of the constituent phases and microstructure, but are less useful for tracking site-specific aspects of phase transformations.

The first goal of this study is to elucidate the effect of high-energy mechanical milling on the magnesium hydride microstructure by providing direct microstructural evidence. This will be accomplished by using transmission electron microscopy (TEM) to characterize the defects and Density Functional Theory (DFT) to model their effect. A cryogenic sample holder cooled to liquid nitrogen temperature (~90 K) will be utilized since it allows for TEM analysis of MgH₂ powder without rapid beam-induced decomposition [22] (Also see the Appendix I). The second goal of this study is to gain mechanistic insight regarding the MgH₂ to metallic magnesium phase transformation. Both conventional and energy-filtered TEM (EFTEM) will be employed to analyze partially desorbed magnesium hydride. The latter technique is uniquely suited for analyzing a mixed metal-hydride microstructure, since we are able to conclusively image the hydride and the metal phases without having to rely on overlapping electron diffraction patterns.

3-2- Experimental Procedures

Commercial magnesium hydride (MgH₂) powder was purchased from Gelest, Inc. with 97 wt.% purity, the rest being metallic magnesium. The powder was milled in a Fritsch Pulverisette 6 planetary ball-milling unit for 30 minutes at 650 rpm rotational speed. Agate balls and vials, with a ball to powder weight ratio of 10:1 were used for grinding. Milling was performed in a high purity and dry argon glove box (Unilab glove box manufactured by Braun, Inc.). The water vapor and oxygen content in the glove box was less than 0.1 ppm total. After milling some of the powder was subsequently annealed for 15 hours at 350°C under 30 bar (3 MPa) hydrogen pressure. High purity hydrogen gas (Hydrogen 6.0 research grade purchased from Welco-CGI gas technologies) was utilized for annealing. A portion of the annealed batch was subsequently milled again, using identical parameters as in the first round of milling. Thus a total of three types of samples were analyzed in this study: 1) MgH₂ milled for 30 min, labeled *Milled*; 2) MgH₂ milled for 30 min and hydrogen annealed for 15 hours, labeled *Milled-Annealed*; 3) the preceding sample milled again for 30 minutes, labeled *Milled-Annealed-Milled*. This study also refers the As-received MgH₂ powder as a comparative baseline. Additional analysis was performed on *Milled* hydride specimens that were partially desorbed to lose 3 wt.% hydrogen out of a total theoretical capacity of 7.6 wt.%. This was achieved in a Sievert's volumetric apparatus (HyEnergy™) at a temperature of 380°C.

Thermal desorption of powder samples was studied using a differential scanning calorimeter (DSC), SDT Q600, TA Instruments. All measurements were performed in standard alumina cups and under a constant flow of pure argon (200 mL/min) to prevent oxidation. In order to analyze the kinetics of desorption for different powder samples we performed Kissinger analysis [25]. Based on the theory of non-isothermal iso-conversion kinetics analysis the following relation holds for the activation energy (E) and pre-exponential term (k₀) for the rate constant $k=k_0\exp(-E/RT)$:

$$\ln \frac{\Phi}{T_{f'}^2} = \ln \frac{Rk_0}{E} - \frac{E}{RT_{f'}} - \ln \beta_{f'} \quad (3-1)$$

where Φ is the heating rate ($^{\circ}\text{C}/\text{min}$), $T_{f'}$ is the temperature corresponding to a specific degree of completion in the transformation (f') and b is a state variable. For Kissinger analysis the temperature of the maximal transformation rate ($T_{f_{\max}}$) is of interest and $\ln \beta_{f'}$ can be approximated to be zero. The activation energy is calculated from the slope of $\ln \frac{\Phi}{T_{f_{\max}}^2}$ versus $\frac{1}{T_{f_{\max}}}$. The experiments were conducted at four different heating rates (Φ : 5, 10, 15, and 20 $^{\circ}\text{C}/\text{min}$). Temperature and heat flow calibrations were carried out at each heating rate value prior to the corresponding experiment. The melting points of two standard samples were used for temperature calibration, zinc ($T_m = 419.5$ $^{\circ}\text{C}$) and indium ($T_m = 156.6$ $^{\circ}\text{C}$).

In order to see the effect of milling on the thermodynamics of reaction, enthalpy of desorption and absorption in two powder samples, *Milled* and *As-received*, was measured using a high-pressure DSC, Q20 TA Instruments. Heating rate of 1 $^{\circ}\text{C}/\text{min}$ was used, starting at four different initial hydrogen pressures. Enthalpy values for absorption were also measured by gathering DSC signal on cooling down following the desorption steps. Cooling rate of 5 $^{\circ}\text{C}/\text{min}$ was used for absorption steps. Van't Hoff plots for desorption and absorption were generated using the temperatures and pressures corresponding to the onset of corresponding reactions [26].

TEM analyses were performed on two microscopes, JEOL 2010 and JEOL 2200FS, the latter equipped with an in-column energy filter (Omega filter) and both operating at 200 kV accelerating voltage. TEM samples were prepared by dispersing the powder samples directly onto copper grid supported amorphous carbon films. This was done in our argon glove box, where the samples were stored until the microscopy sessions, reducing the samples exposure to air to the minimum possible. Conventional bright field - dark field imaging and selected area diffraction were done on the JEOL 2010 microscope using a cryogenic sample holder cooled down to 90 K. the cryo-holder was used so as to increase the stability time of the hydride phase under the electron beam. We were able to investigate the microstructure of MgH₂ specimens, with minimal indication of beam-induced desorption, for about 10-15 minutes. The commercial software Desktop Microscopist™ was used for simulating the experimental selected area

diffraction (SAD) patterns, using the well-known space group information for the metal and the hydride phases.

The JEOL 2200FS microscope, also equipped with a cryo-holder, was used for energy-filtered imaging (EFTEM) and electron energy loss spectroscopy (EELS) analysis. In order to characterize the features in the EELS spectra, electron beam-induced desorption of hydride powder was monitored at ambient temperature, *in-situ*. EELS spectra were acquired in image mode and with condenser lens highly defocused, to maintain a slow rate of desorption of the initially hydride sample. The full width at half maximum of the zero-loss peak was around the average of 0.9 eV. The spectrometer's dispersion was set at 300 $\mu\text{m}/\text{eV}$.

EFTEM experiments were carried out to locate hydride and metal phases, in the partially desorbed powder sample, by using their corresponding characteristic volume plasmon features. The slit width of 2 eV was used for selecting different parts of the EELS spectra. MgH₂ is known to have a plasmon peak around 14 eV (14.2 \pm 0.5 eV in [27]) while metallic Mg is known to demonstrate a plasmon peak at 10 eV (10.0 \pm 0.5 eV in [27]). Series of micrographs were acquired under energy shifts of 10 eV and 14 eV, to monitor the metal and hydride phases, respectively. In order to minimize the contribution of diffraction contrast, no objective apertures were used during EFTEM experiments.

3-3- Results

3-3-1- Deformation Twins: Experimental

Figure 3-1 illustrates the outcome of the Kissinger analysis for desorption activation energy. The calculated values are presented on the side of the graph. The *As-received* hydride powder had an activation energy for desorption equal to 196 kJ/mol. The calculated activation energy for desorption of the *Milled* powder sample is 127 kJ/mole. This is in good agreement with previously reported values for ball milled MgH₂ powder (for example E=120 kJ/mole in [28]). The *Milled-Annealed* sample exhibited a double peak in DSC heat flow signal. While various explanations have been proposed for the double DSC peak, the *Milled-Annealed* sample did not contain the high-pressure γ -MgH₂ phase that has been attributed to the lower temperature peak of the doublet [17].

The two peaks did not vary significantly in their activation energy values, with the lower temperature peak having $E = 141$ kJ/mol, and the higher temperature peak yielding $E = 151$ kJ/mol. The *Milled-Annealed-Milled* sample had the lowest activation energy for desorption, with $E = 100$ kJ/mol.

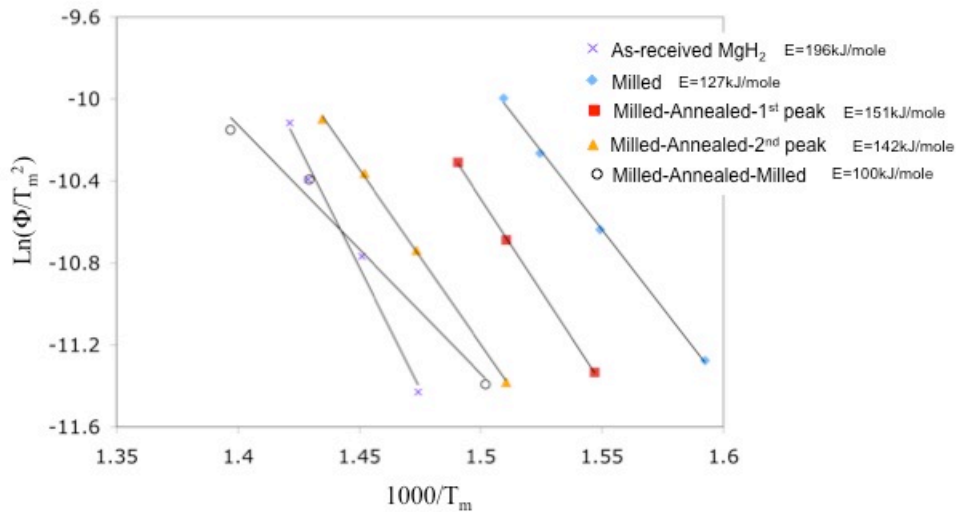


Figure 3-1- Kinetic analysis for the desorption of the three powder samples. Calculated values for activation energy (E) appear on the right. Activation energy for *as-received* powder is also presented for comparison.

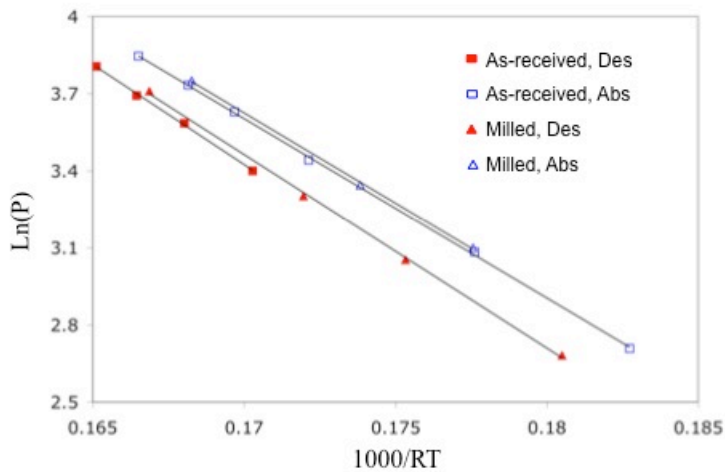


Figure 3-2- Van't Hoff plots generated using high pressure DSC, yielding the following enthalpy of reaction values: *As-received* desorption, $\Delta H = 78$ kJ/mole; *As-received* absorption, $\Delta H = -70$ kJ/mole; *Milled* desorption $\Delta H = 75$ kJ/mole; *Milled* absorption $\Delta H = -70$ kJ/mole (negative means exothermic).

We also investigated to see whether high-energy mechanical milling thermodynamically destabilizes α -MgH₂. Figure 3-2 shows the resulting Van't Hoff plots. There is a quantifiable hysteresis between the hydride formation plateau and the hydride decomposition plateau. In the *As-received* state the enthalpy for hydride formation is -70 kJ/mol while the enthalpy for hydride decomposition is 78 kJ/mol. In the *Milled* state the enthalpy for hydride formation is -70 kJ/mol while the enthalpy for hydride decomposition is 75 kJ/mol. This difference between absorption and desorption thermodynamics is associated with the asymmetry of the nucleation barrier for the hydride versus the metal and the irreversible work associated with each [29]. When the powders are milled the enthalpy for hydride decomposition is lowered by 3 kJ/mol. The enthalpy for hydride formation is unaffected since all the strain and defects introduced during the milling of the hydride are eliminated with the nucleation of the fresh metal, which is subsequently hydrogenated. A reduction of 3 kJ/mol in the enthalpy will have some affect on the desorption temperature. For example in a rough vacuum with a hydrogen partial pressure of 0.01 atm, a sample with $\Delta H = 78$ kJ/mol will begin to desorb at 190 °C, while a sample with $\Delta H = 75$ kJ/mol will begin to desorb at 173 °C.

TEM/EFTEM characterization was performed on the *Milled*, *Milled-Annealed*, and *Milled-Annealed-Milled* batches of the hydride powder samples. The as-received MgH₂ powder was not electron transparent. Figure 3-3 shows a representative microstructure of the *Milled* hydride sample. A prominent feature in the milled microstructure was large density of deformation twins. Figure 3-3A shows a multiply twinned grain in *Milled* powder sample, close to a symmetrical zone axis (ZA). Figure 3-3B shows the selected area diffraction (SAD) pattern obtained from this grain. The simulation of the diffraction pattern, shown in Figure 3-3C, demonstrates that the ZA is close to $[\bar{2}1\bar{2}]$ α -MgH₂. The twinning plane is (101) while the twinning translation is $\frac{1}{2}\langle 111 \rangle$. A schematic twin boundary structure is depicted in Fig. 3-3D. The mirror symmetry holds for the magnesium cations but not for the hydrogen anions. The twinning geometry agrees with the reported twinning mode in Rutile (TiO₂) [30], which has the same crystal structure as α -MgH₂, i.e. P4₂/mnm (136), and close value for c/a ratio (0.64 in Rutile versus 0.67 in α). The proposed twinning mode also agrees with cryo-TEM analysis of bulk MgH₂ [12], where $\{011\}$ -type twin boundaries were reported from trace

analysis. It is important to note that the proposed positions of the hydrogen in this schematic of the twin interface were obtained by assuming the same twinning displacement as for the Mg atoms. The actual hydrogen locations cannot be confirmed experimentally by TEM. In fact according to DFT analysis presented in the next section, the hydrogen atomic positions are slightly displaced relative to what is shown here.

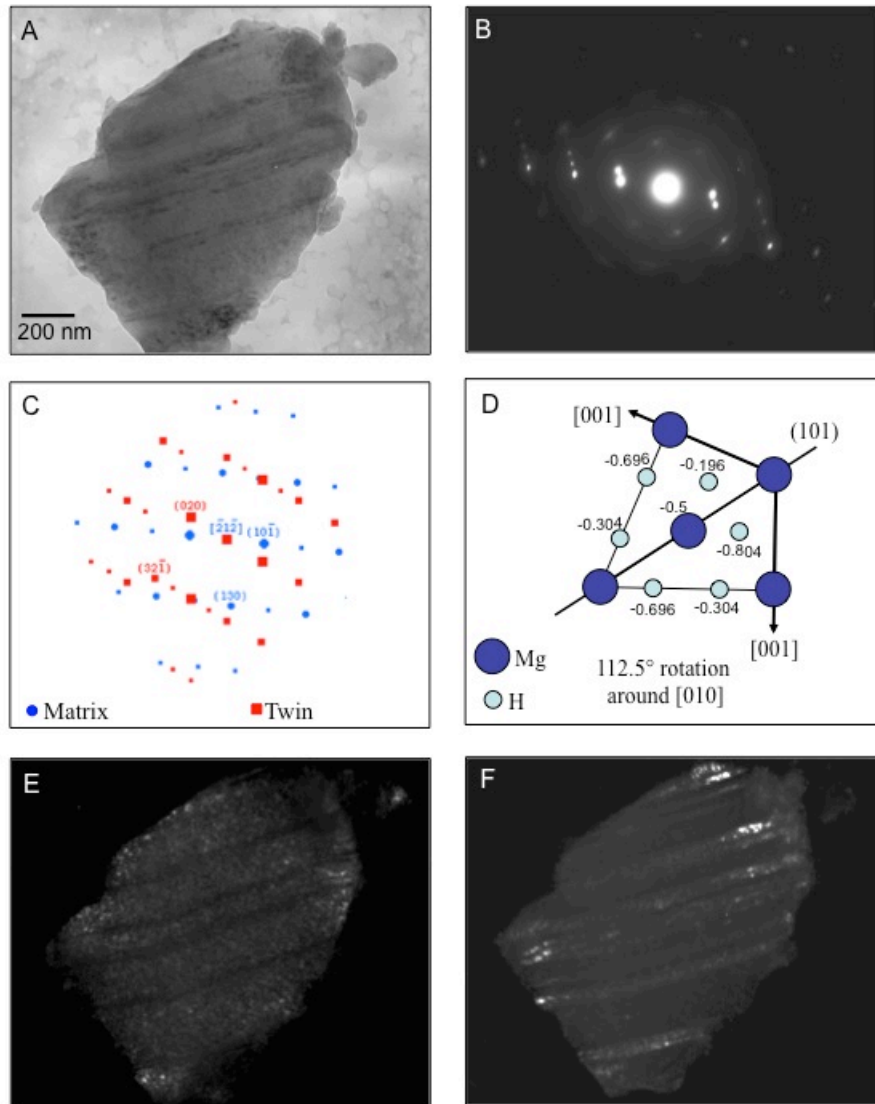


Figure 3-3- TEM analysis of a *Milled* powder particle: (A) Bright field micrograph; (B) Selected area diffraction SAD; (C) Simulation of the diffraction pattern which shows that the matrix ZA is close to $[-21-2]$, and the observed twinning plane is $(10\bar{1})$. (D) schematic of the twin geometry looking down $[010]$ (ion sizes not to scale); The numbers show the depth of the ions with reference to (010) plane; TEM analysis of a *Milled* powder particle: (E) dark field micrograph obtained using the matrix spot $g = -202$ α -MgH₂; (F) dark field micrograph obtained using $g = 020$ α -MgH₂ twin reflection.

Figure 3-3E shows a dark field micrograph obtained using the matrix spot $g = \bar{2}02$ α -MgH₂. Figure 3-3F shows a dark field micrograph obtained using $g = 020$ α -MgH₂ twin reflection. Figure 3-3 demonstrates that all the twins in the grain have the same orientation with respect to the matrix and are densely distributed throughout the hydride particle.

Figure 3-4 shows the representative grain morphology of the *Milled-Annealed* sample. Dark field images of two grains in Figure 3-4B were obtained using a 110 type α -MgH₂ reflection labeled in 3-4C. The thin faint continuous rings in the diffraction pattern correspond to MgO, which is always present on the hydride surfaces even at UHV conditions. Both grains imaged in dark-field show evidence of dislocation slip traces made in the surface oxide (most visible on top corner of leftmost grain). The dislocations were introduced by the high-energy milling, but were removed by the heat treatment. We have observed some remaining deformation twins after milder anneals than the one utilized in this study. In those cases the twins were always much coarser in scale and spacing than that in the initial as-deformed microstructure. The annealing performed here was purposely sufficiently aggressive such that we were sure that the twins would be eliminated. The conclusion that the annealed hydride did not contain any twins was reached after an exhaustive TEM examination of over 200 particles, taken from two different *Milled-Annealed* batches.

Figure 3-5 demonstrates the hydride microstructure when the powder is milled for another 30 minutes following the annealing cycle (*Milled-Annealed-Milled* sample). An arrow points to the same area in the bright field and the dark field micrographs where two twinned grains show strong diffraction contrast. We can now confidently state that in addition to increasing the dislocation density and refining the grain size, high-energy mechanical milling induces deformation twinning in α -MgH₂.

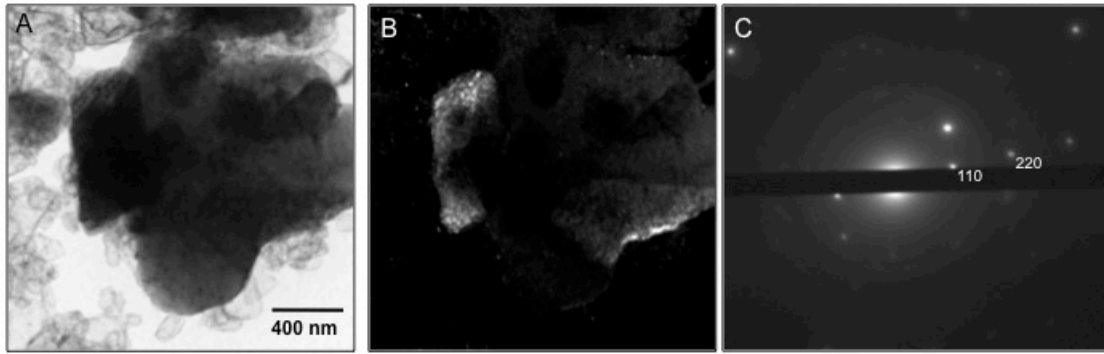


Figure 3-4- TEM micrographs of *Milled-Annealed* powder sample: (A) bright field micrograph, (B) dark field micrograph obtained using $g = 110$ α -MgH₂ reflection; (C) corresponding SAD pattern.

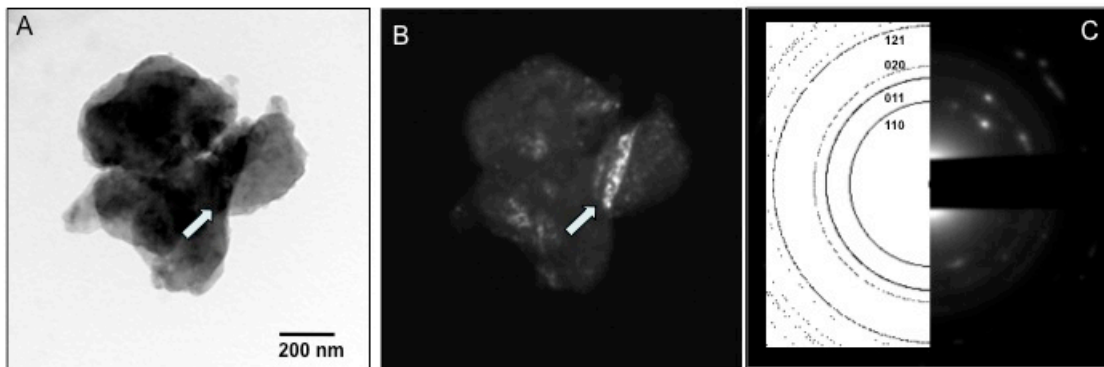


Figure 3-5- TEM micrographs of several *Milled-Annealed-Milled* powder particles: (A) bright field micrograph, (B) dark field micrograph obtained using a portion of the 110 α -MgH₂ ring pattern (C) diffraction pattern and simulation of α -MgH₂. Arrow points to the same area in the bright field and the dark field micrographs where two twinned grains show strong diffraction contrast.

3-3-2- Thermodynamic Stability of Deformation Twins: DFT

We performed Density Functional Theory (DFT) simulations to examine the thermodynamic stability of deformation twins in α -MgH₂. All calculations were performed using DFT as implemented in the Vienna Ab-Initio Simulation Package (VASP) [31, 32]. The Kohn-Sham equations were solved using a basis of Projector Augmented Wave-functions with a plane-wave energy cut-off 300 eV [33], and using pseudopotentials [34] to describe the core electrons. The Perdew-Wang 1991 generalized gradient approximation was used for the electron-exchange correlation potential [35]. A total of 13x13x13 k points were used to model the Brillouin zone for the four metal unit

cell structures. With this number of k points, the influence of the distribution of the k points on the calculated total energies became less than 0.02% and therefore this number of k points was deemed sufficiently large. For larger cells k points were scaled down proportionally, e.g. for a lattice parameter of double length, only half number of k points were required. Therefore for eight and sixteen metal cells (see Figure 3-6B and C, z axes were doubled and quadrupled), 13x13x7 and 13x13x3 k points were used. For all structures the lattice parameters, the volume and the atom positions were allowed to relax. The formation energies are defined as, $\Delta H_f = E_{MgH_2} - E_{Mg(hcp)} - E_{H_2}$ where E_{MgH_2} , $E_{Mg(hcp)}$ and E_{H_2} are energies obtained from their respective calculations, normalized to the number of metal atoms present in the unit cell. At H/M=2, as is the case in our study, this is the same as normalization per H₂ molecule.

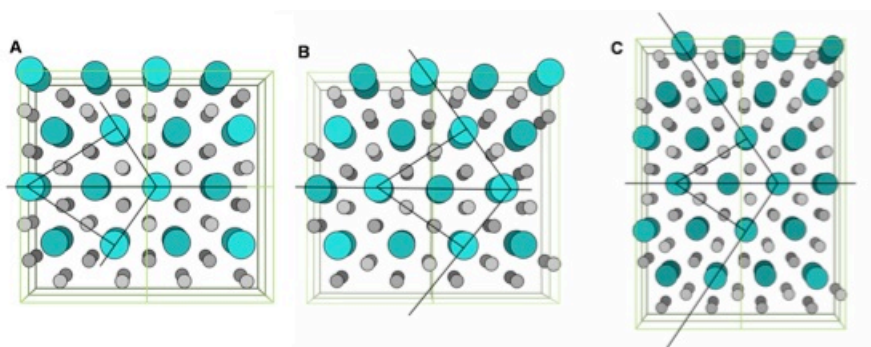


Figure 3-6- Multiple deformation twins. In order to highlight the twin structures (the black lines), supercells are shown. (A) Four metal atoms cell with 100% deformation twins (2x2x2 supercell); (B) Eight metal atoms cell with 50% deformation twins (2x2x1 supercell); (C) Twelve metal atoms with 33% deformation twins (2x2x1 supercell).

The optimized Rutile MgH₂ (i.e. α -MgH₂) structural data are shown in Table 3-1. Figure 3-7A presents the optimized twin structure in α -MgH₂. Notice the slight variation in hydrogen atoms positions from what we anticipated, by only considering the geometry of shear, in Figure 3-3D. Figure 3-7B marks some of the atomic positions, referred to in Table 3-1. In α -MgH₂ the hydrogen ions are arranged approximately octahedrally around the magnesium ions, which in turn are arranged trigonally around the hydrogen ions. The calculated formation energy of Rutile MgH₂ is -77 kJ/mol (with ZPE correction), which is well within the range reported in literature, e.g. [29]. Three cells (Figure 3-6A, B and

(C) are considered to model different density of multiple deformation twins, i.e. (A), (B), and (C) are with 100%, 50%, 33% of deformation twins in the cells. The calculated formation energy for all of three cells is the same as for α -MgH₂ (77 kJ/mol). Therefore even an unrealistically high density of deformation twins does not thermodynamically destabilize the hydride.

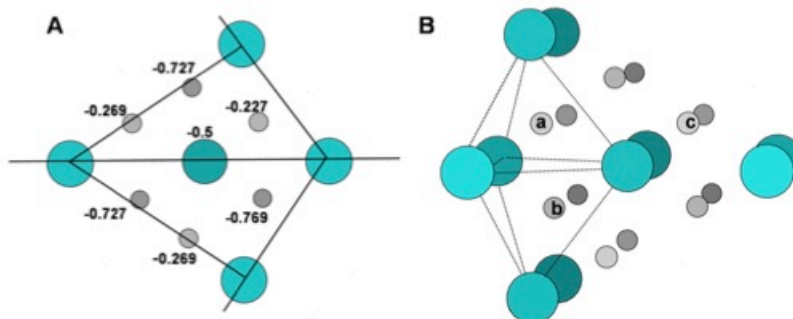


Figure 3-7- (A) The optimized structure of twinned α -MgH₂. (B) A side view of the twin interface.

Table 3-1- The crystal data for Rutile MgH₂ and deformation twin MgH₂. The calculated lattice constants and interatomic distances. Unit is Å.

		Rutile	Twin
Lattice constants		a=4.45, c=2.99	a=5.37, b=4.90, c=4.44
Interatomic distances	Mg-H	1.94, 1.94, 1.92	1.98, 1.93, 1.90
	H-H	2.72 (ac)	2.63(ab)
		2.46 (ab) 3.22 (be)	2.69(ac)

3-3-3- Partially Desorbed Microstructure: Experimental

Figure 3-8A shows the Electron Energy Loss Spectra (EELS) of the hydride phase and its time-resolved evolution during *in-situ* room temperature desorption in the TEM. The α -MgH₂ volume plasmon peak is around 14.7 eV. Desorption starts to occur after a short time. This is accompanied by the appearance of the volume plasmon peak corresponding to metallic Mg that is around 10.7 eV. Metallic magnesium having a

higher density of “free” electrons, as compared to the ionic MgH₂, exhibits a plasmon peak with smaller full-width at half maximum. With increasing the exposure time the 14.7 eV peak diminishes and the 10.7 eV peak grows in intensity. After 574 seconds of beam exposure the particle is devoid of any hydride phase (red plot in Fig. 3-8A). The peak around 21 eV is due to plural plasmon scattering in resulting magnesium phase. The broad peak around 22-26 eV can be attributed to plural scattering in MgH₂ (~28 eV), potential MgO phase (~23 eV [36]), or carbon volume plasmon (20-34 eV [37]) from the support thin film.

The temporal evolution in the microstructure can be further traced by constructing EFTEM micrographs of the plasmon peaks. Micrographs presented in Figure 3-8B show the stages of beam-induced desorption of a hydride particle by using the Mg plasmon and the α -MgH₂ plasmon energy shifts. Initially the bulk of the particle is fully MgH₂. There is some evidence of metal Mg formation near the particle surface. After about 400 seconds of electron beam exposure, the majority of the particle has transformed into Mg, with some hydride left near the particle center. While it may be argued that this is strong evidence of the “core-shell” morphology that has been proposed for both desorption and absorption in MgH₂ [24], as we will show it is not representative of the *ex-situ* elevated temperature dehydrogenation sequence.

The EFTEM results of partially desorbed *Milled* sample are presented in Figures 3-9 through 3-12. In all cases the bright field micrograph is labeled (A) while the 10 eV (Mg plasmon peak) and the 14 eV (MgH₂ plasmon peak) energy filtered micrographs are labeled (B) and (C), respectively. Figure 3-9 depicts a large partially desorbed hydride particle along with several smaller satellite hydride particles. In this partially dehydrogenated state (roughly 40% of the hydride, by weight, is transformed to magnesium) there is little evidence for a shell of magnesium that is growing at the expense of a shrinking hydride core.

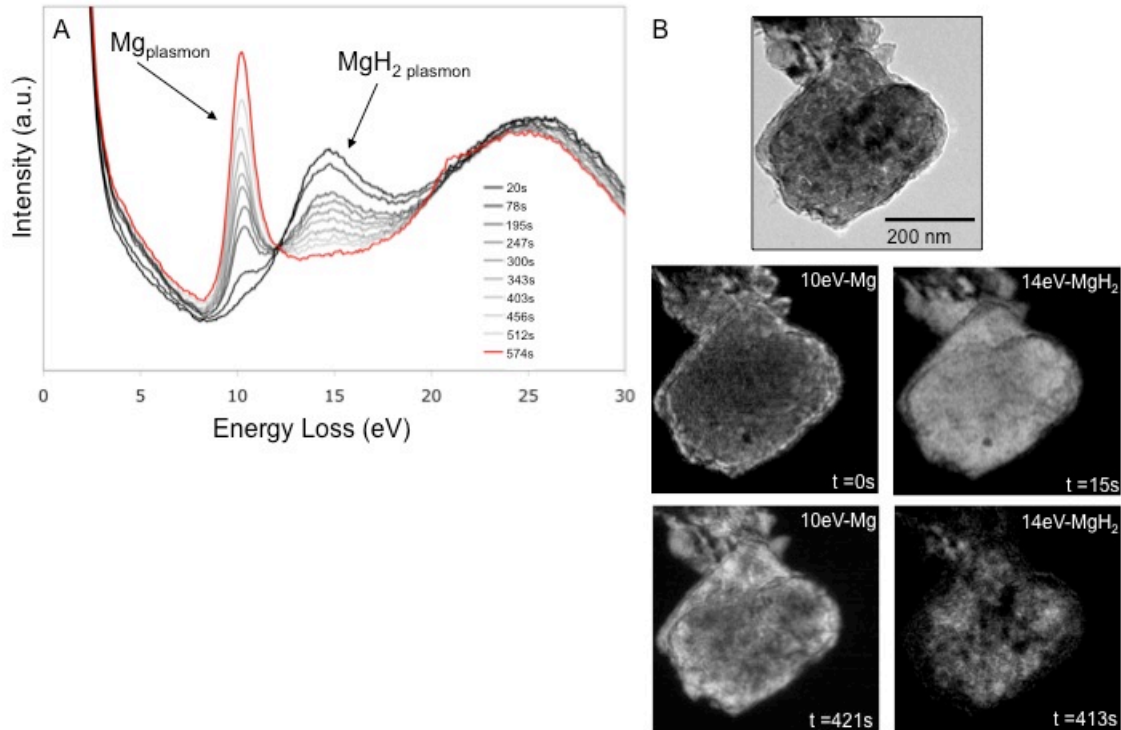


Figure 3-8- (A) Time-resolved series of low-energy loss spectra from *in-situ* desorption of Milled sample; (B) An example of room-temperature *in-situ* desorption as observed by EFTEM. Initial state bright field micrograph is shown in top-center. Left column shows Mg at $t \approx 0$ seconds beam exposure and after 421 seconds. Right column shows MgH₂ after 15 and 413 second exposures.

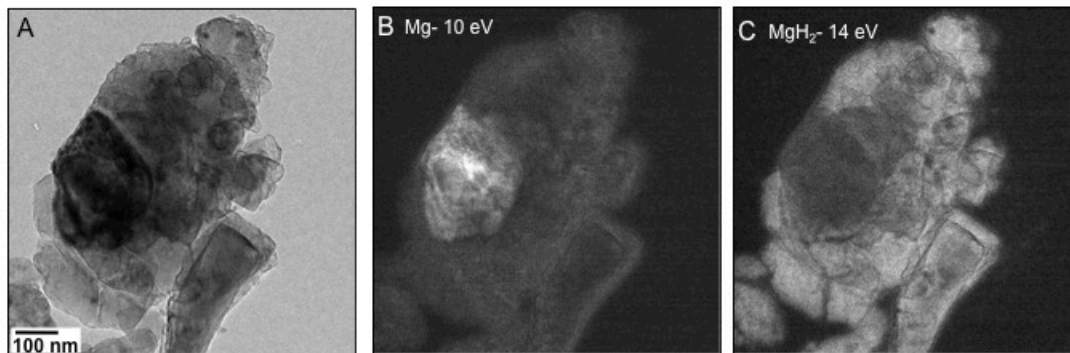


Figure 3-9- Partially desorbed relatively large hydride particle in the *Milled* condition. (A) bright field micrograph; (B) Mg - 10eV and (C) MgH₂ - 14eV energy-filtered micrographs.

Instead there is an isolated metallic magnesium grain that has formed on the surface of the large hydride particle. The magnesium grain shows some residual diffraction contrast, which is unavoidable in the absence of a rocking electron beam feature on the microscope [38].

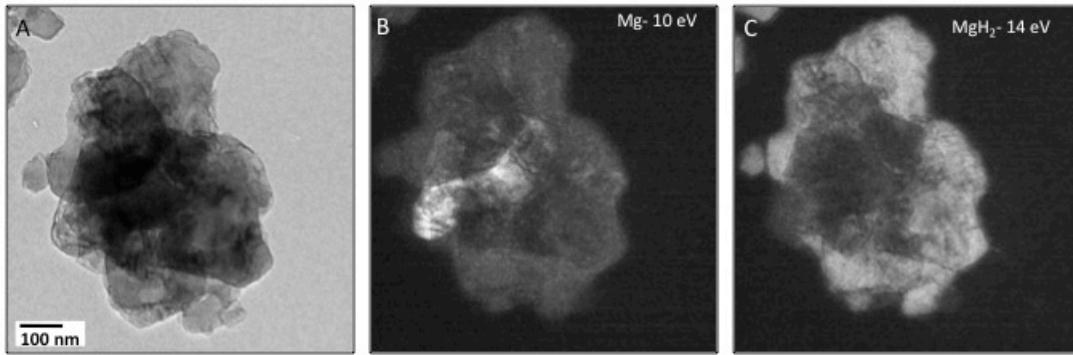


Figure 3-10- Another example of a partially desorbed relatively large hydride particle in the *Milled* condition. (A) bright field micrograph; (B) Mg - 10eV and (C) MgH₂ - 14eV energy-filtered micrographs.

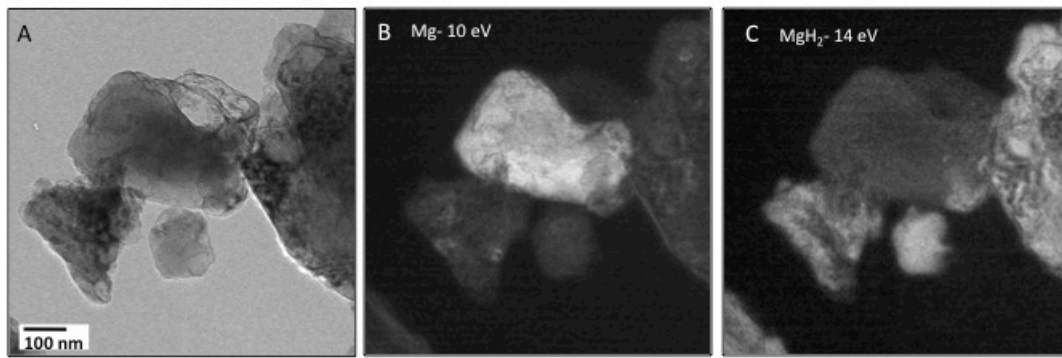


Figure 3-11- Several smaller metal and hydride particles taken from a partially desorbed *Milled* condition sample. (A) bright field micrograph; (B) Mg - 10eV and (C) MgH₂ - 14eV energy-filtered micrographs.

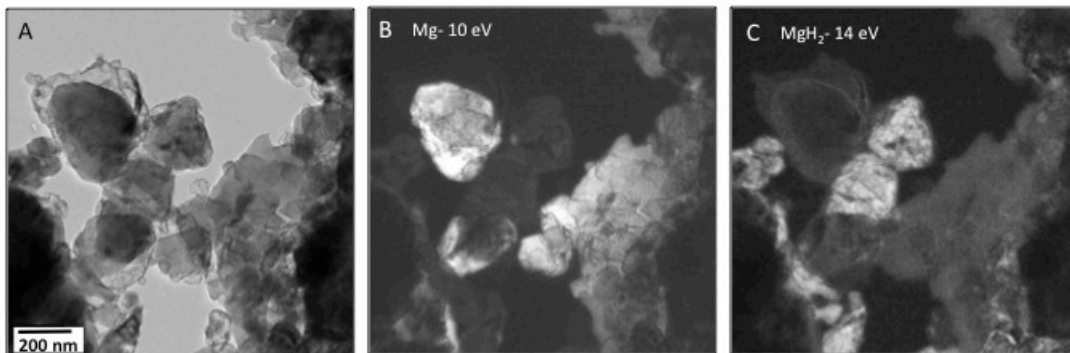


Figure 3-12- Another example of smaller metal and hydride particles taken from a partially desorbed *Milled* condition sample. (A) bright field micrograph; (B) Mg - 10eV and (C) MgH₂ - 14eV energy-filtered micrographs.

Figure 3-10 confirms this mechanistic picture: one or several metallic magnesium grains having heterogeneously nucleated on the surface of a large hydride particle. Meanwhile a large portion of the particle including other regions near its surface, remain a hydride. Figures 3-11 and 3-12 show the other scenario encountered in the partially desorbed

specimens: Smaller particles that are either fully transformed to metal or remain fully hydrided. There again is not evidence for a “core-shell” structure.

3-4-Discussion

3-4-1- Effect of Twins on the Thermodynamics and Kinetics of Desorption

Our TEM analysis indicates that high-energy mechanical milling induces a high density of deformation twins in magnesium hydride powder. This is not surprising since the two basic prerequisites for deformation twinning [39] are present in this system: First a non-close-packed (tetragonal) ionic crystal structure with less than 5 independent slip systems that cannot readily deform by shear. And second a high-strain-rate mode of deformation inherent to planetary milling process. The critical question to address here is the significance of the deformation twins with respect to desorption properties of the hydride powder.

As we showed in Figure 3-1 the effect of milling is most pronouncedly observed in lowering desorption activation energy. However high-pressure DSC experiments (Figure 3-2) demonstrated that milling does cause a fairly minor thermodynamic destabilization. This agrees with the PCT measurements reported by Huot *et al.* [40]. Previously we have shown that the dislocation density in a high-energy milled MgH₂ powder is at the upper limit of highly deformed materials [22] (Chapter 2 of this thesis). From XRD broadening we calculated the density to be $1 \times 10^{15} / \text{m}^2$ and a dislocation spacing of 31 nm. However this resulted in an energy release of only 236 J/mol due to their annealing - a negligible thermodynamic destabilization. Based on the DFT analysis performed here we can now safely argue that deformation twins will make a similarly negligible contribution to the lowering of the enthalpy of hydride decomposition. Most likely the 3 kJ/mol destabilization comes from a mechanism proposed by Berube and co-workers [1], consisting of high-energy milling inducing localized regions in the hydride with excess volume.

Our hypothesis is that a significant portion of this enhancement is in fact attributable to the high diffusivity of the hydrogen ions along the twin boundaries. This

hypothesis agrees well with a recently published NMR study on MgH₂-based powder systems [41]. In this study the authors demonstrated that hydrogen hopping rate (ω_H) in ball milled MgH₂ powder is drastically higher than that in commercial, coarse-grained MgH₂, even below 225° C. It is also shown that ω_H is far less temperature-dependent in milled powder and more closely related to the sample history i.e. the microstructure. We agree with the ultimate conclusion in Ref [41], stating that the effect of milling on enhancing desorption kinetics is not simply due to reduction in the diffusion distances. But rather it has to do with higher hydrogen mobility in ball-milled microstructure.

3-4-2- Partially Desorbed Microstructure

We used EFTEM to examine a partially desorbed (*ex-situ*, elevated-temperature) Milled hydride sample and compared the results with *in-situ* desorption under an electron beam at ambient temperature. The main conclusion to be drawn from comparing *in-situ* versus *ex-situ* results is that the former is not representative of the latter. Hence *in-situ* TEM desorption studies cannot be utilized to understand the true mechanisms of elevated temperature dehydrogenation.

If metal nucleation were energetically easy one would observe many magnesium nucleation sites and growth fronts per hydride particle. In the extreme case, when nucleation is energetically easy but subsequent growth of the metal is diffusion limited, one would observe a continuous growing shell of magnesium surrounding a shrinking core of hydride, i.e. a “core-shell”. However the *ex-situ* results demonstrate the difficulty of nucleating during desorption. Isolated grains of magnesium formed on a large hydride particle signal heterogeneous nucleation with a large energetic barrier. The small hydride particles that are either fully transformed or non-transformed also imply heterogeneous nucleation. From these results we can rule out “growing metal shell and shrinking hydride core” model for dehydrogenation of MgH₂.

It is known that the strain energy associated with a solid-state phase transformation impedes the progression of the reaction. In case of a ductile matrix, plastic deformation can dissipate some of this elastic energy. This happens in the case of hydride precipitation in metals (see for example [42] for Nb-H system and [43] for Zr-H system),

where a network of dislocations is nucleated around the hydride precipitate. These dislocations can also potentially later act as preferential sites for heterogeneous nucleation. The phase transformation from MgH₂ to metallic Mg is accompanied by a significant reduction in volume (24.6%), generating large strain energy in the process. It is unlikely that α -MgH₂ would easily yield during bulk nucleation of magnesium. This is especially true for the powders that are already heavily deformed by milling. Hence heterogeneous nucleation on exposed surfaces is the preferred mechanism.

Many factors may lead to some particles desorbing preferentially. One such factor is the crystallographic orientation of the grains relative to the surface and hence to the nucleating magnesium crystallite. Schober has shown that during nucleation and growth Mg and MgH₂ maintain the following orientation relation [12]: (100)MgH₂ || (0001)Mg and [001]MgH₂ || [-1-120]Mg. Surface nucleation on magnesium should begin where the (100) and (010) faces of MgH₂ are exposed to the surface. The grain-to-grain variation in the density of deformation-induced defects and their orientation relative to the surface may also be a factor. Another factor may be particle-to-particle variations in the structure or intactness of the nano-scale MgO layer that always covers the MgH₂ [44]. Unintended minority catalytic phases may also play a role such as residual magnesium oxide particles that are inherited from the as-received powder. It has been shown that direct milling of MgH₂ with MgO powder can yield improved desorption kinetics [45]. Even a minute volume fraction of oxide ground to nano-scale dimensions and dispersed throughout the microstructure may give a significant catalytic boost to the hydride particles that are contacted. Again, any of these factors would become important only when uniform and dense nucleation of magnesium is difficult.

Finally we would like to point out that the two key findings of this study - deformation twins and magnesium nucleation - provide for a fairly consistent phenomenology of MgH₂ → Mg phase transformation. The behavior is analogous to what is observed during solid-state precipitation in bulk metallic alloys. Nucleation of a chemically and crystallographically dissimilar phase with a different density than the parent matrix is difficult, proceeding heterogeneously on surfaces and on high-energy defects such as high-angle grain boundaries. In bulk alloys there are relatively more grain boundaries than free surfaces. In the hydride powder the situation is reversed since many

smaller particles are single crystal. In cases when the geometric spacing of such defects is relatively coarse, so will be the spacing of the nuclei. The critical process that allows for the rapid completion of this thermodynamically favorable but kinetically limited reaction is solid-state diffusion. A sufficient flux of atoms or ions towards or away from the growing nucleus is essential. The observed twins may promote fast hydrogen transport away from the growing magnesium front, allowing the heterogeneously nucleated magnesium grains to fully consume MgH₂ at a faster rate. This is a secondary and complementary pathway for eliminating hydrogen from the matrix in addition to its interstitial diffusion through the growing metal and along the interphase-interface.

3-5- Summary and Conclusions

In the present study we used TEM to examine the microstructure of high-energy planetary ball milled as well as of partially desorbed MgH₂ powder. The focus was on understanding the nature of crystallographic defects induced by high-energy ball milling and the mechanism of dehydrogenation. TEM analysis demonstrates that milling MgH₂ powder causes deformation twinning in the hydride. An annealing heat treatment under pressurized hydrogen eliminates the twins, while a subsequent milling cycle induces their presence again. The observed mode was (011)-type twin planes with the twinning directions being $1/2\langle 111 \rangle$.

High-energy mechanical milling results in a minor (3 kJ/mol) thermodynamic destabilization of α -MgH₂. Since DFT predicts that deformation twins do not affect the thermodynamic stability of α -MgH₂, other explanations for this slight destabilization must be sought. Milling does cause a pronounced decrease in the activation energy for hydrogen desorption. Our hypothesis is that a significant contributor to the milling-induced kinetic enhancement is due to this higher diffusivity of the hydrogen ions through the twin boundaries.

We conducted EFTEM studies on partially desorbed milled hydride sample to investigate the nature of the MgH₂ → Mg phase transformation. We also compared these results to *in-situ* TEM desorption experiments. The primary conclusion of this comparison is that the *in-situ* TEM desorption sequence is not representative of the bulk

elevated-temperature *ex-situ* dehydrogenation mechanism. The *ex-situ* results show aspects of the desorbed microstructure previously unreported: Metallic magnesium crystallites heterogeneously nucleate on the large hydride particles. The number of nuclei per particle is few and no evidence exists for a continuous growing shell of metal around the shrinking hydride core. The smaller particles are either fully transformed to magnesium or remain entirely a hydride. Several scenarios are proposed for this observation including the particle-to-particle variations in the crystallography of the individual grains relative to the particle surface, differences in the structure of the surface oxide, variations in defect content, or the proximity of residual magnesium oxide phase.

3-6- References

- 1 Berube V, Chen G, Dreeselhaus MS. Impact of Nanostructuring on the Enthalpy of Formation of Metal Hydrides. *Int. J. Hydrogen Energy* 2008; 33: 4122.
- 2 Denys RV, Riabov AB, Maehlen, Lototsky MV, Solberg JK, Yartys VA. *In-situ* Synchrotron X-ray Diffraction Studies of Hydrogen Desorption and Absorption Properties of Mg and Mg-Mm-Ni after Reactive Ball Milling in Hydrogen. *Acta Mater.* 2009; 57: 3989.
- 3 Ma LP, Kang XD, Dai HB, Liang Y, Fang ZZ, Wang PJ, Wang P, Cheng HM. Superior Catalytic Effect of TiF₃ over TiCl₃ in Improving the Hydrogen Sorption Kinetics of MgH₂: Catalytic Role of Fluorine Anion. *Acta Mater.* 2009; 57: 2250.
- 4 Cermak J, Kral L. Hydrogen Diffusion in Mg-H and Mg-Ni-H Alloys. *Acta Mater.* 2008; 56: 2677.
- 5 Zlotea C, Sahlberg M, Zbilien S, Moretto P, Andersson Y. Hydrogen Desorption Studies of the Mg₂₄Y₅-H System: Formation of Mg Tubes, Kinetics and Cycling Effects. *Acta Mater.* 2008; 56: 2421.
- 6 Pauw BR, Kalisvaart WP, Tao SX, Koper MTM, Jansen APJ, Notten PHL. Cubic MgH₂ Stabilized by Alloying with Transition Metals: A Density Functional Theory Study. *Acta Mater.* 2008; 56: 2948-2954.
- 7 Li HW, Kikuchi K, Nakamori Y, Ohba N, Miwa K, Towata S, Orimo S. Dehydriding and Rehydriding Processes of Well-crystallized Mg(BH₄)₂ Accompanying with Formation of Intermediate Compounds. *Acta Mater.* 2008; 56: 1342.
- 8 Bloch J, Mintz MH. Kinetics and Mechanisms of Metal Hydrides Formation - A Review. *J. Alloy. Compds.* 1997; 253-254: 529.
- 9 Rudman PS. Hydrogen-diffusion-rate-limited Hydriding and Dehydriding Kinetics. *J. Appl. Phys.* 1979; 50(11): 7195.
- 10 Barkhordarian G, Klassen T, Bormann R. Kinetic Investigation of the Effect of Milling Time on the Hydrogen Sorption Reaction of Magnesium Catalyzed with Different Nb₂O₅ Contents. *J. Alloy. Compds.* 2006; 407: 249.
- 11 Fernandez JF, Sanchez CR. Rate Determining Step in the Absorption and Desorption of Hydrogen by Magnesium. *J. Alloy. Compds.* 2002; 340: 189.
- 12 Schober T. The Magnesium-Hydrogen System - Transmission Electron Microscopy. *Met. Trans. A* 1981; 12A: 951.

-
- 13 Du AJ, Smith SC, Lu GQ. First-principle Studies of the Formation and Diffusion of Hydrogen Vacancies in Magnesium Hydride. *J. Phys. Chem. C* 2007; 111:8360.
- 14 Borgschulte A, Gremaud R, Griessen R. Interplay of Diffusion and Dissociation Mechanisms During Hydrogen Absorption in Metals. *Phys. Rev. B* 2008; 78: 094106.
- 15 Dornheim M, Eigen N, Barkhordarian G, Klassen T, Bormann R. Tailoring Hydrogen Storage Materials Towards Application. *Adv. Eng. Mat.* 2006; 8(5): 377-385.
- 16 Varin RA, Czujko T, Chiu C, Wronski Z. Particle Size Effects on the Desorption Properties of Nanostructured Magnesium Dihydride (MgH₂) Synthesized by Controlled Reactive Mechanical Milling (CRMM). *J. Alloy. Compds.* 2006; 424: 356.
- 17 Varin RA, Czujko T, Wronski Z. Particle Size, Grain Size and Gamma-MgH₂ Effects on the Desorption Properties of Nanocrystalline Commercial Magnesium Hydride Processed by Controlled Mechanical Milling. *Nanotechnology* 2006; 17: 3856.
- 18 Fatay D, Revesz A, Spassov D. Particle Size and Catalytic Effect on the Dehydrating of MgH₂. *J. Alloy. Compds.* 2005; 399: 237.
- 19 Hanada N, Ichikawa T, Orimo S-I, Fujii H. Correlation Between Hydrogen Storage Properties and Structural Characteristics in Mechanically Milled Magnesium Hydride MgH₂. *J. Alloy. Compds.* 2004; 366: 269.
- 20 Borgschulte A, Bosenberg U, Barkhordarian G, Dornheim M, Bormann R. Enhanced Hydrogen Sorption Kinetics of Magnesium by Destabilized MgH₂-delta. *Catalysis Today* 2007; 120: 262.
- 21 Schimmel HG, Huot J, Chapon LC, Tichelaar FD, Mulder FM. Hydrogen Cycling of Niobium and Vanadium Catalyzed Nanostructured Magnesium. *J. Amer. Chem. Soc.* 2005; 127: 14348.
- 22 Danaie M, Mitlin D. TEM Analysis and Sorption Properties of High-energy Milled MgH₂ Powders. *J. Alloy. Compds.* 2009; 476: 590.
- 23 Wu C, Wang P, Yao X, Liu C, Chen D, Lu GQ, Cheng H. Effects of SWNT and Metallic Catalyst on Hydrogen Absorption/desorption Performance of MgH₂. *J. Phys. Chem. B.* 2005; 109: 22217.
- 24 Zhdanov VP, Krozer A, Kasemo B. Kinetics of 1st-Order Phase-Transitions Initiated by Diffusion of Particles from the Surface into the Bulk. *Phys. Rev. B.* 1993; 47: 11044.
- 25 Kissinger HE. Reaction Kinetics in Differential Thermal Analysis. *Analytical Chemistry* 1957; 29(11): 1702.

-
- 26 Rongeat C, Llamas-Jansa I, Doppiu S, Deledda S, Borgschulte A, Schultz L, Gutfleisch O. Determination of the Heat of Hydride Formation/Decomposition by High-pressure Differential Scanning Calorimetry (HP-DSC). *J. Phys. Chem. B* 2007; 111: 13301.
- 27 Zaluzec NJ, Schober T, Westlake DG. Application of EELS to the Study of Metal-Hydrogen Systems. 39th Annual EMSA meeting, 1981: 194.
- 28 Luo Y, Wang P, Ma L-P, Cheng H-M. Hydrogen Sorption Kinetics of MgH₂ Catalyzed with NbF₅. *J. Alloy. Compds.* 2008; 453: 138.
- 29 Flanagan TB and Oats WA. 1978. in: *Hydrogen in Intermetallic Compounds I (Topics in Applied Physics)*, Schlapbach L (Ed), Springer-Verlag, Berlin, p. 49-85.
- 30 Lee W-Y, Bristowe PD, Gao Y, Merkle KL. The Atomic-structure of Twin Boundaries in Rutile. *Phil. Mag. Lett.* 1993; 68(5): 309.
- 31 Kresse G and Furthmüller J. Efficient Iterative Schemes for Ab-initio Total-energy Calculations Using a Plane-wave Basis Set. *Phys. Rev. B* 1996; 54: 11169.
- 32 Kresse G and Furthmüller J. Efficiency of Ab-initio Total Energy Calculations for Metals and Semiconductors Using a Plane-wave Basis Set. *Comp. Mat. Sci.* 1996; 6:15.
- 33 Kresse G and Joubert G. From Ultrasoft Pseudopotentials to the Projector Augmented-wave Method. *Phys. Rev. B* 1999; 59: 1758.
- 34 Perdew JP. Generalized Gradient Approximations for Exchange and Correlation - A Look Backward and Forward. *Physica B* 1991; 172: 1.
- 35 Monkhorst HJ and Pack JD. Special Points for Brillouin-zone Integrations. *Phys. Rev. B* 1976; 13: 5188.
- 36 From EELS Atlas provided in, *Transmission electron energy loss spectroscopy in materials science and the EELS atlas*, Ahn CC(Ed.), Wiley-VCH, 2nd Edition, 2005.
- 37 Stolojan V. 2003, Electron energy loss spectra of a-C (in STEM and TEM), in: *Properties of Amorphous Carbon*, Silva SRP (Ed.), Institution of Engineering and Technology, p. 83.
- 38 Hofer F, Warbichler P. Improved Imaging of Secondary Phases in Solids by Energy-filtering TEM. *Ultramicroscopy* 1996; 63: 21-25.
- 39 Christian JW, Mahajan S. Deformation Twinning. *Prog. Mat. Sci.* 1995; 39: 1.

40 Huot J, Liang G, Boily S, Van Neste A, Schulz R. Structural Study and Hydrogen Sorption Kinetics of Ball-milled Magnesium Hydride. *J. Alloy. Compds.* 1999; 293-295: 495.

41 Corey RL, Ivancic TM, Shane DT, Carl EA, Bowman RC, Bellosta von Colbe JM, Dornheim M, Bormann R, Huot J, Zidan R, Stowe AC, Conradi MS. Hydrogen Motion in Magnesium Hydride by NMR. *J. Phys. Chem. C* 2008; 112: 19784.

42 Makenas BJ, Birnbaum HK. Phase-changes in the Niobium-Hydrogen System .1. Accommodation Effects During Hydride Precipitation. *Acta Metall.* 1980; 28: 979.

43 Carpenter GJC. Precipitation of Gamma-Zirconium Hydride in Zirconium. *Acta Metall.* 1978; 26: 1225.

44 Borgschulte A, Biemann M, Zuttel A, Barkhordarian G, Dornheim M, Bormann R. Hydrogen Dissociation on Oxide Covered MgH₂ by Catalytically Active Vacancies. *Appl. Surf. Sci.* 2008; 254: 2377.

45 Aguey-Zinsou K-F, Ares Fernandez JR, Klassen T, Bormann R. Using MgO to Improve the (De)hydriding Properties of Magnesium. *Mater. Res. Bull.* 2006; 41(6): 1118.

Chapter 4

Hydrogen Storage in Bulk Mg-Ti and Mg-Stainless Steel Multilayer Composites Synthesized via Accumulative Roll-Bonding (ARB)

A version of this chapter has been submitted to *International Journal of Hydrogen Energy* (List of authors: Danaie M, Mauer C, Mitlin D, Huot J, Date submitted: 24 August 2010), Manuscript reference No.: HE-D-10-02104

4-1- Introduction

Magnesium hydride has long been considered a potential candidate for solid-state hydrogen storage, due to its relative high hydrogen capacity (7.6 wt.%) and abundance. Aside from the excessive thermodynamic stability of this hydride ($\Delta H_f = -77$ kJ/mole), the main obstacle has proven to be its slow hydrogen desorption and absorption kinetics. Numerous theoretical and experimental studies have been recently conducted to attempt at addressing this critical issue, e.g. [1, 2, 3, 4, 5, 6]. This sluggish kinetics has been attributed to numerous factors, e.g. high activation energy for hydrogen dissociation and recombination on MgH₂ surface [7], low diffusivity of hydrogen through the hydride phase [8], and slow mobility of the hydride/metal inter-phase interface during the phase

transformation [9]. The focus of many studies has been to incorporate a suitable catalyst via different methods into the magnesium matrix in order to enhance the reaction kinetics.

The majority of the experimental studies in this field have used high-energy ball milling to add the catalyst material to the magnesium powder. Even though this approach has been invaluable in identifying viable catalyst systems, its prospects for scale-up to an industrial level seem highly difficult and expensive (See [10] and references therein). Due to exposure of large surface area of the storage media in this powder-based technique the milling process has to be performed under controlled atmosphere, which can be very challenging on an industrial scale. Also moving from a batch-scale process to a continuous procedure is difficult to implement for ball milling. It would be more convenient to take advantage of a technology, which is already widespread in the industry, with existing sub-structure and know-how.

It is with the above-mentioned rationale that few groups have approached cold rolling as an alternative route for manufacturing hydrogen storage composite systems. Accumulative roll bonding (ARB) is a method for preparing ultra-fine grain structures in metals and alloys [11]. This technique involves repetitive cold rolling and folding of a single-phase metal [12] or an alloy in order to reach a refined grain structure. The same methodology was later put to use for preparing bimetallic composites, mainly for structural applications [13]. Repetitive cold-rolling and folding has recently been demonstrated to be also pertinent for various hydrogen storage related applications, including catalyst addition (Mg-2.5 at.% Pd [14]), formation of intermetallics (Mg₆Pd [15, 16, 17], Mg₂Cu [16], Mg₁₇Al₁₂ [18], Mg₂Ni [19, 20]) and also preparation of alloy systems (Ti-Cr [21], Ti-V-Mn [22]). It has also been demonstrated that Mg₂Ni prepared via repetitive rolling can operate as the negative electrode for Ni-MH batteries [23].

As-synthesized alloys and composites for hydrogen storage applications generally show much slower hydrogen sorption kinetics during the initial hydrogenation cycle, as compared to the subsequent cycles. This is certainly true for the magnesium-based systems. The term “activation step” has come to describe this initial induction period, highlighting the fact that the kinetics is not acceptable for actual functional utilization of the material. Research done on understanding the mechanisms involved in this activation

step is relatively sparse. As for non-catalyzed activation of pure magnesium, it has been suggested that the thermally induced rupture of the surface oxide layer, which occurs at around 400°C, is conducive to activation [24]. Also there are indications of the significance of texture on the kinetics of activation, with a preferred orientation close to [0002] showing a faster activation [25].

The goal of the present study is to further explore the possibility of synthesizing bulk magnesium-based hydrogen storage materials with acceptable kinetics. To achieve this we use repetitive cold rolling to fabricate magnesium - titanium and magnesium - stainless steel multilayer composites. Our aim is to utilize a synthesis approach that could translate into industrial production with minimal additional modification. In essence what this means is that all the material handling is to be performed in ambient conditions, without any inert atmosphere. In parallel, we seek to use bulk multilayers as a model system to provide phenomenological insight into the origin of activation. We expect that the fundamental scientific findings of this study would be fully transferable to more established “classic” hydrogen storage materials synthesis routes such as high-energy ball milling.

4-2- Experimental Procedures

Commercially pure magnesium ribbons were cold-rolled and folded for different number of repetitions with pure titanium. The magnesium starting material was ribbons about 0.15 mm thick and 3 mm wide, with +99% purity (purchased from Aldrich). The titanium used was in the form of foils 0.0127 mm in thickness and 99.8% in purity (from Alfa Aesar). The Ti foil and Mg ribbon were cut in proportions to yield the desired composition. After cleaning all surfaces with acetone, the Ti foil was wrapped around Mg ribbon and placed between two clean stainless steel plates (~1mm in thickness) and passed through the rolling machine. For rolling we used a Durston DRM 100 with rolls of 6.5 centimeters in diameter and 13.0 centimeters in length. For all cases the rolling speed of 20 revolutions per minute was used. After the first rolling pass, the sample was folded in half, placed between the steel plates and rolled again. This was repeated by gradually reducing the rolling gap. After reaching a homogeneous-looking, single piece sample the

roll spacing was kept constant. Hence the thickness of the sample would be reduced to about its half on each fold and rolling cycle (designated here as: 1 FR). The final thickness of each of the samples was around 0.7 mm. Care was taken to maintain clean working surfaces during sample preparation. All sample handling and preparation was performed at ambient conditions.

We also prepared fold-and-rolled samples of magnesium with 316L stainless steel (SS) with the same general preparation procedure. The only difference, however, was that the SS samples were in the form of elongated flakes, which were 7 mm in length and about 0.2 mm in thickness.

For Mg/Ti samples, we first varied the composition – refer to table 1- keeping the number of folding and rolling (FR = 15) and gap distances in rolling constant. Secondly, for the composition Mg- 22 at.% Ti (relative volume fraction of 82.3 Vol.% Mg) we varied the numbers of FR and used four sets of FR conditions: 15, 30, 50 and 90. For Mg-SS samples we only utilized the first approach, while keeping the number of FR operations constant at 15. Table 4-1 summarizes the volume fraction of each phase for the experiments. Since 316L stainless steel is a multi-component alloy, we will refer to its volume fraction rather than the more intuitive atomic percent, as is done for the Mg-Ti multilayers.

Table 4-1- Labeling and respective volume fractions of the 15 FR titanium and stainless steel samples.

Sample name	Volume % Mg	Volume % Ti/SS
Mg- 40 at.%Ti	66.4	33.6
Mg- 22 at.%Ti	82.3	17.7
Mg- 10at.%Ti	92.2	7.8
Mg- 5 at.%Ti	96.1	3.9
Mg- 18 vol.%SS	82	18
Mg- 8 vol.%SS	92	8
Mg- 5 vol.%SS	95	5
Mg- 1 vol.%SS	99	1

The hydrogen sorption properties of the samples were tested in a Sieverts' type apparatus. All hydrogen sorption and desorption tests were carried out at 350°C, with the absorption hydrogen pressure set at 2 MPa and the desorption pressure around 0.05 MPa. The amount of sample used for these measurements was typically around 150 mg.

A Bruker D8-Focus Diffractometer, with Cu K α radiation ($\lambda = 1.5406 \text{ \AA}$), was utilized for phase identification, grain size and dislocation density analysis. We performed a modified Williamson-Hall analysis, taking into account the strain anisotropy through assigning various contrast factors to different dislocation groups [26, 27]. We used the software package *MWP-fit* developed by Ribarik et al. [28, 29] for this analysis. Transmission electron microscopy (TEM) analysis was performed using a JEOL-2010 TEM equipped with a LaB₆ filament and operated at 200 kV. Samples were mechanically thinned to about 100 μm and then jet polished in a Fischione twin jet electropolisher (Model 110) at room temperature. 15% (by volume) solution of perchloric acid in ethanol was used for electropolishing.

We performed scanning electron microscopy (SEM) on the polished cross sections of the prepared composites. In all cases back-scattered electron (BSE) signal was used, yielding a compositional (Z) contrast in the final images. In number of occasions we performed SEM on samples partially absorbed and quenched during their activation step or after a number of cycles. Since the hydride is very reactive with water, these samples were polished using an oil-based coolant liquid (Buehler's Metadi) and diamond paste. This prevented the decomposition of the hydride in the process of surface preparation. Scanning electron microscopy was performed on a Hitachi S-3000N microscope, equipped with a back-scattered electron detector. For all cases the microscope was operated at 15 kV accelerating voltage.

4-3- Results

4-3-1- Mg-Ti 15FR, Effect of Ti Content

Cross-sectional microstructures of the 15FR Mg-Ti composites with four different Ti loadings can be found in Figure 4-1. Since we are using back-scattered electron (BSE)

signal for imaging, the titanium shows a brighter contrast compared to the lower atomic number magnesium matrix. The red arrows on these micrographs mark the trace of the rolling plane. One can observe that Ti flakes generally follow the rolling direction in these micrographs. At the two higher Ti content samples (*i.e.* 22 and 40 atomic percent) we can discern a layered structure in the Ti phase. This is due to overlap of the Ti foil onto itself when wrapped around the Mg ribbon before the start of rolling (more likely to happen for samples with higher Ti content, as can be seen in micrographs 4-1(C) and 4-1(D)). The observed thickness of the layers is close to that of the initial Ti foil.

By applying the multiple whole profile (MWP) fitting analysis to the XRD data of the Mg-Ti samples we can track the average grain size and dislocation density in the magnesium matrix (Figure 4-2). In graphs presented in Figures 4-2A and 4-2C the data for a pure magnesium sample (with no Ti addition), undergone the same fold and roll process is also presented for comparison. Increasing the Ti content, while keeping the number of FR constant (15 here) in these composites has no substantial impact on the average grain size of magnesium (Figure 4-2A), with the volume-weighted average grain size being in the 80 nm range. Figure 4-2B shows a bright field TEM micrograph of a typical region within the magnesium microstructure in the Mg-10 at.%Ti composite. The hole in the top right corner of the sample also contains some MgO left over from the electrochemical jet polishing process. Unfortunately the secondary Ti phase acted as coarse inclusions during the electrochemical polishing, making it exceedingly difficult to obtain sufficiently thin samples for quantitative defect analysis. What Figure 4-2B does confirm, however, is the presence of very fine Mg grains. Much larger Mg grains, on the order of 500 nm - 1000 nm, were also occasionally detected within the microstructure. Since the diffraction peaks present for Ti were limited in number, the fit qualities for the Ti grain size values were fairly poor.

As for the dislocation density in magnesium (Figure 4-2C), we observe an increasing trend in dislocation population with increasing the Ti content. The dislocation density reaches a saturation limit for Mg-22 at.%Ti, and drops off for Mg-40 at.%Ti. Pure magnesium deformed at low temperatures can undergo partial recovery even at room temperature [30, 31]. In order for the recovery process to proceed there needs to be a minimum stored energy to derive the reaction [32].

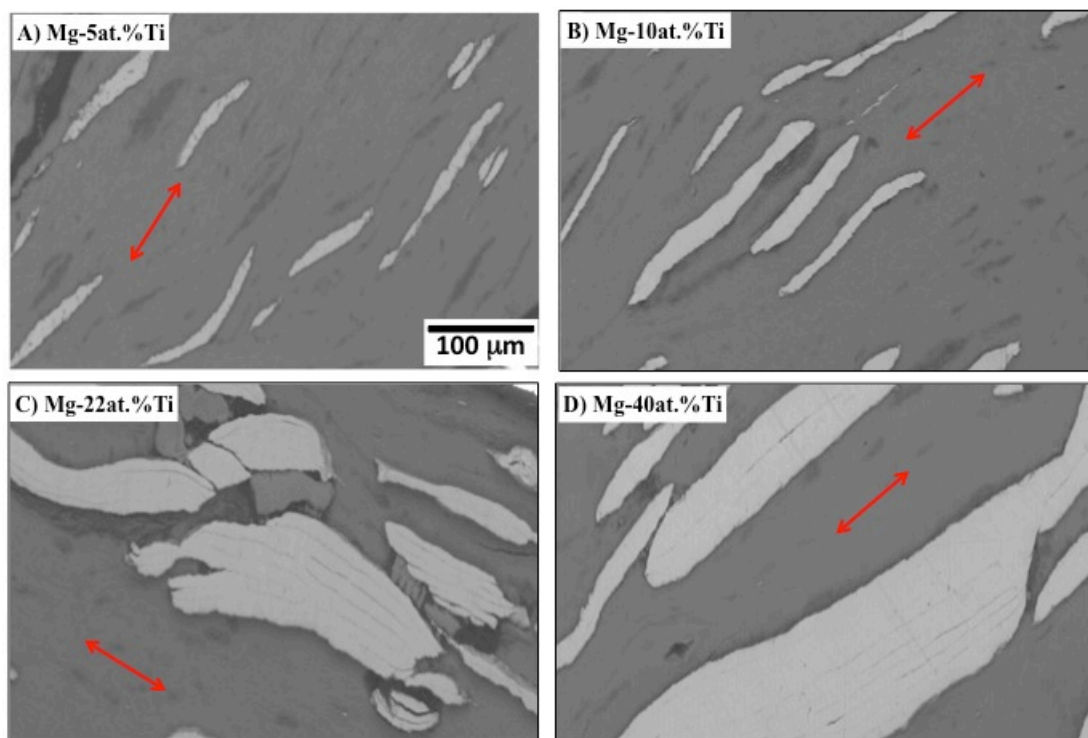


Figure 4-1- SEM micrographs showing the as-rolled microstructure of the Mg-Ti samples with different compositions, all folded and rolled for 15 times. The arrow shows the approximate trace of the rolling plane. The images are at the same magnification.

This condition seems to be met at 22 at.% Ti addition and 15 passes of folding and rolling. On the other hand Ti, with higher melting point, requires higher temperatures for recovery and stores a larger density of dislocations. Figure 4-2D shows the dislocation density in Ti phase. In the Mg-5 at.%Ti composite, the Ti XRD peaks were too close to the background to perform a meaningful analysis. The dislocation density values in Ti are consistently an order of magnitude larger than those in magnesium matrix. In both cases the reported values for dislocation density is the sum of all three types of dislocations in the hexagonal crystal system, i.e. Burgers vector types a $\langle 2-1-10 \rangle$, type c $\langle 0001 \rangle$ and type a+c $\langle -2113 \rangle$.

The hydrogen sorption kinetics of 15FR Mg-Ti composites, with varying Ti content is presented in Figure 4-3. Identically rolled pure magnesium is not shown since it displayed negligible hydrogen absorption at the testing conditions. Figure 4-3A indicates that during the initial hydrogen absorption (i.e. activation), increasing Ti content yields improved kinetics. This result seems to hold up to 22at.%Ti, with no subsequent improvement at 40 at.%Ti. On the first desorption cycle (Figure 4-3B) the 22 at.%Ti

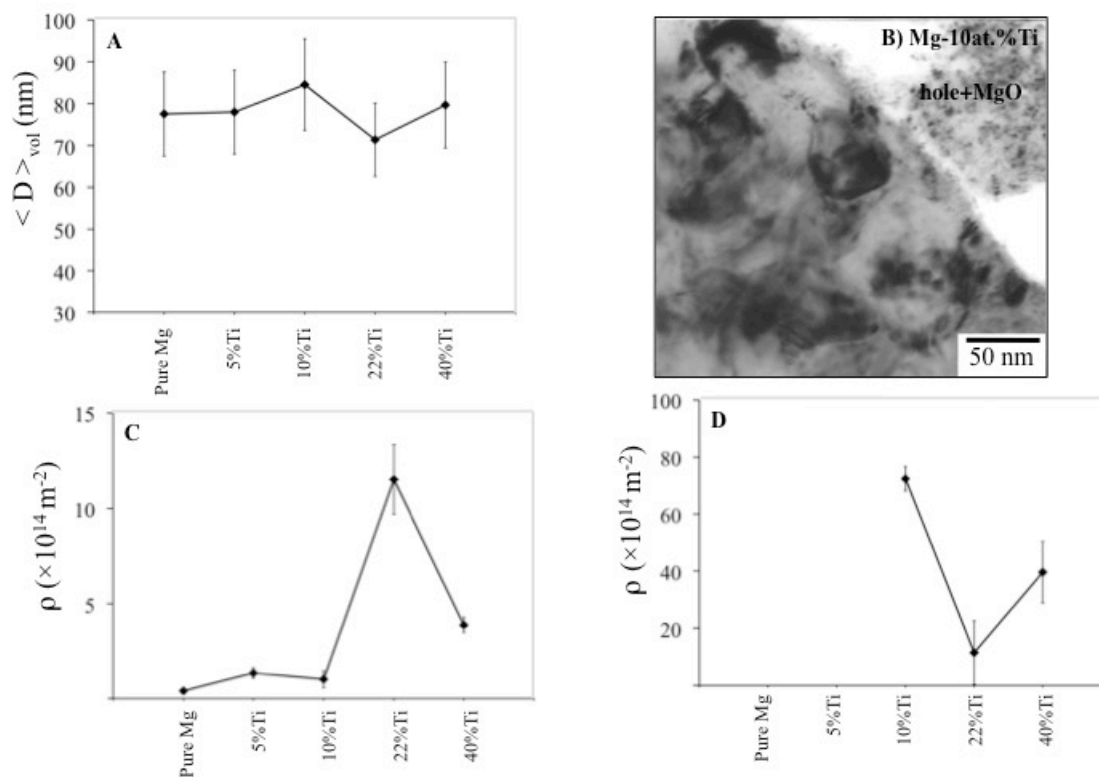


Figure 4-2- Mg-Ti composites with 15FR repetitions but with different Ti content. (A) XRD obtained (via multiple whole profile fitting) average grain size of Mg as a function of Ti content. (B) Bright field TEM micrograph of a representative region in the Mg portion of a Mg-10at.%Ti composite. (C) XRD obtained dislocation density in Mg, and (D) dislocation density in Ti.

sample demonstrates the fastest kinetics. The desorbed capacity is lower than the absorbed capacity. As will be confirmed by the XRD results, this is due to the irreversible formation of TiH_2 , which cannot be desorbed at these testing conditions.

Figure 4-3C and 4-3D show the composites' performance during the subsequent absorption and desorption cycles, respectively. The pure Mg-5 at.%Ti data is not shown since this composite displayed very slow second cycle absorption kinetics, yielding almost no hydrogen absorption after 4 hours. At capacities less than approximately 1 wt.% hydrogen, the absorption rates of all three composites are quite similar. However the maximum experimentally achievable capacity of the composites decreases with increasing Ti content. The Mg-10 at.%Ti demonstrate the highest hydrogen gravimetric capacity, followed by Mg-22 at.%Ti and finally Mg-40 at.%Ti. During second desorption, the same held true: The Mg-10 at.%Ti composite was able to desorb the most

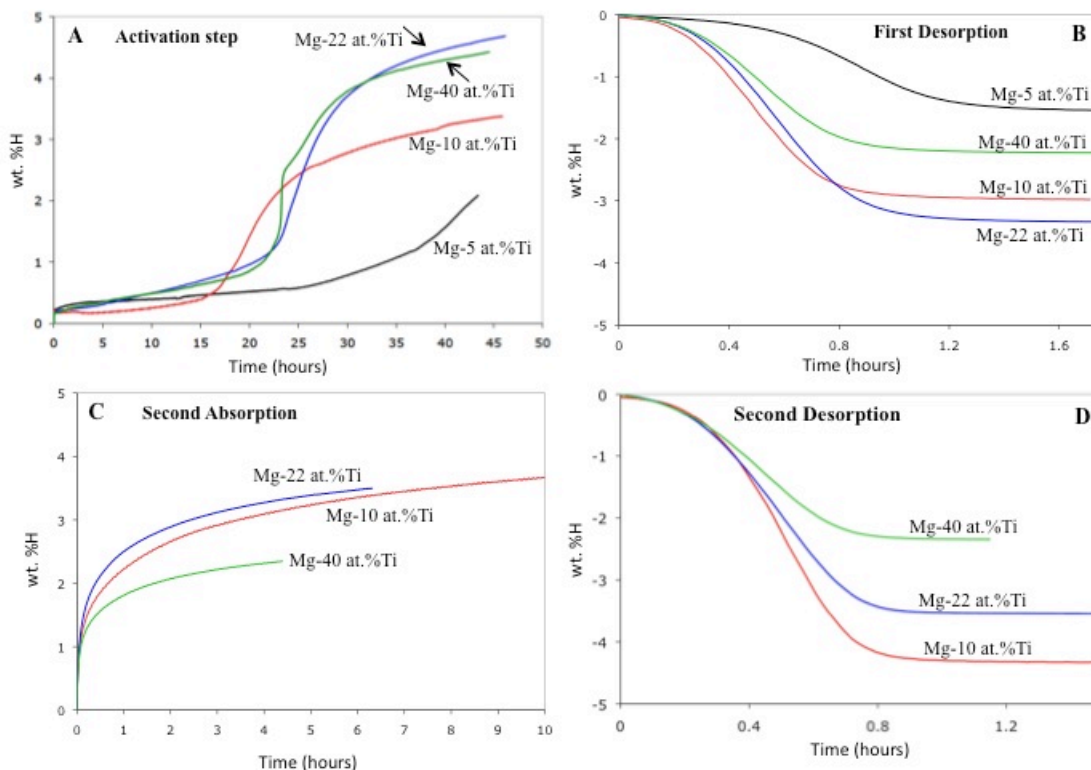


Figure 4-3- Hydrogen sorption kinetics of 15FR Mg-Ti composites with varying Ti content, tested at 350°C: (A) First absorption (activation), (B) First desorption, (C) and (D) Second absorption and desorption, respectively.

hydrogen, followed by 22 at.% Ti and 40 at.% Ti samples. As it is evident from a comparison of Figure 3B and Figure 4-3D, the Mg-10 at.% Ti sample was not fully activated by the initial absorption cycle. The sluggish kinetics led to a lower capacity during cycle 1 compared to cycle 2.

A summary of the effect of Ti content on the sorption kinetics is provided in Table 4-2, which compares the maximum possible reversible capacity due to hydrogenation of magnesium and the experimentally measured ones at absorption cycle 2. When Ti content is low, hydrogen absorption by magnesium is very sluggish. This leads to a kinetically limited capacity that is far less than the theoretical value. As Ti content increases, so does the absorption kinetics, allowing most of the magnesium to absorb hydrogen. However, if the Ti addition is excessively high, complete hydrogenation of magnesium is again hindered.

The complete pressure-composition isotherm curve for Mg-22 at.%Ti sample is presented in Figure 4-4A. At 350°C, the equilibrium hydrogen pressure is around 0.6

MPa, which is close to that value for pure magnesium hydride [1]. Moreover the maximum observed hydrogen capacity is around 4 wt.%, confirming that after first absorption cycle only magnesium participates in reversible sorption.

Table 4-2- Theoretical versus experimental (recorded on the second sorption cycle) hydrogen capacities of different Mg-Ti composites. The maximum (theoretical) capacity here only takes into account magnesium.

Composition	Maximum reversible H exchange capacity	Experimental capacity (2nd cycle)	Ratio %
Mg- 5 at.%Ti	7.54	1.57	21
Mg- 10 at.%Ti	6.82	4.33	63
Mg- 22 at.%Ti	5.33	4.06	76
Mg- 40 at.%Ti	3.57	2.34	65

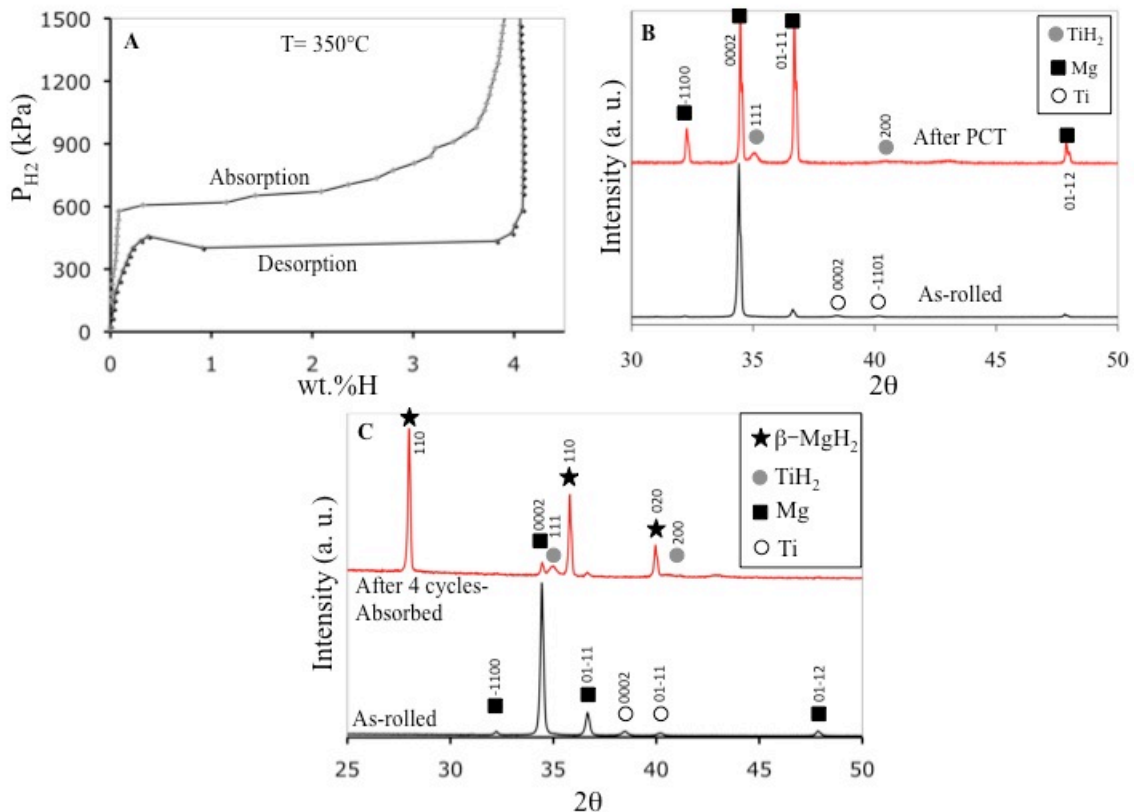


Figure 4-4- (A): Pressure – composition curve of the 15FR Mg- 22at.%Ti composite at 350°C. (B) XRD patterns of the composite in the as-rolled state and after the PCT experiment (desorbed). (C) XRD patterns of as-rolled compared to the absorbed state of Mg-22 at.%Ti sample (50FR).

The difference observed between absorption and desorption thermodynamics is generally associated with the asymmetry of the nucleation barrier for the hydride vs. the metal and the irreversible work associated with each [33].

The crystal structures of the phases present in both absorbed and desorbed states were determined from XRD. Figure 4-4B compares the XRD plots of the as-rolled Mg-22 at.%Ti (15FR) sample to that of the same sample but after undergoing the PCT experiment (PCT curve presented in Figure 4-4A). Both plots have been normalized with respect to the 0002 Mg reflection intensity. The intensities of the diffracted Ti peaks are relatively low. This is due to the absorption of X-ray by the magnesium matrix, leaving behind a weak diffracted intensity from the embedded Ti phase. Assuming a mass absorption coefficient of $39.55 \text{ cm}^2/\text{g}$ for Mg (for Cu-K α radiation) [34], at 40° in 2θ the x-ray beam loses 90% of its intensity after passing about $57 \text{ }\mu\text{m}$ of Mg. The as-rolled state shows a strong rolling texture. This texture has diminished in the post-PCT state, and Ti has fully transformed to TiH_2 (Fm-3m – 225, $a = 4.45 \text{ \AA}$). The heat of formation for TiH_2 has been reported to be -130 kJ/mole [35], which means that the equilibrium hydrogen pressure for this hydride at 350°C is around 2.7 kPa (0.027 atm), much lower than our operating pressure during desorption ($\sim 0.05 \text{ MPa}$). Hence the hydrogen absorbed in generating TiH_2 is not reversible under our experimental conditions. Figure 4-4C compares the XRD of the as-rolled state of one of the composites (Mg-22 at.%Ti sample – 50FR) to that of the absorbed state, showing MgH_2 as the active hydrogen cycling phase.

4-3-2- Mg-22 at.%Ti, Effect of number of FR

In order to investigate the effect of number of fold and rolls on the resulting hydrogen sorption kinetics, we maintained the Ti content constant at 22 at.% and prepared four samples with 15, 30, 50 and 90 operations of FR. Figure 4-5 presents the typical microstructures of Mg- 22 at.% Ti composites rolled and folded for different repetitions. With increasing number of FR operations, the Ti layers show progressively more necking. Two clear examples of this are marked with white arrows in Figure 4-5C. In 50 and 90FR composites, the Ti aggregates that are clearly layered are less discernible.

This necking process results in a wider size distribution of Ti particles (Figure 4-6D). Multiple necking of the hard phase in bi-metallic laminates prepared by cold rolling and folding is well established [36].

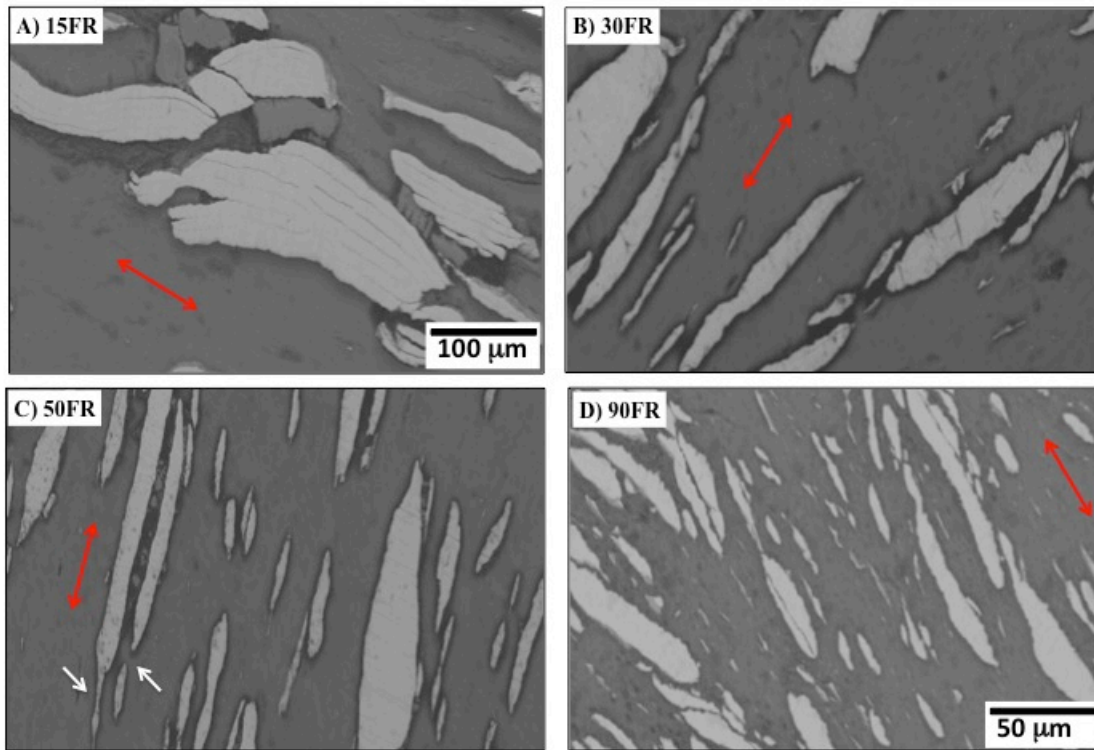


Figure 4-5- SEM micrographs showing the as-rolled microstructure of the Mg-22 at.%Ti composites. The arrows show the approximate trace of the rolling plane. White arrows in (C) mark necking events. The images are at the same magnification, except for D).

The average grain size and dislocation density as a function of FR number, calculated using MWP-fit analysis methodology is presented in Figure 4-6. The volume averaged grain size essentially varies very little up to 50FR (Figure 4-6A), and after that point drops significantly for 90FR sample. Again, since the number of peaks available for Ti were limited, the margin of error in calculated dislocation density and grain size in Ti is significant. The dislocation density values in magnesium matrix show an analogous trend to what we observed in the case for varying Ti content (Figure 4-6B, also see Figure 4-2B). The calculated ρ value peaks at 15FR sample, and decreases for increasing folding and rolling passes. Here it seems that the recovery in Mg has proceeded in a larger extent in 90FR sample, showing a substantial reduction in the dislocation density.

Dislocation density in Ti (Figure 4-6C), also similar to what we saw in the previous section, shows consistently higher values compared to Mg.

The first hydrogen absorption cycle kinetics for the Mg-22 at.%Ti, with differing FR number, is presented in Figure 4-7A. For the samples with lower numbers of FR (15 and 30) there appears to be a distinctive rise in the absorption rate during the activation step after around 25 hours of hydrogen exposure. This step becomes flatter and less

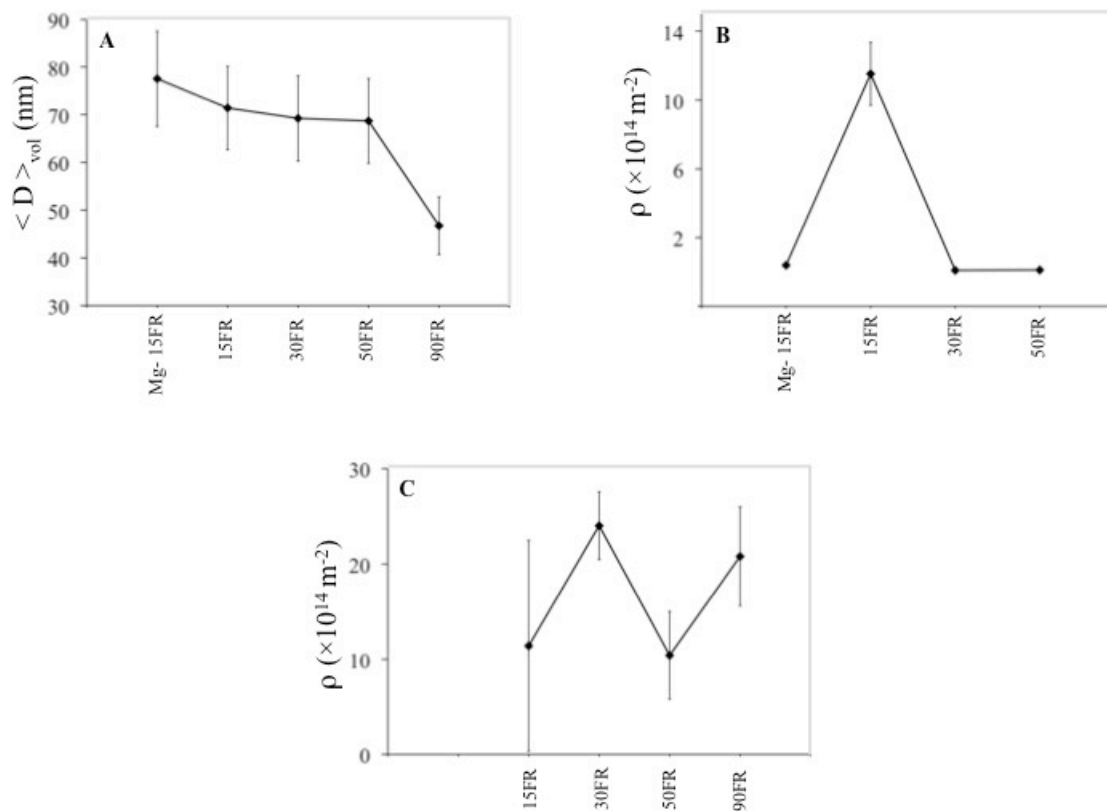


Figure 4-6- Results of the multiple whole profile (MWP) fitting analysis on the XRD data for Mg-22 at.%Ti composites with different number of FR operations. (A) Mg volume weighted average grain size. (B) Dislocation density in Mg. (C) dislocation density in Ti.

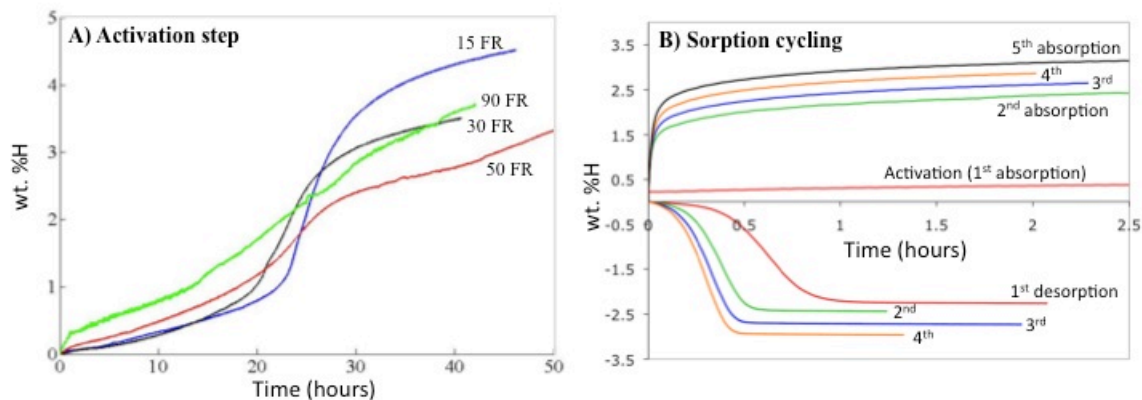


Figure 4-7- (A) Comparison of the first absorption cycle for the 22at.%Ti composites, but with varying FR number, tested at 350°C. (B) Hydrogen sorption cycling kinetics of the Mg-22at.%Ti 50FR composite.

prominent for samples with higher number of FR, almost non-existing for 90FR sample. Figure 4-7B shows the cycling behavior of 50FR Mg-22at.%Ti composite. Even with this many fold and roll operations, the initial absorption rate is very slow relative to that in the subsequent cycles. In fact, the absorption kinetics improves up to cycle 5, after which point they remain relatively stable. Similarly the desorption kinetics also improve with cycling. This result demonstrates that though the fold and roll process is useful to minimize the preliminary unacceptably slow sorption kinetics, it does not eliminate the activation period entirely. Figure 4-7B also demonstrates that with a sufficiently high distribution of the TiH₂ phase it is possible to achieve a fairly rapid - on the scale of minutes - absorption and desorption cycling of the MgH₂-TiH₂ composite.

In order to investigate the origin of the step observed on the first absorption curve of the Mg-22 at.% Ti 15FR sample (Figure 4-7A), we quenched two pieces of this composite at different stages of activation (See Figure 4-8A): One early within the initial incubation stage (with 0.26 wt.% hydrogen uptake) and the other one at the wake of the step (with 1.6 wt.% uptake of hydrogen). Figure 4-8B compares the XRD plots of these two quenched samples with the as-rolled specimen. In the sample quenched at 0.26 wt.%H no MgH₂ was detected. Since the peaks corresponding to TiH₂ happen to be close to major Mg and Ti reflections it is hard to rule out the presence of this phase. If we assume that all the absorbed hydrogen in this case is in the form of solid solution in α -Mg and α -Ti we can back-calculate the absorbed hydrogen. At 350°C and 2 MPa hydrogen

pressure, magnesium dissolves 0.02 H/Mg (0.83 ppm) atomic ratio of hydrogen [37]. Hydrogen solubility in titanium at this condition is 0.072 H/Ti atomic ratio (1.506 ppm) [38]. Given these values, for Mg- 22 at.% Ti, only 0.11 wt.% H can be absorbed exclusively through solid solution at the given temperature and pressure. The rest of the hydrogen (0.15 wt.%) has to be absorbed by forming a hydride phase, but the volume fraction of the hydride is most likely below the detection limit of x-ray diffraction.

The sample quenched at 1.6 wt.%H (Figure 4-8B) shows no metallic titanium present (the Ti-0002 reflection at 38.5° disappears), and by inference one can conclude that all have transformed to TiH_2 . At the same time magnesium is partially transformed into MgH_2 . This observation indicates that full hydrogenation of titanium happens in advance of substantial formation of MgH_2 .

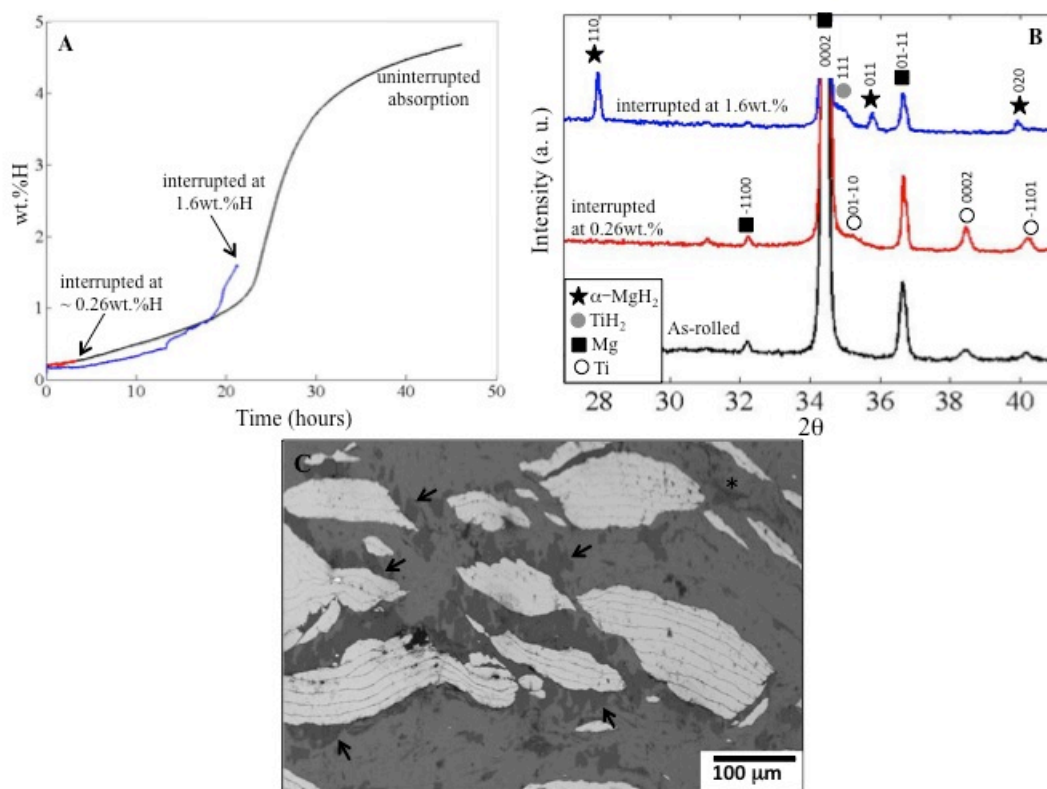


Figure 4-8- First absorption cycle for Mg-22 at.% Ti 15FR composite (A) Interrupted and full absorption curves, (B) XRD patterns. (C) SEM micrograph of the cross-sectioned composite absorbed with 1.6wt.%H. Arrows point to MgH_2 (darker regions) nucleated in the proximity of TiH_2 .

Figure 4-8C shows cross sectional micrograph of the 15FR Mg-22 at.%Ti composite hydrogenated to 1.6 wt.%. In back-scattered electron imaging mode the MgH_2 phase could be straight-forwardly identified relative to the metallic Mg matrix and the cracks and free surfaces between the layers: The “globular” nucleated MgH_2 phase shows a darker contrast relative to the Mg matrix, whereas the two-dimensional traces of cracks and non-metallurgically bonded interfaces show up as entirely black regions. Since the characteristic metallic Ti reflections were unambiguously absent after 1.6 wt.% H absorption, we assume that the secondary phase of the microstructure (brightest regions) is TiH_2 . Considering the distribution of the MgH_2 phase in these micrographs, one can recognize that this phase tends to nucleate in close proximity to the TiH_2 particles. A secondary preferential location for MgH_2 nucleation was at cracks and non-metallurgically bonded interfaces, also known as “kissing bonds”. An asterisk marks one such region, located in the top right corner of the micrograph. “*Kissing bond*” is a term used in solid-state welding literature referring to a condition that the two metallic sheet surfaces are sufficiently mechanically close together to appear joined when examined by conventional microscopy, but actually do not form a true metallurgical bond [39, 40]. Such bonds may certainly be present within these composites, and would be permeable to hydrogen gas during sorption.

An identical sorption-interruption experiment was conducted on the Mg-22 at.% Ti 90FR sample. It took 20 hours to absorb this much hydrogen, with the absorption rate being close to constant the entire time. As expected, the XRD analysis indicated that the metallic Ti peaks were largely absent, and that some $\alpha\text{-MgH}_2$ did form. Figure 4-9 shows the non-sigmoidal absorption curve (4-9A), the XRD patterns (4-9B), and the partially (1.6 wt.%) absorbed microstructure (4-9C). With increasing levels of folding and rolling, the distribution of the Ti (or TiH_2) becomes finer and more dense. As a result, the nucleation density of the MgH_2 phase around the particles increases as well. SEM characterization of this sample (Figure 4-9C) demonstrates that the preferred location for MgH_2 nucleation is neighboring Ti/ TiH_2 particles.

The distribution of the MgH_2 proved to be different for the composites that have undergone several absorption-desorption cycles. Figure 4-10 presents a representative case for 15 FR Mg-22 at.%Ti (15FR) quenched at 2.5 wt.%H on the third absorption

cycle (while absorbing). While some nucleation is observed near the TiH_2 particles, much of the Mg surrounding the TiH_2 remain metallic even at this higher hydrogen content. Rather, MgH_2 growth seems more concentrated in the proximity of highly cracked regions. Such cracks, arrowed on the right side of the image, were present in much more copious numbers after hydrogen cycling. It is quite likely that they have formed as a result of the stresses associate with the Mg to MgH_2 , and vice versa, phase transformation. The expansion mismatch between the Mg (MgH_2) and the TiH_2 phase should also generate such cracking. The regions that were not cracked, e.g. the middle to left side of the micrograph, displayed markedly less MgH_2 formation despite the presence of the TiH_2 phase.

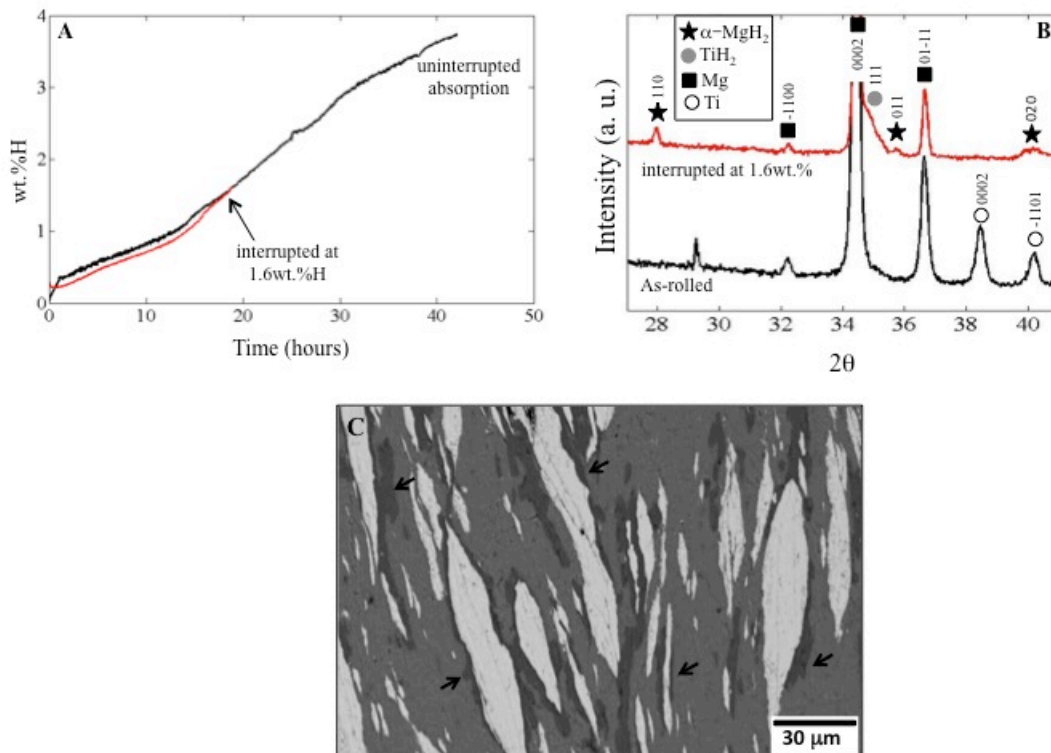


Figure 4-9- First absorption cycle for Mg-22 at.% Ti 90FR composite (A) Interrupted and full absorption curves (B) XRD patterns. (C) SEM micrograph of the cross-sectioned composite absorbed with 1.6wt.% H. Arrows point to MgH_2 (darker regions) nucleated in the proximity of TiH_2 .

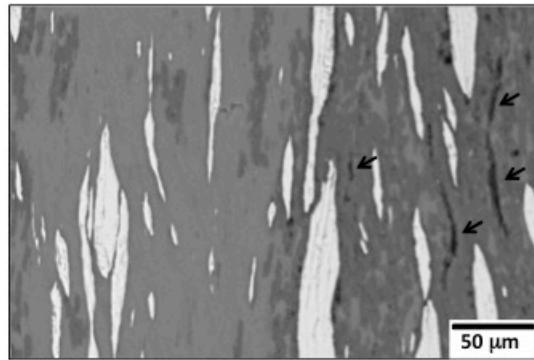


Figure 4-10- SEM micrographs from the Mg- 22 at.% Ti 15 FR composite, quenched at 2.5 wt.% H on the third absorption cycle.

4-3-3- Mg-Stainless Steel Composites

In the previous section we examined hydrogen sorption properties of Mg-Ti composites with the secondary phase (Ti) forming a hydride phase. It is interesting to compare those results to that of magnesium - stainless steel, where the majority austenitic iron phase of the steel will not form any stable hydrides at the testing conditions. Four samples with different loadings of stainless steel (1, 5, 8 and 18 vol. %) were folded and rolled for 15 times. Hydrogen sorption kinetics of these four samples for the first two cycles is presented in Figure 4-11. The test on Mg-1 vol.% SS was discontinued after the first cycle due to extreme slowness. Although their volume fractions are nearly identical, both the initial and the composite geometries of the SS phase are different from the Ti phase, precluding a direct comparison. However the general effect of the second phase addition is quite similar: Up to a certain point, with increasing amounts of SS addition, the kinetics continues to improve. However at even higher SS content, the kinetics begin to degrade. Naturally, increasing the volume fraction of the SS decreases the overall hydrogen capacity.

Figures 4-12A through 4-12C highlight the microstructure of the Mg-5 at.% SS (A) and (B), and Mg-18 at.% SS (C) samples, both absorbed to 1 wt.% hydrogen. The cross-sections illustrate that there is no homogeneous nucleation of the MgH_2 phase. Arrows point to typical nucleation sites, which include the SS-Mg interfaces, large cracks and free surfaces. Even the MgH_2 grains that do not appear to be associated with a visible

defect have one edge with a planar morphology (e.g. MgH_2 grains arrowed in Figure 4-8C), indicating heterogeneous nucleation on some defect. Of the heterogeneous nucleation sites, another potential location for MgH_2 formation may be on the “kissing bonds” formed between sheets of layered magnesium. The sparseness of the nuclei even at free surfaces suggests a strong crystallographic dependence of MgH_2 on Mg nucleation, with certain, perhaps low index, Mg surface orientations being favorable.

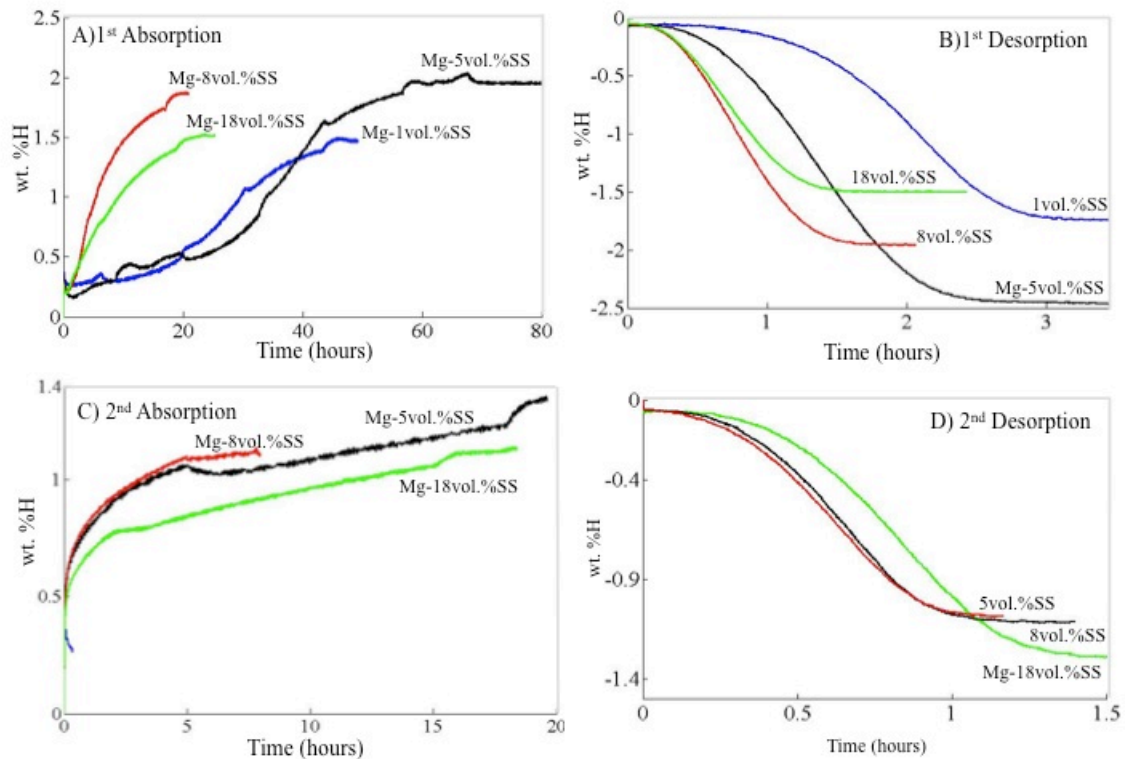


Figure 4-11- Hydrogen sorption kinetics of 15 FR Mg-SS composites, tested at 350°C: (A) Activation, (B) 1st desorption, (C) 2nd absorption, and (D) 2nd desorption. The test for Mg- 1vol.% SS was discontinued after the first cycle due to sluggish kinetics.

4-4- Discussion

It is instructive to compare the results of the first section of the present study (Mg-Ti composites) with the hydrogen sorption properties reported for the ball-milled Mg-Ti system. After milling Mg-20 at.% Ti for 31 hours, Liang and Schulz [41], reported a

maximum of 12.5 at.% Ti solution in the magnesium matrix, still maintaining the hexagonal crystal structure. Upon first hydrogen absorption and desorption though the dissolved Ti precipitates and, along with the free Ti embedded in Mg, forms TiH_2 , with the rest of the hydrogen absorbed in MgH_2 phase. Like our observations here, the subsequent hydrogenation (dehydrogenation) cycles only entails formation (decomposition) of MgH_2 . The activation of this sample takes about 8.3 hours, which is much faster than our case (about 40 hours, see Figures 4-3A and 4-7A). Given that the powder milling and handling was performed under inert atmosphere this is expected. Similar to the observed activation behavior of our Mg- 22 at.% Ti samples with lower FR numbers (15 and 30 FR samples in Figure 4-7A), they also report a step at which the activation rate changes pace. They correlate this first step to the formation of TiH_2 , while not presenting any experimental evidence for it.

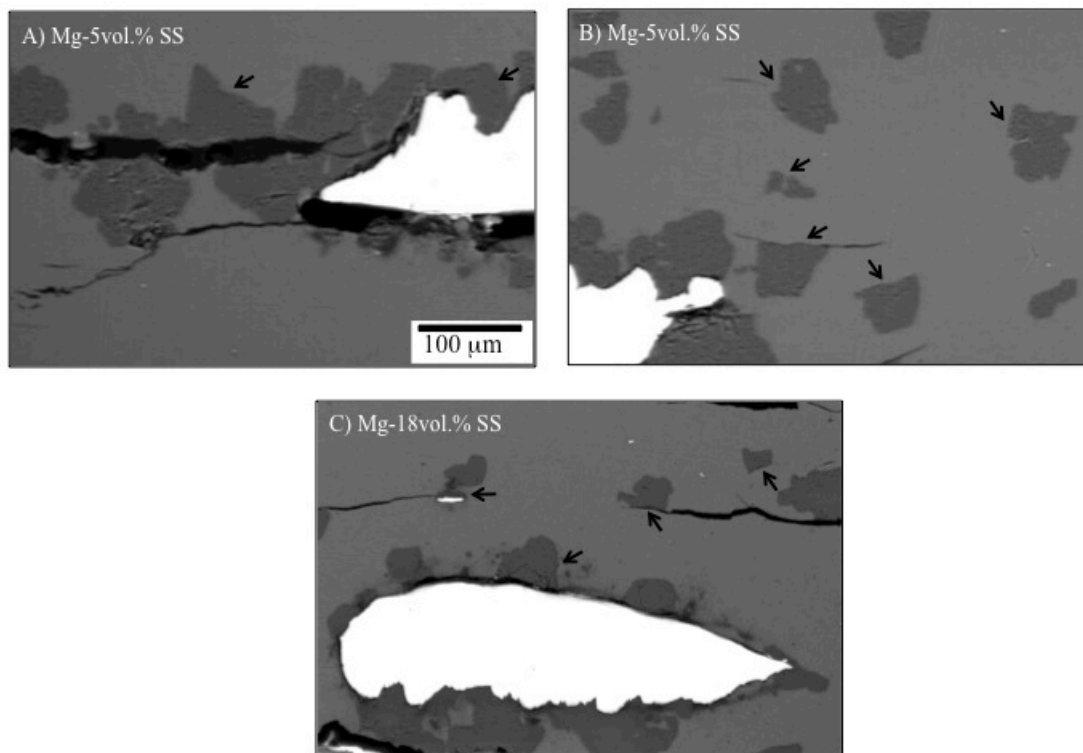


Figure 4-12- Microstructure of Mg-SS composites interrupted on their first absorption cycle at ~ 1 wt.% H, showing the nucleation sites of MgH_2 (arrowed). (A) Hydride nucleation in Mg-5 vol% SS samples near the stainless steel particles and at cracks. (B) Hydride nucleation in Mg-5 vol% SS samples near smaller cracks and other heterogeneous nucleation sites. (C) Hydride nucleation in Mg-18vol%SS composite.

The picture for folded and rolled Mg-Ti composites is more complicated than the above. Figure 4-13 presents the derivatives (with respect to time) of the first absorption step plots of Mg-Ti composites (For the original data refer to Figures 4-3A and 4-7A). The derivative in each case was calculated after smoothing the raw data with a standard floating-point average procedure in MATLAB. The effect of Ti content on the rate of activation is presented in Figure 4-13A. The arrows at the top show the time corresponding to the hydrogen uptake, taking only Ti into account (This can be easily calculated to result in 0.4, 0.75, 1.5, 2.4 wt.% H for the four Ti loading values we used, i.e. 5, 10, 22 and 40 at.% Ti, respectively). The corresponding time values were read from the activation plots presented in Figure 4-3A, also considering the $\sim 0.1\%$ initial offset due to volume expansion.

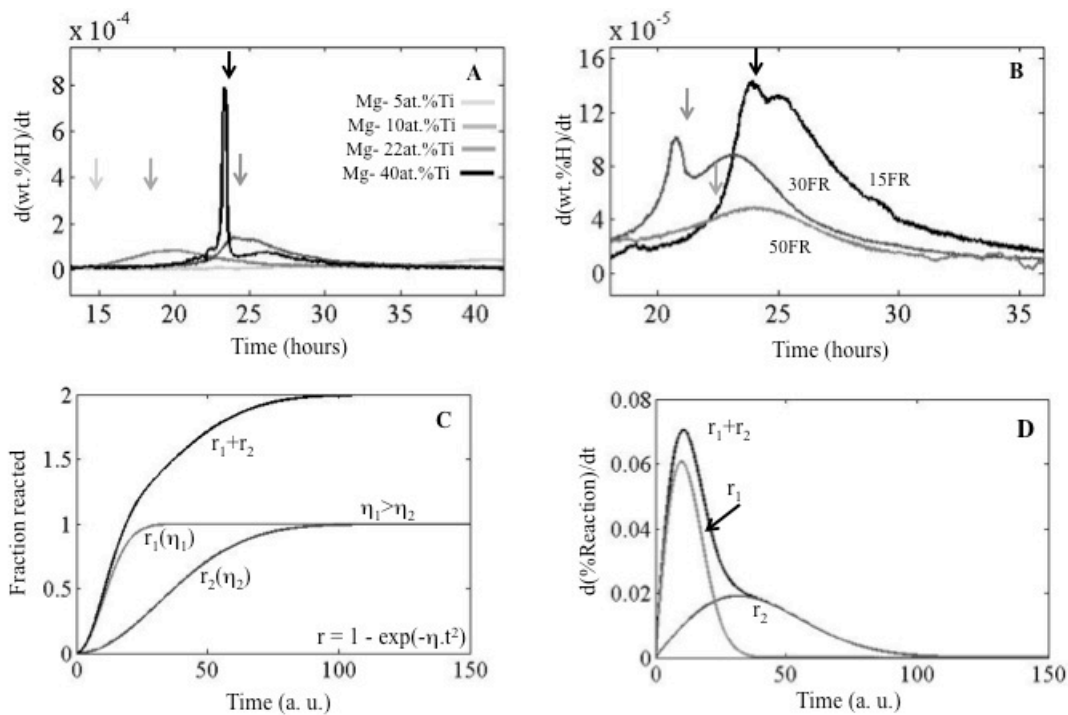


Figure 4-13- (A) and (B) First derivatives with respect to time of activation steps of Mg-Ti composites with different compositions (raw data presented in Fig. 3A), and Mg-22 at.% Ti with various FR number (raw data plot presented in Fig. 7A), respectively. (C) a schematic demonstration of two concurrent reactions with different rate constants. (D) time derivative of the model data presented in (C).

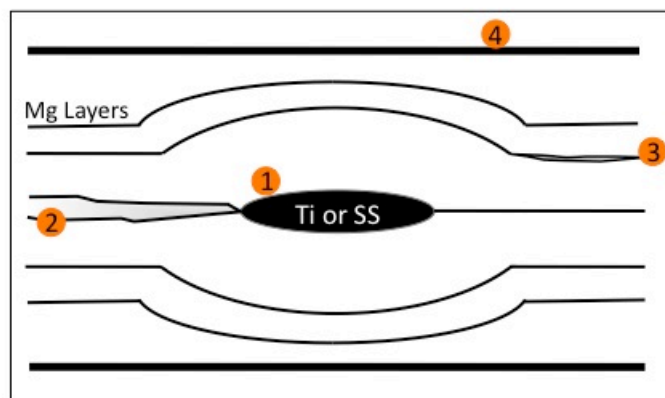


Figure 4-14- Schematic of the potential nucleation sites in Mg- composite system: (1) the incoherent interface between the hard phase and the magnesium (2) cracks, (3) kissing bonds and (4) external surfaces. Hydrogenation on location (4) was only occasionally observed.

As can be observed in Figure 4-13A, the derivative plots show two neighboring peaks. These two can be seen quite distinctively in samples with 22 and 40 at.% Ti contents. They look closely merged in 10 at.% Ti sample, and only one peak can be observed for the 5 at.% Ti sample. The position of the arrows (same color-coding as the graph) in this plot closely correlates with the first of these two peaks, Mg- 5 at.% Ti sample being an exception showing a large discrepancy between the existing single peak and the arrow. The observed double-peak in the time derivatives of the activation steps correspond to the two overlapping sigmoidal curves for the hydrogenation of Ti and of Mg. This is shown in a model data presented in Figure 4-13C, presenting two concurrent reactions with different rate constants. To model the reaction kinetics here we have used the equation $r = 1 - \exp(-\eta \cdot t^2)$, where r is fraction transformed, η is the reaction constant and t is time. The overall reaction kinetics is represented by the addition of the two individual sigmoidals (r_1+r_2). By acquiring the time derivative of the overall reaction kinetics (Figure 4-13D) one can demonstrate the two separate reactions, each exhibiting a peak marking the inflection point of the corresponding single-reaction sigmoidal curve. The plots reported for the first absorption cycles of Mg-Ti composites (Figs. 4-3A and 4-7A) are in effect analogous to the (r_1+r_2) case of Figure 4-13C.

In the case observed in Figure 4-13A the first peak can be correlated to TiH_2 formation. Our experimental observations on quenched samples shows that full

hydrogenation of Ti precedes that of Mg (refer to Figure 4-8 and the relating text in the results section). Here in Figure 4-13A also one can recognize the close proximity of the time required to reach full Ti hydrogenation (arrows) to the first peak in $d(\text{wt.}\%H)/dt$ versus time plot, marking the inflection point of the first sigmoidal curve as the point of TiH_2 formation. This independently suggests that the process of hydrogenation in Ti reaches its completion before that of Mg.

The position of the first peak in the plots presented in Figure 4-13A may depend on the geometrical distribution of the Ti phase, weather they lie close to the surface or are deeply embedded within the magnesium matrix. It also depends on the size distribution of Ti particles. This can be readily observed in Figure 4-18B. Here we are presenting the time derivatives of the Mg- 22 at.% Ti samples activation steps folded and rolled for various repetitions (Raw activation data can be found in Figure 4-7A). Derivative for 90FR data is not presented here due to high level of noise. For 15 FR and 30 FR samples the two peaks are prominently present and the first peaks for both cases correspond well to the time required for full Ti hydrogenation. Here the arrows mark the time required to reach the capacity if only Ti is taken into account (here: 1.5 wt.% H), read from the kinetics plot presented in Figure 4-7A. Both peaks for the 30 FR sample occur at shorter times compared to the 15FR specimen. The only observed significant difference between these two samples is smaller size of the Ti phase (refer to the micrographs in Figure 4-5). The picture for 50 FR sample is completely different from the above, showing only one broad peak in the $d(\text{wt.}\%H)/dt$ versus time plot. Looking back to the SEM micrographs presented in Figure 4-5, 50 FR was the stage that the Ti particles started to show extensive necking. That resulted in a much broader size distribution of the Ti phase, with the necked regions being much smaller in size than the rest. This has caused the two initially separate sigmoidals to merge, showing up as a single peak in Figure 4-13B.

Such sigmoidal shape is known to be associated with nucleation-limited reactions [42], and is distinctly absent in Mg-Ti and Mg-Fe-Ti alloys were a high density of heterogeneous nucleation sites is available [43, 44]. In contrast, the specimens that have undergone more FR operations show fairly constant absorption rates from the start. This means that available heterogeneous nucleation sites are abundant, which is evidently true by looking at the microstructures at this stage (See Figure 4-5C and 4-5D). This causes

the two reaction curves to merge with no trace of the sigmoidals (For example see 50FR sample plot in Figure 4-13B). The fact that the Ti sigmoidal precedes that of the Mg in majority of the cases means that the reaction rate constant is larger for Ti hydrogenation (See Figure 4-13C). This can be both correlated to higher nucleation rate (TiH_2 is thermodynamically more stable) and also better kinetics (growth rate).

Another important trend to follow and interpret here is the activation kinetics in Mg-Ti samples with different Ti loadings (See Figure 4-3A), also with various numbers of folding and rolling (See Figure 4-7A). Our microscopy observations have shown that the hydride growth front during activation step is more concentrated around the Ti particles (See micrographs in Figures 4-8 and 4-9). This was not the case for the subsequent cycles, meaning that the same close spatial correlation between the growing hydride phase and the Ti phase was not observed for the samples quenched on their 2nd or 3rd cycles (See micrograph in Figure 4-10). The plausible explanation, since the Ti phase is harder than the magnesium matrix, is the potential effect of the induced localized strain surrounding the Ti particles on preferential hydrogenation of these regions. In the experiments we performed on Mg-stainless steel composites, titanium was replaced with a non-hydride-forming second phase with no catalytic behavior towards hydrogen. Since stainless steel is still harder than the magnesium matrix the hypothesis mentioned above can be put to trial more directly.

As shown in Figure 4-11A for the Mg-SS samples, increasing the SS content in these composites produces an enhancement in the activation kinetics. The kinetics is fastest for Mg-8 vol.% SS sample, showing a decline with more addition of SS (See the plot for Mg-18 vol.% SS). Microscopy on the cross-sections of the quenched samples (Figures 4-12) show that there are a number of preferential locations for MgH_2 nucleation, namely: in the vicinity of the embedded SS particles, cracks, kissing bonds and other defect sites within the magnesium matrix, and also the free external surface of the composite. For samples with higher SS content, there seems to be a more dense concentration of hydride grains neighboring this hard second phase (Figure 4-12C), whereas at lower loadings of SS the contributions of the various nucleation sites tend to be more evenly distributed (Figure 4-12B).

Figure 4-14 provides a schematic of the available heterogeneous nucleation sites for the hydride phase. Our observations suggest that type 1, *i.e.* close to the strain field induced by the secondary hard phase, is the most favorable. Higher density of defects (dislocations and twins) can lower the nucleation barrier of the new phase and also facilitate higher diffusivity for hydrogen. These defects have been proven to be crucially important in enhancing the kinetics for the reverse scenario, desorption of MgH_2 , as well [45, 46]. Cracks and kissing bonds (sites 2 and 3 in Figure 4-14) can be deemed fairly equally favorable. Increasing the population of the hard phase and hence increasing the occurrence of the localized strain fields will be accompanied by an enhancement in activation kinetics (As observed in Figure 4-3A and 4-11A). But there is a saturation limit to this enhancement. Once the loading level of the secondary phase passes this threshold, the strain fields overlap and lose their efficiency on the kinetics enhancement. That is potentially the reason behind the observed slight deterioration of the activation kinetics for the highest SS content case in Figure 4-11A. Also upon cycling these highly deformed areas would disappear, and this can explain our microscopy observations after number of cycles showing low correlation between the hydride grains and the secondary hard phase.

Looking closer to the microstructure and phase distribution in the partially absorbed samples, both for Mg-Ti (Figures 4-8 and 4-9) and Mg-SS (Figure 4-12), one common observation is that the MgH_2 phase rarely can be seen to be formed on the external surface of the composites (type 4 sites in Figure 4-14). This is due to the presence of the magnesium oxide layer. This layer can be physically ruptured during folding and rolling processes (along the kissing bonds), and more so closer to the secondary hard phase due to a more localized deformation. Also, density functional theory (DFT) simulations have demonstrated that a defective Mg surface containing vacancies has much lower (an order of magnitude lower) adsorption energy for hydrogen molecule compared to the ideal surface [47]. Hence the observed spatial distribution of the MgH_2 phase during activation can also be attributed to the defective oxide layers in the proximity of the above sites combined with the high density of defects in the same regions.

In summary, we believe that through two main general contributions the activation kinetics of the Mg-Ti and Mg-SS folded and rolled composites are enhanced, as compared to pure magnesium. The activation process can be divided into two steps: surface activation and bulk activation [48]. Rolling and folding can enhance the kinetics of the initial surface activation through the defects induced in the surface oxide layer, rendering it more permeable to the incoming hydrogen molecules. Bulk activation kinetics is also significantly enhanced due to the presence of highly deformed regions in the vicinity of the harder second phase, providing energetically favorable locations for heterogeneous nucleation of the hydride phase.

4-5- Summary and Conclusion

We have prepared bulk magnesium - titanium and magnesium - stainless steel multilayer composites by accumulative roll-bonding (ARB). These structures created by repetitive cold rolling and folding of stacked layers, demonstrate significantly faster hydrogenation rate during the first hydrogen absorption cycle (also termed “activation”) relative to cold-rolled pure magnesium. The composites are also hydrogen cycleable at 350°C. For example, by the fifth hydrogenation cycle, the Mg-22 at.% Ti composite that has undergone 50 fold and rolled (FR) operations can absorb and desorb over 2.5 wt.% hydrogen in minutes.

For both magnesium - titanium and magnesium - stainless steel, excessive amounts of the hard phase addition reduced the operating hydrogen capacity. On the other hand too little of each phase resulted in slower kinetics. In the case of the Mg-Ti composites, the TiH_2 that formed during activation was stable throughout the subsequent absorption/desorption cycling.

Microscopy analysis performed on partially absorbed Mg-Ti and Mg-SS composites during the first absorption cycle showed that initial MgH_2 formed primarily in the proximity of the second phase particles. Conversely, in the partially hydrogen absorbed Mg-Ti samples that have undergone hydrogenation cycling, MgH_2 nucleation conspicuously occurred at gas permeable interfaces such as cracks. We therefore believe that the primary role of either second phase at absorption cycle 1 is to provide

heterogeneous nucleation sites for MgH_2 formation. Other heterogeneous nucleation sites become important once the sample is activated.

4-6- References

- 1 Jain IP, Lal C, Jain A. Hydrogen storage in Mg: A most promising material. *Int. J. of Hydrogen Energy* 2010; 35: 5133-5144.
- 2 Ma L-P, Wang P, Cheng H-M. Hydrogen sorption kinetics of MgH₂ catalyzed with titanium compounds. *Int. J. of Hydrogen Energy* 2010; 35: 3046-3050.
- 3 Mao J, Guo Z, Yu X, Liu H, Wue Z, Ni J. Enhanced hydrogen sorption properties of Ni and Co-catalyzed MgH₂. *Int. J. of Hydrogen Energy* 2010; 35: 4569-4575.
- 4 Skripnyuk VM, Rabkin E, Bendersky LA, Magrez A, Carreno-Morelli E, Estrin Y. Hydrogen storage properties of as-synthesized and severely deformed magnesium-multiwall carbon nanotubes composite. *Int. J. of Hydrogen Energy* 2010; 35: 5471-5478.
- 5 Yu XB, Yang ZX, Liu HK, Grant DM, Walker GS. The effect of a Ti-V-based BCC alloy as a catalyst on the hydrogen storage properties of MgH₂. *Int. J. of Hydrogen Energy* 2010; 35: 6338-6344.
- 6 Pauw BR, Kalisvaart WP, Tao SX, Koper MTM, Jansen APJ, Notten PHL. Cubic MgH₂ stabilized by alloying with transition metals: A density functional theory study. *Acta Mater.* 2008; 56(13): 2948-2954.
- 7 Du AJ, Smith SC, Lu GQ. First-principle studies of the formation and diffusion of hydrogen vacancies in magnesium hydride. *J. Phys. Chem. C* 2007; 111(23): 8360-8365.
- 8 Rudman PS. Hydrogen-diffusion-rate-limited hydriding and dehydriding kinetics. *J. Appl. Phys.* 1979; 50(11): 7195-7199.
- 9 Schober T. The Magnesium-hydrogen system- transmission electron microscopy. *Metall. Trans. A* 1981; 12A(6): 951-957.
- 10 Eigen N, Keller C, Dornheim M, Klassen T, Bormann R. Industrial production of light metal hydrides for hydrogen storage. *Scripta Materialia* 2007; 56(10): 847-851.
- 11 Saito Y, Utsunomiya H, Tsuji N, Sakai T. Novel ultra-high straining process for bulk materials - Development of the accumulative roll-bonding (ARB) process. *Acta Materialia* 1999; 47(2): 579-583.
- 12 Jiang L, Perez-Prado MT, Gruber PA, Arzt E, Ruano OA, Kassner ME. Texture, microstructure and mechanical properties of equiaxed ultrafine-grained Zr fabricated by accumulative roll bonding. *Acta Materialia* 2008; 56(6): 1228-1242.
- 13 Sieber H, Park JS, Weissmuller J, Perepezko JH. Structural evolution and phase formation in cold-rolled aluminum-nickel multilayers. *Acta Materialia* 2001; 49(7): 1139-1151.

- 14 Dufour J, Huot J. Rapid activation, enhanced hydrogen sorption kinetics and air resistance in laminated Mg-Pd 2.5 at.%. *Journal of Alloys and Compounds* 2007; 439(1-2): L5-L7.
- 15 Takeichi N, Tanaka K, Tanaka H, Ueda TT, Tsukahara M, Miyamura H, Kikuchi S. Hydrogen storage properties and corresponding phase transformations of Mg/Pd laminate composites prepared by a repetitive-rolling method. *Materials Transactions* 2007; 48(9): 2395-2398.
- 16 Takeichi N, Tanaka K, Tanaka H, Ueda TT, Kamiya Y, Tsukahara M, Miyamura H, Kikuchi S. Hydrogen storage properties of Mg/Cu and Mg/Pd laminate composites and metallographic structure. *Journal of Alloys and Compounds* 2007; 446(Sp. Iss. SI): 543-548.
- 17 Dufour J, Huot J. Study Of Mg₆Pd alloy synthesized by cold rolling. *Journal of Alloys and Compounds* 2007; 446(Sp. Iss. SI): 147-151.
- 18 Suganuma K, Miyamura H, Kikuchi S, Takeichi N, Tanaka K, Tanaka H, Kuriyama N, Ueda TT, Tsukahara M. Hydrogen storage properties of Mg-Al alloy prepared by super lamination technique. *Advanced Materials Research* 2007; 26-28: 857-860.
- 19 Ueda TT, Tsukahara M, Kamiya Y, Kikuchi S. Preparation and hydrogen storage properties of Mg-Ni-Mg₂Ni laminate composites. *Journal of Alloys and Compounds* 2005; 386(1-2): 253-257.
- 20 Mori R, Miyamura H, Kikuchi S, Tanaka K, Takeichi N, Tanaka H, Kuriyama N, Ueda TT, Tsukahara M. Hydrogenation characteristics of Mg based alloy prepared by super lamination technique. *Materials Science Forum* 2007; 561-565(1-3): 1609-1612.
- 21 Amira S, Santos SF, Huot J. Hydrogen sorption properties of Ti-Cr alloys synthesized by ball milling and cold rolling. *Intermetallics* 2010; 18(1): 140-144.
- 22 Couillaud, Enoki H, Amira S, Bobet JL, Akiba E, Huot J. Effect of ball milling and cold rolling on hydrogen storage properties of nanocrystalline TiV_{1.6}Mn_{0.4} alloy. *Journal of Alloys and Compounds* 2009; 484(1-2): 154-158.
- 23 Pedneault S, Huot J, Roue L. Nanostructured Mg₂Ni materials prepared by cold rolling and used as negative electrode for Ni-MH batteries. *Journal of Power Sources* 2008; 185(1): 566-569.
- 24 Chen CP, Liu BH, Li ZP, Wu J, Wang QD. The Activation mechanism of Mg-based hydrogen storage alloys. *Zeitschrift fur Physikalische Chemie-International Journal of Research in Physical Chemistry & Chemical Physics* 1993; 181(1-2): 259-267.

-
- 25 Leon A, Knystautas EJ, Huot J, Schulz R. Influence of the evaporation rate and the evaporation mode on the hydrogen sorption kinetics of air-exposed magnesium films. *Thin Solid Films* 2006; 496(2): 683-687.
- 26 Ungar T, Gubicza J, Ribarik G, Borbely A. Crystallite size distribution and dislocation structure determined by diffraction profile analysis: principles and practical application to cubic and hexagonal crystals. *Journal of Applied Crystallography* 2001; 34(3): 298-310.
- 27 Dragomir IC, Ungar T. Contrast factors of dislocations in the hexagonal crystal system. *Journal of Applied Crystallography* 2002; 35(5): 556-564.
- 28 Ribarik, G, Ungar T, Gubicza J. MWP-fit: a program for multiple whole-profile fitting of diffraction peak profiles by ab initio theoretical functions. *Journal of Applied Crystallography* 2001; 34(5): 669-676.
- 29 Gabor Ribarik (2008) *Modeling of diffraction patterns based on microstructural properties*, PhD Thesis, Department of Materials Physics, Eotvos Lorand University.
- 30 Fromageau R, Pastol JL, Revel G. Recrystallization of magnesium deformed at low temperatures. *Journal of Nuclear Materials* 1978; 74(2): 252-259.
- 31 Sharp JV, Mitchell A, Christian JW. The recovery of deformed cadmium, magnesium, zinc and cobalt. *Acta Metall.* 1965; 13: 965-971.
- 32 Humphreys FJ and Hatherly M, *Recrystallization and related annealing phenomena*, 2nd Edition, Elsevier, Oxford, 2004, p. 220.
- 33 Flanagan TB, Oats WA. In: Schlapbach L, editor. Hydrogen in intermetallic compounds I (topics in applied physics). Berlin: Springer; 1978. p. 49–85.
- 34 Lawrence JL. X-ray attenuation coefficients for magnesium and aluminum in the range 0.3 to 1.3Å. *Acta Crystallographia* 1979; A35: 845-848.
- 35 Luo W, Clewley JD, Flanagan TB. Calorimetrically measured enthalpies for the reaction of H₂(D₂) (G) with Ti and Ti-Ni alloys at 323K. *Metallurgical Transactions B* 1993; 24(5): 867-873.
- 36 Bordeaux F, Yavari R. Multiple necking and deformation-behaviour of multilayer composites prepared by cold-rolling. *Z. Metallkde* 1990; 81(2): 130-135.
- 37 San-Martin A, Manchester FD. The H-Mg System. *Bulletin of Alloy Phase Diagrams* 1987; 8(1): 431- 437.
- 38 Vitt RS, Ono K. Hydrogen solubility in alpha-titanium. *Metallurgical Transactions* 1971; 2(2): 608-609.

- 39 Oosterkamp A, Oosterkamp LD, Nordeide A. 'Kissing bond' phenomena in solid-state welds of aluminum alloys. *Welding Journal* 2004; 83(8): 225S-231S.
- 40 Mitlin D, Radmilovic V, Pan T, Chen J, Feng Z, Santella ML. Structure-properties relations in spot friction welded (also known as friction stir spot welded) 6111 aluminum. *Materials Science and Engineering A* 2006; 441(1-2): 79-96.
- 41 Liang G, Schulz R. Synthesis of Mg-Ti alloy by mechanical alloying. *Journal of Materials Science* 2003; 38(6): 1179-1184.
- 42 N. Gerard and S. Ono, *Hydrogen in Intermetallics II (Topics in Applied Physics)*, edited by L. Schlapbach, Springer-Verlag, Berlin, 1988, pp. 165-193.
- 43 Zahiri B, Harrower CT, Amirkhiz BS, Mitlin D. Rapid and reversible hydrogen sorption in Mg-Fe-Ti thin films. *Appl. Phys. Lett.* 2009; 95:103114.
- 44 Kalisvaart WP, Harrower CT, Haagsma J, Zahiri B, Luber EJ, Ophus C, Poirier E, Fritzsche H, Mitlin D. Hydrogen storage in binary and ternary Mg-based alloys: A comprehensive experimental study. *Int. J. of Hydrogen Energy* 2010; 35, 2091.
- 45 Danaie M, Mitlin D. TEM analysis and sorption properties of high-energy milled MgH₂ powders. *Journal of Alloys and Compounds* 2009; 476(1-2): 590-598.
- 46 Danaie M, Tao SX, Kalisvaart P, Mitlin D. Analysis of deformation twins and the partially dehydrogenated microstructure in nanocrystalline magnesium hydride (MgH₂) powder. *Acta Materialia* 2010; 58(8): 3162-3172.
- 47 Wu G, Zhang J, Wua Y, Li Q, Chou K, Bao X. The effect of defects on the hydrogenation in Mg (0 0 0 1) surface. *Applied Surface Science* 2009; 256: 46–51.
- 48 Schlapbach L, Surface properties and activation, in: Schlapbach L (Ed), *Hydrogen in Intermetallic Compounds II, Surface and dynamic properties and applications*, Springer-Verlag, Berlin, 1992, p. 41.

Chapter 5

Conclusions

In this thesis we examined two processes that can be utilized to enhance the hydrogen sorption kinetics of magnesium. Chapters 2 and 3 were focused on ball milling of magnesium hydride (α -MgH₂) powder, and in Chapter 4 we studied the accumulative roll bonding of two magnesium-based multilayer composites (Mg-Ti and Mg-SS). In both cases, we characterized the microstructure, in hydrogenated, desorbed or partially desorbed state. The main motivation for the above was to find correlations between the final observed properties of the processed hydride powder or the prepared composites and the characteristics of the corresponding microstructure. Besides yielding a mechanistic knowledge with regards to the hydrogen sorption and desorption reactions, this understanding can enable us to optimize the processing parameters such that they would be more conducive to enhanced properties.

As for the ball milled MgH₂, we demonstrate that the hydride microstructure can be directly studied by transmission electron microscopy (TEM), using a cryogenically cooled TEM sample holder. One main prominent feature in the ball milled hydride microstructure was presence of large density of deformation twins. Our extensive microscopy observations on both milled and annealed hydride samples resulted in the conclusion that ball milling induces deformation twins within the MgH₂ grains. While

both experimental measurements and DFT simulations rule out any thermodynamic destabilization caused by the existence of the twins, the kinetics of desorption show a substantial enhancement in presence of the twins. We believe this is either due to higher diffusivity of the hydrogen ions through the twin boundaries or twins acting as favorable locations for the heterogeneous nucleation of the metallic magnesium phase.

By examining the partially desorbed microstructure in ball milled MgH_2 , using energy filtering TEM, we demonstrate that the dehydrogenation phase transformation is a nucleation and growth process. Moreover, the nucleation step in this phase transition seems to be quite difficult. This is confirmed by observing only a few nucleation sites within the hydride matrix that construct the growth front. This is in contrast to the generally assumed “core-shell” microstructure during desorption, which would be a direct consequence of easy nucleation of the metallic magnesium phase.

With regards to the accumulative roll bonded composites; we demonstrate that these structures show much faster activation kinetics as compared to cold-rolled pure magnesium. For both Mg-Ti and Mg-SS cases, increasing the loading amount of the secondary phase to the composite enhances the kinetics of the hydrogen sorption and desorption reactions. This holds true only up to a threshold value, beyond which the hydrogen capacity of the composite would be compromised. The loss in hydrogen capacity in both cases is the direct result of the secondary phase not partaking in the hydrogen sorption and desorption reactions. In Mg-Ti, titanium reacts with hydrogen to form the stable TiH_2 phase during the first hydrogenation cycle and stays as such throughout the subsequent cycles. And in Mg-SS, stainless steel simply does not react with hydrogen.

Microscopy analyses of the partially hydrogenated composites, on their activation cycle, demonstrate that the nucleation of the hydride phase mainly occurs in the vicinity of the added secondary phase (Ti or SS). This close correlation was not observed in the fully activated composite samples. After number of hydrogenation and dehydrogenation cycles, other heterogeneous nucleation sites, e.g. cracks, free surfaces, and kissing bonds, come into play.

In both of the cases mentioned above we are dealing with the nucleation of a phase (Mg in the ball milled MgH_2 and MgH_2 in the multilayer composites) within a

matrix with significant difference in specific volume. This substantial volume change during a solid-state phase transition can give rise to large coherency stress values that can alter the equilibrium condition within such a system. This added stress term in the nucleation energy barrier can suppress the nucleation of the secondary phase until larger driving forces become available. In this context, the role of various crystallographic sites suited to act as heterogeneous nucleation sites are crucial. Abundance of these sites can result in enhanced kinetics of the reaction, by providing the possibility of nucleation at smaller driving forces.

Appendix 1

MgH₂ in the Transmission Electron Microscope

A section of this appendix has been published in: Danaie M, Malac M, Mitlin D. 2008; 14 (Suppl. 2): 278-288.

DOI: <http://dx.doi.org/10.1017/S1431927608088429>

As it was discussed in Chapters 2 and 3, magnesium hydride (MgH₂) is extremely unstable in TEM at room temperature and decomposes into a mixture of magnesium and magnesium oxide. In this appendix we will provide some data on the extent of instability of the hydride phase within the TEM and also, we will look into the thermodynamic stability of this phase in the microscope's environment.

In this experimental study we have measured electron doses required to decompose magnesium hydride to metallic magnesium for two different powders: (1) magnesium hydride powder that was ball milled in a pure argon atmosphere for 30 min (10:1 ball to powder weight ratio and 650 rpm rotation speed), (2) half of the milled batch was then annealed at 400°C in pressurized hydrogen (1.72 MPa). We used a JEOL

2200FS TEM operating at 200 kV accelerating voltage to study the electron beam-induced degradation at room temperature. We acquired series of diffraction patterns, at consecutively increasing irradiation doses, followed by radial integration and background subtraction to study the effect of electron irradiation¹. The decrease in integrated intensity of the diffraction rings indicates the loss of long-range order and transformation of MgH₂ into Mg and/or MgO.

Our measurements show that annealed MgH₂ powder completely transforms into magnesium after receiving 3.6 C/cm² (Figure A-1) at room temperature, but milled powder decomposes after 2.6 C/cm² (Figure A-2). In the case of annealed powder the initial large crystal of MgH₂ transforms to a fine-grained Mg. Figure A-3 shows the change in intensity of 110-MgH₂ reflections with increasing electron dose. Not only the milled sample is more susceptible to beam-induced degradation, but also its degradation behavior is different from that of annealed material. Our XRD experiments on the same samples have shown smaller grain size (14 nm versus 19 nm) and higher lattice strain (1.41×10^{-3} rms strain versus none) for milled sample. It appears that the difference in beam-induced damage properties of annealed and ball milled powders is closely related to the desorption behavior of milled and annealed samples respectively (referring back to Chapter 2, we know that milled powder sample shows faster desorption kinetics).

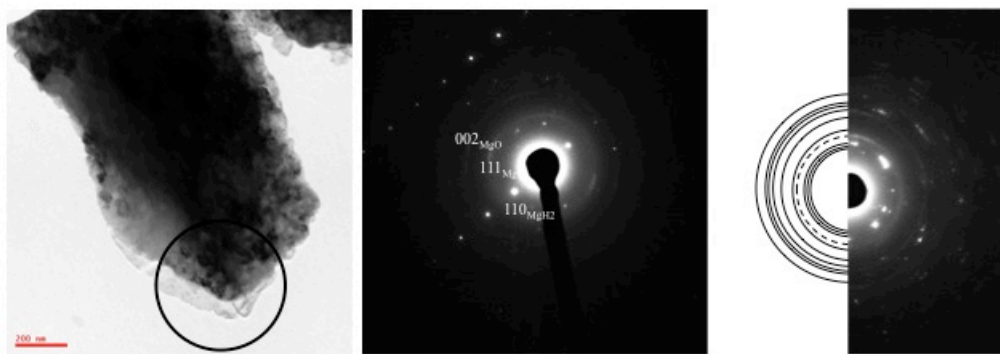


Figure A-1- Annealed MgH₂ (a) and corresponding diffraction patterns for (b) newly exposed and (c) after 3.6 C/cm². Simulation is for Mg and dashed line is 002_{MgO}. Ring in (a) designates selected area.

¹ We recognize here that dynamic effects can also contribute to the integrated diffraction intensities.

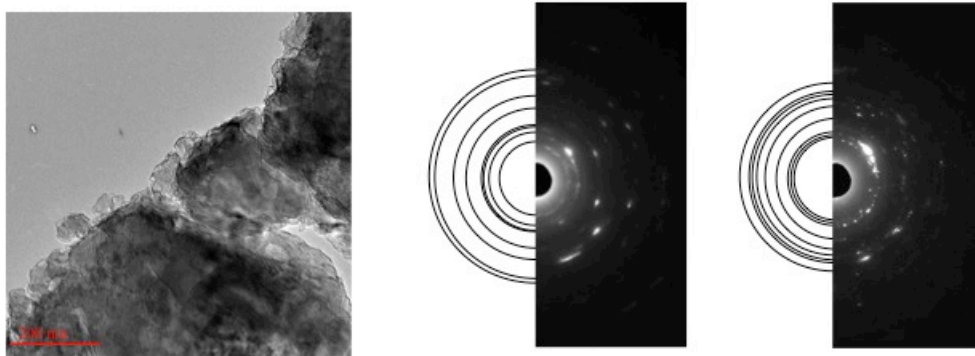


Figure A-2- Milled MgH_2 powder (a) and corresponding diffraction patterns for (b) newly exposed – simulation for MgH_2 - and (c) after 2.6 C/cm^2 –simulation for Mg.

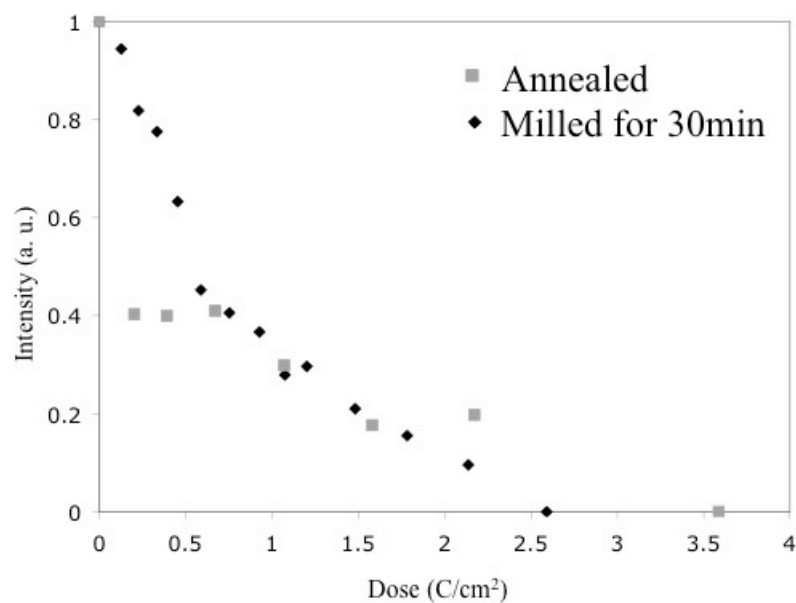


Figure A-3- Change in intensity of 110- MgH_2 reflections with increasing electron dose for annealed and milled samples.

This observation can be explained in the light of thermodynamic stability of the hydride phase inside a TEM. For the reaction $\text{Mg} + \text{H}_2 (\text{g}) \rightarrow \alpha\text{-MgH}_2$ at standard conditions we have the following values for enthalpy and entropy [1]:

$$\Delta H^0 = -74.5 \text{ kJ/mole}$$

$$\Delta S^0 = -135 \text{ J/mole.K}$$

Having the above values, using the Van't Hoff equation ($\ln P_{\text{eq}} = \Delta H^0 / (RT)$ -

$\Delta S^0/R$), the table below lists the equilibrium hydrogen pressure values, as function of temperature. This is assuming that hydrogen gas follows the ideal gas behavior within the mentioned range of temperature and pressure.

Table A-1- Equilibrium hydrogen pressures as function of temperature for α -MgH₂.

T (°C)	T (K)	P _{eq} (atm)
-196	77	3.25E-44
0	273	6.26E-8
25	298	9.83E-7
200	473	0.067
250	523	0.408
279	551	1

The vacuum in a TEM is usually in the range of 1E-8 Torr, i.e. 1.3E-11 atm. Hence if MgH₂ were to be studied at ambient temperature inside a TEM, it would be thermodynamically unstable ($P_{\text{TEM}} \ll P_{\text{eq}}$). Whereas if we use a cryogenic TEM sample holder (Liquid N₂ temperature, 77K) the situation is reversed and the local pressure in TEM is 33 orders of magnitude higher than the equilibrium pressure for the hydride, so MgH₂ is thermodynamically stable. This is the main reason that utilizing cryogenically cooled TEM sample holder can extend the stability time of the hydride phase within the TEM (as demonstrated in Chapters 2 and 3).

Beside the thermodynamic consideration mentioned above, we also have a beam-induced decomposition of the magnesium hydride phase. So even using the cryo-holder for microscopy, the hydride phase would eventually transform to a combination of magnesium and magnesium oxide. The difference here is the time-scale of the decomposition. Beam-induced decomposition takes place much faster at room temperature, since in that temperature the hydride phase is thermodynamically unstable and a minute heating caused by the electron beam can derive the dehydrogenation reaction forward. The main mechanism for the beam-induced decomposition is radiolysis, i.e. atomic displacement caused by the high-energy electron through an inelastic scattering incident [2]. This can readily happen for a light element like hydrogen.

Importantly though, radiolysis is temperature dependent and can be reduced by cooling the sample in the TEM.

So in summary, by cooling the magnesium hydride sample to cryogenic temperatures inside the TEM we can extend the stability time of this phase due to two main reasons. Firstly, in a cryo-stage TEM sample holder the hydride is thermodynamically stable. Secondly, lowering the sample temperature damps the main mechanism through which beam-induced degradation of the sample can occur (radiolysis).

References

1 Stampfer JF, Holley CE, Suttle JF. The Magnesium Hydrogen System. *Journal of the American Chemical Society* 1960; 82(14): 3504-3508.

2 Egerton RF, Li P, Malac M. Radiation Damage in the TEM and SEM. *Micron* 2004; 35: 399-409.

